

**Investigations on Magnetic, Optical and Transport  
Properties of Magnetic Nanofluids for Engineering and  
Biomedical Applications**

*Thesis submitted to  
Cochin University of Science and Technology  
in partial fulfillment of the requirements  
for the award of the degree of  
**Doctor of Philosophy***

*by*

**Reena Mary A P**



*Department of Physics  
Cochin University of Science & Technology  
Cochin- 682 022, India.*

*August 2011*

**Investigations on Magnetic, Optical and  
Transport Properties of Magnetic Nanofluids  
for Engineering and Biomedical Applications**

Author

**Reena Mary A P,**  
Pathiyam House,  
Palakkad (Dist)  
Kerala, India  
Pin: 683514

Supervising Guide

**Prof. M. R. Anantharaman**  
Head of the Department  
Department of Physics  
Cochin University of Science & Technology  
Cochin- 682 022, India.

**August 2011**

Cover page illustration

Front Cover: Rosensweig instability in water based ferrite fluid

Back Cover: FC-ZFC showing superparamagnetic blocking in MnZn ferrite  
nanoparticles –both synthesized in magnetic lab

## *Certificate*

Certified that the thesis entitled “**Investigations on Magnetic, Optical and Transport Properties of Magnetic Nanofluids for Engineering and Biomedical Applications**” submitted by Ms. Reena Mary A.P is an authentic record of research work carried out by her under my supervision at the Department of Physics in partial fulfillment of the requirements for the award of degree of Doctor of Philosophy under the faculty of science, Cochin University of Science and Technology and the work embodied in the thesis has not been included in any other thesis submitted previously for the award of any other degree.

Kochi-682022

25-08-2011

Prof. M R Anantharaman  
Department of Physics,  
Cochin University of Science and  
Technology, Kochi-682022,  
Kerala, India.

## **Declaration**

I hereby declare that the work presented in this thesis entitled “**Investigations on Magnetic, Optical and Transport Properties of Magnetic Nanofluids for Engineering and Biomedical Applications**” is based on the original research work carried out by me under the guidance and supervision of Prof. M R Anantharaman, Department of Physics , Cochin University of Science and Technology, Cochin-682 022 and no part of the work reported in this thesis has been presented for the award of any other degree from any other institution.

**Reena Mary A P**

**Cochin-22  
25-08-2011**

## *Acknowledgements*

Let me express my deep sense of gratitude I have towards my supervising Guide and Head of the Department of Physics, Prof. M. R. Anantharaman for taking me into confidence and for all the support and persistent encouragement extended to me. I am always grateful to him for his competent advices and sustained guidance throughout my Ph. D days.

I acknowledge CSIR, India for the financial support in the form of fellowship.

I wish to acknowledge all former Heads of the Department, Prof. V. C. Kuriakose, Prof. Ramesh Babu. T and Prof. Godfrey Louis, for providing the laboratory and library facilities during my course.

My sincere thanks to all the faculty members and members of office staff of the Department of Physics, Cochin University of Science and Technology for the help and support they have provided for the completion of this research work. Let me thank Prof. S Jayalakshmi for her support and encouragement. I do remember all my teachers during different stages of my life.

I am grateful to the faculty and scientists in various institutions around the world. Let me thank Prof. Guenter Schatz of University of Konstanz, Germany, who made me to view life from a different aspect, and his group members for magnetic measurements. I acknowledge with thanks Prof. Manfred Albrecht of Technical University Chemnitz, for stimulating discussions and magnetic measurements. I thank Prof. P M Ajayan of Rice University , Dr. Imad-al-Omari of Sultan Qaboos University Muscat, Dr. P A Joy of National Chemical Laboratory Pune, Dr. John Philip of IGCAR Kalpakkam, Prof. Philip Kurian of CUSAT and Prof. D Sakthi Kumar of Toyo University, Japan for helping me at various stages of my work. I thank the scientists at STIC, CUSAT for their technical help. I am thankful to Dr. Reji Philip of Raman Research Institute, Bangalore for helping in non linear measurements.

I recollect those days I had with my friends at Konstanz Dr. Ildico Guhr, Dr. Till Ulbrich, Dr. Denis Makarov, Dr. Felix Springer, Dr. Stefan and Dr. Sebastian for their

valuable help during the DST-DAAD project. I thank Dr. Suchand Sandeep for fruitful discussions and Mr. Smijesh from RRI Bangalore for their help.

Magnetics Laboratory has been a nice place to work in. I am deeply thankful to its alumini and present members for creating a warm environment and for their support and help, without which it would have been difficult for me to complete my degree. I remember Dr. K A Malini and Dr. Asha Mary John for their timely advice and affection showered on me. I remember Dr. S. Saravanan, Dr. Sajeev U S, Dr. Swapna S Nair, Dr. Mathew George and Dr. Prema K H with deep gratitude and love. I would always cherish the memories with Tom Thomas, Rajeev R Asokan, Syam Kishore, Anjali C. P, Binumon P K, Ram Kumar V R, Neeraj K, Navaneet P and Anand.P B.

The care and support of Dr. E. M. A. Jamal, Dr. Sagar S and Sanoj M. A. is remembered with thanks. Words cannot express my love and thanks to Veena, Vijutha, Senoy and Narayanan for the support they rendered me throughout my research days. I cherish the good times we had together in discussions and debates and for the support in my personal life. Let me express my thanks to Sudeep and Geetha for their whole hearted support and love. I am grateful to Dr. Smitha, Hysen Thomas, Mr. Vasudevan Nampoothiri, Vinayasree, Sethulakshmi, Lija, and Lisha for the warmth I felt in lab.

I thank with love and gratitude all my fellow research scholars of Department of Physics for the cordial atmosphere during my research days. I remember with love Gleeja, Sini, Mangala, Rose, Bhavya and dear friends of '*Athulya*'. I express my feeling of gratitude towards childhood friends of palakkad Navodaya.

I acknowledge the support from the staff and students of GPTC Palakkad and Dept. of Physics, GVC Palakkad.

Words are insufficient to express my feeling towards my parents, who inspire me and love unconditionally. I thank my brother Roy & his family, sister Rose mol, her family and in-laws, my cousins and relatives for their support and encouragement showered upon me.

I thank almighty for all those who come across my life...

**Reena Mary A P**

## *Preface*

The emerging area of Nanoscience and Nanotechnology has provided the right impetus for the socio-economic advancements witnessed during the past few decades. Nanotechnology deals with the manipulation of material properties by leveraging the size and shape effects on their properties at atomic/molecular scales. The advancement in this field demands a multidisciplinary approach that requires the expertise from physical, chemical and biological sciences, and also from different branches of engineering. Nanotechnology without physics is physics without quantum mechanics and nanotechnology without chemistry is chemistry without periodic table. Nanotechnology and biology is closer than ever before and more often the fruits of nanotechnology are often translated very quickly into products whether they are lab on a chip or drug delivery and drug targeting.

Nanotechnology has been known to men from ancient times when people applied nano gold in medicines for arthritis and gold colloids were applied as dyes in medieval period. Nanoscience, engineering and technology holds great potential to provide substantial improvements from medicine to data storage, from automobile engineering to energy harvesting and the areas not yet imagined. Exploring materials at the nanolevel is known from the 19<sup>th</sup> century when Faraday has experimented on the optical properties of orange coloured gold colloids. The well known lecture “there is plenty of room at the bottom” by Feynman has intellectually challenged and urged the material research to look at the synthetic techniques in the ‘bottom up’ approach and rendered a drastic turn in understanding the material properties. The spatial confinement in the atomic clusters or molecular assemblies have made the researchers in material science and engineering to fabricate nanodevices and the concomitant advancements in analysis and imaging techniques have demonstrated various

phenomena predicted by Quantum Mechanics. The understanding of the mechanism at the nanolevel demand the mother tongue of quantum mechanics and this makes physicists to be all the more engaged in this area of knowledge. Quantum mechanics speaks through the mouth piece of nanoscience. The prediction of single electron transistor is now a reality and so is the quantum hall effect. With the dawn of this brand new technology in the horizon of science, the brightest sun is the area of photonics. Photonic band gap materials, photonic crystals are some examples. Gone are the days when scientists used to modify various properties of materials by incorporating impurities, now they would modify the properties by manipulating the dimensionality, shape and size.

Magnetic materials and magnetism are known to man from time immemorial. Ancient mariners used them as lodestone, while in modern days magnetic materials are applied in computers, motors and engines, in magneto optical displays and in medical imaging and therapeutic techniques. Magnetism in nanotechnology has resulted in high density data storage, high speed sensors, and efficient actuators, in communication and for medical diagnosis and drug delivery. Atomic magnetism comes from the magnetic moment of electrons - the fundamental entity in magnetism. In ferromagnets, with positive interaction, all the spins are arranged parallel and result in spontaneous magnetization even in the absence of external field.

Ferromagnetic materials contain a number of small regions called domains in which the moments are aligned parallel figuring a net magnetization. The direction of net moments in each domain is different that it reaches a minimum at zero external fields. Domains are separated by domain walls. There are certain directions or crystallographic axes in crystals of magnetic materials which are favourable and known as easy directions along which magnetic moments are aligned. When in

external magnetic field the domain with direction favourable to the applied field direction grows at the expense of neighboring domains and at high applied fields, when the magnetic energy outweighs the anisotropy energy, a coherent rotation of all the moments takes place along the direction of applied field and the magnetization reaches a saturation value which is specific for each material. As the field is removed, the interactions keep a memory of the magnetization and a net magnetization results at zero field which is known as the remanent magnetization. This memory is made use in magnetic data storage. A reverse field applied to bring the magnetization to zero value is known as the coercive field.

Magnetic particles broadly exist in three categories. When the size is fairly large enough that contains more than a domain and the magnetization reversal occurs by domain wall motion. When the particle size is decreased, that it has the volume of a single domain, the domain magnetization needs to be rotated. This rotation results in large change in energy determined by the anisotropy of the material. So the single domain (SD) particles are bound to have large coercivity compared to the multi-domain (MD) particles. When the particle's size is further decreased, the thermal energy is sufficient to fluctuate the magnetization of the entire particle. The magnetisation reversal occurs in a time shorter than the measurement window. The particles behave paramagnetically but with large net magnetisation and distributed randomly. They exhibit superparamagnetism with zero remanence and zero coercivity. The decreased size is exploited for high density data storage. Data storage media need to operate at a temperature of 350 K and this sets a lower limit to the size of particles. Superparamagnetism is an unwanted phenomenon as far as storage applications are concerned. This is because of relaxation phenomenon. If superparamagnetism is not required in storage industry, SPIONs are much sought after in biology for various applications such as magnetic hyperthermia, imaging and

bio-labeling. Superparamagnetic particles of size less than 10 nm are the basic components for ferrofluids.

Ferrofluids are stable suspensions of fine magnetic particles in a suitable carrier liquid. They are stable in a gravitational field owing to the Brownian motion in the suspended medium. The inevitable Van der Waal interaction among the particles is stabilized by a surfactant which separates the particles from aggregating together. This surfactant is either a long chain polymer that provide steric hindrance or an electrostatic charge over the surface which repels the particles from coming closer. The stability criteria demand the suspended particles to be in the size regime of 10 nm and hence behave superparamagnetically except for systems with high magneto-crystalline anisotropy. Ferrofluids which combine magnetic property as well as flowability are technologically important as they are used in loud speaker coolants, in seals, micro actuators and sensors, and proposed for space applications and lab on chip applications.

Spinel ferrites are soft ferrimagnets which are technologically important materials. Owing to high permeability and low coercivity they are used in high frequency applications. The ferrite core in transformers and antenna are few to mention. The nanosized ferrite particles find greater application in data storage and biomedicine and in ferrofluids. They could be easily synthesized by simple co precipitation techniques.

Metals with particles size below Bohr radius are no more metals and they exhibit modified optical properties. The energy states get rearranged from bulk that they show blue shift in band gap and could exhibit good nonlinear optical properties. Metallic ferrofluids are good thermal and electrical conducting materials and are highly sought after in the thermal engineering as nanofluids. A small amount of

nanoparticles in the liquid modifies the electrical and thermal conductivity retaining the flow properties such as viscosity. Nickel nanoparticles are industrially pursued as catalysts and pigments. Being highly prone to oxidation the synthesis of metallic nanoparticles is challenging. Oxide layer at the surface of nanoparticles modifies the magnetic properties and surface passivation could prevent the oxidation.

Magnetic nanoparticles are ideal templates to study the magnetic, optical and magneto optical properties at the nanolevel. As the grain size reduces, the surface area become enormous and the properties are modified to a near molecular level. The properties depend on the quantum size effects as well as the kind of interactions among them. Ferrofluids are ideal systems to study these as the particle concentration and nature of the carrier determine the properties to some extent. Magneto optical dichroism measurements on ferrofluids can give considerable knowledge of the interacting nature of the particles.

Magnetic nanoparticles are highly desirable in several biomedical applications such as targeted drug delivery, cell separation, imaging and tagging and in magnetic hyperthermia. Ferrofluids with the magnetic nanoparticles properly functionalized could be easily guided to the desired site by an external magnetic field. This property is applied in targeted drug delivery and imaging. The biomedical application requires the nanoparticles to be cell compatible. Iron oxide nano suspensions in water could be a good bio friendly ferrofluid. Silica capping of nanoparticles provides better biocompatibility together with the ease of functionalisation with biomolecules.

Nanoparticles of magnetic materials and their composites are good systems where fundamental research and applications complement each other. The complex and modified phenomena exhibited by these particles are displayed by the

contributions from the intrinsic properties, inter-particle interactions, size distribution, finite size and concomitant surface effects. The synthesis techniques for each system are different and need to be optimized. The ferrofluids need to be synthesized with optimum conditions for getting a good dispersion and long shelf life. The magnetic optical and magneto optical properties of these fluids are studied for various possible applications and to understand the field induced aggregations. This thesis presents the synthesis techniques for ferrofluids based on some spinel ferrites and nickel. The structural, magnetic, magneto optical and nonlinear optical properties of these fluids are thoroughly analysed by various techniques. The biocompatibility and the possibility for bio medical applications in magnetic hyperthermia treatment are studied.

The title of the thesis is “**Investigations on Magnetic, Optical and Transport Properties of Magnetic Nanofluids for Engineering and Biomedical Applications**” and the whole thesis is divided into eight chapters as follows:

*Chapter 1* is an introductory chapter, an introduction to Nanoscience in general, and on the magnetic properties of nanoparticles and ferrofluids in particular. It outlines various properties and applications of nano sized particles especially magnetic nanoparticles and suspensions. General synthesis routes adopted for nanotechnology is also mentioned.

In *chapter 2* the different measurement and analysis techniques applied to characterize the nanoparticles are briefly explained. Schematics of the experimental set up and the underlined theory in each is briefed. Necessary equations are cited.

*Chapter 3* deals with the synthesis of nickel nanoparticles by auto combustion method and the nanofluid preparation by high energy ball milling with

the surfactant. The structural and magnetic properties of the prepared nanoparticles and nanofluid are analysed in detail. The synthesis technique for nanoparticles is found to be superior for oxide free Ni synthesis.

Synthesis and characterization of some spinel ferrite based ferrofluids are described in *chapter 4*. Iron oxide and cobalt substituted iron oxide ferrofluids are synthesized in kerosene. The effect of anisotropic cobalt substitution is explained. In the second part, water based and kerosene based fluid of manganese zinc ferrite is compared. A discussion on the magnetic interaction among the nanoparticles is also presented.

*Chapter 5* deals with the bio-compatible ferrofluids and their applications in medical fields. This chapter explains the synthesis of iron oxide nanoparticles suspended in water and silica modified iron oxide suspended in polyethylene glycol. The structural and magnetic properties are studied, and a possibility for magnetic hyperthermia is theoretically verified. The cell compatibility studies are also described in this chapter.

The magneto optical, nonlinear optical studies on the ferrofluids and microwave absorption studies on PVA iron oxide composites are presented in *chapter 6*. The interaction effects with respect to different magnetic systems and carrier liquid and surfactants are correlated. The nonlinear optical characterization by z scan set up shows good optical limiting behaviour in oxide fluids whereas a fluence dependant saturable absorption and excited state absorption is observed in nickel nanofluid.

The minimization of energy wastage demand good cooling systems with fast response and efficiency. *Chapter 7* describes the initial results on the transport

properties of the ferrofluids. Ferrofluids could be good candidates for heat transfer applications.

*Chapter 8* is conclusion which discusses the salient outcome of the present study and the different applications thereof. The need for further advanced analysis and the scope for futuristic applications are also discussed.

## Contents

### Chapter 1

<b>1. Introduction</b>	1
1.1 Fundamental properties at nano level	3
1.2 Magnetism and magnetic materials	4
1.3 Magnetic Interactions	8
1.3.1 Magnetic dipolar interactions	8
1.3.2 Exchange interactions	8
1.4 Magnetic Anisotropy	10
1.4.1 Magneto crystalline anisotropy	10
1.4.2 Shape anisotropy	11
1.4.3 Surface anisotropy	11
1.4.4 Exchange anisotropy	11
1.4.5 Induced anisotropy	11
1.5 Ferromagnetic Domains	12
1.6 Magnetism of nanoparticles	13
1.6.1 Single domain particles	13
1.6.2 Superparamagnetism	14
1.6.3 Variation of Coercivity	15
1.6.4 Surface effects and finite size effects	17
1.6.5 Transport properties	19
1.7 Ferrites	19
1.7.1 Structure of ferrites	20
1.7.2 Magnetic properties of ferrites	21
1.8 Ferrofluids	22
1.8.1 Stability criteria	23

1.8.2	Stabilization techniques	24
1.8.3	Modified Bernoulli's equation	26
1.9	Nanofluids	26
1.10	Nanoparticles and fluid synthesis	27
1.11	Motivation of present work	30
1.11.1	Objectives	34
	References	36

## **Chapter 2**

### **2. Experimental Techniques**

2.1	Synthesis of metal and metal oxide nanoparticles and fluids	40
2.1.1	Sol-gel method	40
2.1.2	Chemical co-precipitation technique	41
2.2	High energy ball-milling	41
2.2.1	Planetary ball-mill	42
2.3	X-Ray Diffraction Analysis	45
2.4	Transmission Electron Microscopy (TEM)	46
2.4.1	Selected Area Electron Diffraction Pattern (SAED)	48
2.4.2	Energy Dispersive X-ray Spectroscopy (EDS)	49
2.5	Scanning Electron Microscopy (SEM)	49
2.6	Fourier Transform Infrared Spectroscopy (FTIR)	50
2.7	Raman Spectroscopy	50
2.8	UV-Visible Spectroscopy	51
2.9	Magnetic Characterisation	53
2.9.1	Vibrating Sample Magnetometer (VSM)	53
2.9.2	Field Cooled and Zero Field Cooled Measurements	56

2.9.3 SQUID Magnetometer	57
2.10 Transient hot-wire method for thermal conductivity measurement	58
References	60

### Chapter 3

#### **3. On the synthesis and characterization of Nickel ferrofluid: Evidence for low temperature magnetic ordering in Nickel nanoparticles**

3.1 Introduction	64
3.2 Synthesis of Nickel nanoparticles and Nickel nanofluids	68
3.3 Structural and morphological analysis	68
3.4 Magnetic measurements	75
3.4.1 Magnetisation measurements on Ni P	76
3.4.2 Magnetisation measurements on Ni M	79
3.4.3 Magnetic studies on Ni F	82
3.5 Conclusion	86
References	88

### Chapter 4

#### **4. Ferrite based aqueous and hydrocarbon Ferrofluids: A case study on Surfactant mediated inter-particle interactions and substitution effect on the magnetic properties**

4.1 Introduction	92
4.2 Synthesis of Nanofluids	94
4.3 Structural characterization	95

4.4 Magnetic hysteresis measurements	98
4.5 FC/ZFC measurements	101
4.6 Cobalt substituted iron oxide ferrofluids ( $\text{Co}_x \text{Fe}_{(1-x)} \text{Fe}_2\text{O}_4$ )	106
4.7 Synthesis of cobalt substituted iron oxide nanofluids	107
4.8 Structural characterization	107
4.9 Magnetic measurements	110
4.10 Conclusion	114
References	116

## Chapter 5

### **5. Superparamagnetic iron oxide nanoparticles based aqueous ferrofluids for biomedical applications**

5.1. Introduction	120
5.2 Synthesis of iron oxide based and silica modified ferrofluids	124
5.2.1 Synthesis of aqueous ferrofluids	124
5.2.2 Synthesis of silica-coated PEG-based ferrofluid	125
5.2.3 Cytotoxicity Assay	127
5.3 Results and Discussion	128
5.3.1 Structural and morphological analysis	128
5.3.2 Magnetic characterization	133
5.3.3 Theoretical analysis for magnetic heating	138
5.3.4 Cytotoxicity of Ferrofluid Nanoparticles	141
5.3.5 Optical measurements	142
5.4 Conclusion	143
References	145

## Chapter 6

### 6. On the magneto-optical, non-linear optical and microwave absorbing properties of ferrofluids based on Nickel and ferrites

6.1 Magneto optics	150
6.1.1 Magneto optical effects in ferrofluids	152
6.2 Experiment	155
6.2.1 Linear dichroism on Nickel nanofluid(Ni F)	156
6.2.2 Dichroism studies in oxide fluids	158
6.3 Nonlinear optics	162
6.4 Third order nonlinearity	163
6.5. Nonlinear Mechanisms	164
6.5.1. Nonlinear scattering	165
6.5.2. Reverse saturable absorption	166
6.5.3. Multi-photon absorption	166
6.5.4. Free-carrier absorption/ Excited state absorption	167
6.6. Measuring nonlinear properties	167
6.7 Ferrofluids as nonlinear optical materials	168
6.8 Experimental	170
6.8.1. Z scan measurements on Nickel nanofluid (Ni F)	171
6.8.2 Z scan measurements on oxide fluids	174
6.9 Microwave absorption properties on Iron Oxide-PVA composite films	179
6.9.1 Synthesis of composite films	179
6.9.2 Experiment	180
6.9.3 Result and discussion	182
6.10 Conclusion	184

References	186
<b>Chapter 7</b>	
<b>A preliminary investigation on the transport properties of nanofluids based on iron oxide</b>	
7.1 Introduction	190
7.2 Theoretical concepts	192
7.3 Thermal conductivity on Iron oxide suspended in kerosene	194
References	196
<b>Chapter 8</b>	
<b>Conclusion</b>	199
<b>List of Publications</b>	207

## *Chapter 1*

### **Introduction**

The advancement in materials science has improved the living conditions of mankind to a great extent. The interdisciplinary nanoscience and nanotechnology has been identified as the technology for 21<sup>st</sup> century and is rapidly growing with high impact on society. Magnetic materials have a significant role in technology for mankind. Nanomagnetic materials with superior properties are progressively replacing the obsolete. The ferrofluid technology finds increasingly great applications in industrial, space and medical fields. The proper engineering requires understanding the properties at the fundamental level. This Chapter discusses an introduction to magnetism at the Nanoscale and the physics of ferrofluids with a brief description of applications. Towards the end, the motivation of the present study is spelt out and the objectives are highlighted.

## *Chapter 1*

---

Material science research and technology, for the past few decades experienced an overwhelmingly radical drift towards understanding the materials by engineering them near the molecular level. The physical properties of materials were engineered previously by altering the chemical composition where as recently this has been changed to engineering the particle sizes for tuning the desired properties [1-3]. This tuning of properties is applicable only at near molecular sizes where addition of few molecules does really matter i.e. when the particles sizes are in the nanometer scales, wherein the material properties make a transition to quantum mechanical nature. Nano, meaning dwarf, refers to  $10^{-9}$ m in science. Nanomaterials form applied materials as once micro technology used, but with near molecular properties besides providing miniaturization of devices. These materials exhibit extensively modified mechanical, electric, optical and magnetic properties from their micron sized counter parts [3]. Exploring the properties at the nano regime made a new branch of science, Nanoscience and engineering the properties at the nanolevel resulted in a new branch of technology Nanotechnology. Identified as the technology of 21<sup>st</sup> century, nanotechnology presents a multitude of applications in daily life as well as opportunities for growing fundamental scientific interest. This interdisciplinary science and technology has made its impact on society; the rapidly expanding branch of knowledge has crossed and combined the borders among different branches of science and engineering, offered the mankind with excitement and scientific challenges. This revolutionary field of science has been promoted by the advances in analysis techniques with atomic scale resolutions and refined synthesis techniques. The pioneering research in this area has made many spin offs and proven capability of making breakthroughs in recent future.

### **1.1 Fundamental properties at nano level**

Engineering nanoparticles and the underlying technology are known to man from medieval period. The church paintings of medieval ages are dyed with long lasting metal colloids, and now we know that they are particle size varied noble metal nanoparticles which retain their colour unusually over a large period. The dairy of faraday reports his optical studies on gold colloids which exhibited a red colour than the bulk glittering yellow. The physical and mechanical properties of nanostructures are found to be superior over the bulk materials due to the spatial confinement (finite size), increased surface area and surface energy of these nanoparticles. The increased surface area is advantageous for catalysts and high sensitive chemical sensors, and the functionalization of these nanoparticles presents many applications in colloidal chemistry and biomedical fields. The electronic band structure of the surface and inner atoms differ considerably and this gives rise to novel properties.

The mechanical properties such as elasticity, hardness, fatigue, toughness etc are found to be modified due to high ordered nature of crystallization. The imperfections can diffuse to surface on annealing in turn resulting in improved mechanical properties. Carbon fibers are reported to have high tensile strength and young's modulus. Composites of nanoparticles and polymers combine the dual properties of both ensuing improved mechanical, thermal and functional properties due to better mixing of the two.

When the size of nanoparticles approach molecular dimensions, the quantum mechanical effects come into play and the band gap modification modifies the electrical and optical properties to a great extent. The metallic particles owing to band gap variation start behaving semiconducting [4], due to the modification of density of states. Surface plasmon resonances (collective excitations of conduction electrons induced by the electric field of the incident radiation) are observed in metals [5-6],

causing a blue shift and offer many nonlinear optical and luminescent properties due to the reduction in particle size below certain limiting value. The confinement of electronic wave function in the particles presents a multitude of properties as seen in quantum dots [7]. These properties can be exploited for light emitting devices and solar cells.

Nanoparticles improve the wetting properties of surfaces as seen in nature. A fine coating with selected nanoparticles can act as hydrophobic or hydrophilic depending on the particles and the surface functionalization. Nanomaterials are promising candidates for hydrogen storage due to large adsorption area at the surface and improved chemical kinetics [8]. Recently nanoparticles are established for pollution control and for water purification process.

In magnetic materials, the size reduction and corresponding surface effects results in a rich variety of modified properties such as superparamagnetism, spin polarized tunneling, giant magneto resistance, tunneling magneto resistance, temperature dependant magnetic moment variation, shape anisotropy and these could find many overwhelming applications.

## **1.2 Magnetism and magnetic materials**

Magnetic materials are known to man and were a part of daily life from ancient times. The mariners used (iron oxide) lodestones in navigation. In modern days magnetic materials are technologically important in automobile, electrical, electronic and communication industries and in medical fields. The response of a material to an external magnetic field varies according to the ordering of atomic moments, the electrons and their spins and based on their interaction and ordering they are classified.

The fundamental entity in magnetism is the magnetic dipole moment. The atomic magnetism comes from the electron revolution and spin. Depending on the

electrons and their orbital overlap the atoms exhibit varied magnetic moments. In a solid with large number of atoms, the magnetic phenomena depend on the interactions among the atomic moments.

Magnetic moment  $\mu$  is related to the angular momentum,  $L$  by

$$\mu = \gamma L \quad (1.1)$$

where  $\gamma$  is the gyro magnetic ratio.

1. *Diamagnetism*

Diamagnetism is universally exhibited by all materials with weak negative susceptibility. When an external magnetic field is applied, the material induces a moment equal and in opposite direction according to Lenz's law. The diamagnetic substances are composed of atoms/ molecules with closed electronic shells and hence no net magnetic moment.

2. *Paramagnetism*

Paramagnetism refers to a positive susceptibility such that external magnetic field induces the moments to align along the direction. The atoms of these materials have unpaired electrons and hence a net magnetic moment. The moments on neighbouring atoms of paramagnetic substances are very weakly interacting and hence behave independently. In zero applied fields these moments are randomly distributed and hence have no net moment. The temperature applied will randomize, so the degree of alignment of the moments in the field direction depends on both the temperature and the strength of the applied magnetic field.

3. *Ferromagnetism*

Materials which have spontaneous magnetization in the absence of external field exhibit ferromagnetism. The magnetic moments of nearby atoms interact with one another strongly and align parallel. They have large positive susceptibility. As the temperature increases, the thermal energy tries to randomize the moments; and at a

## *Chapter 1*

---

particular transition temperature, the thermal fluctuation overcomes exchange energy and they behave paramagnetic. This transition temperature is known as Curie temperature. Below the transition temperature the interaction energy is larger and hence makes the individual moments to order parallel and this parallelism increases with lowering of temperature causing the magnetisation to increase. At absolute zero thermal fluctuation is zero and the perfect parallel alignment cause the saturation to be maximum value. The transition from ordered ferromagnetic phase to randomly oriented paramagnetic phase happens with a symmetry breaking second order phase transition.

Ferromagnetism and the large spontaneous magnetisation in ferromagnetic material are elucidated by a quantum mechanical approach of Heisenberg's exchange interactions based on the Heitler London theory of molecular structure. The exchange interaction in a two electron system leads to an exchange between two neighbouring spins  $S_i$  and  $S_j$  with an energy of

$$E_{\text{ex}} = - 2 J_{\text{ex}} S_i \cdot S_j \quad (1.2)$$

Where  $J$  is the exchange integral, when positive/ negative leads to parallel/antiparallel alignment of the magnetic moments.

Ferromagnetism of metals is explained by localized mean field theory and band theory. The former explains the contribution from the valence electrons localized at the atoms and not free to move in the crystal and this explains the variation of saturation moments with temperature, transition between ferromagnetic to paramagnetic state and the curie Weiss law. The room temperature ferromagnetism exhibited by the 3d transition elements such as iron, cobalt and nickel are best explained by band theory [9-11], where in the electrons are not localized on atoms but are collectively shared by the crystal and free to move . This theory best explains why

certain elements are ferromagnetic while others are not based on the energy bands of magnetic moments. This also details the non integer values of magnetic moment per atom due to the orbital overlap and spin coupling. The spin density functional theory can explain the magnetism of solid state considering the localized electrons and polarized electrons in the conduction band and their mutual interactions. The analysis is tedious but to some approximations because of the complexity arising from many electron calculation.

#### 4. *Antiferromagnetism*

When the exchange interaction is negative, the adjacent atomic moments are aligned antiparallel to each other by the molecular field. This leads to antiferromagnetism. This is easy to understand in systems with crystals containing two interpenetrating sublattices and the moments in one sublattice are aligned in opposite direction to that in the other. The nearest neighbours of one atom will be entirely on the other sublattice. The magnetization of each sublattice will be similar to ferromagnetism, but they will be in opposite directions and hence the net magnetization will be the difference of the two. This is nonzero below a transition temperature, known as Neel temperature, above which the moments turn paramagnetic behavior. The magnetic susceptibility is given by the Curie Weiss law (with  $\Theta$  negative)

$$\chi = 1/(T - \Theta) \quad (1.3)$$

where  $\Theta$  is negative. Antiferromagnets have weak but positive susceptibility. When an external field is applied, the direction of the applied field becomes important. The energy favorable condition to align in the field direction is no more valid. Energy decrease by moments that aligns in the field direction in one sub lattice is counter balanced by the energy increase in the other.

5. *Ferrimagnetism*

Ferrimagnetism refers to uncompensated antiferromagnetism, in which the magnetizations of the two sublattices are not equal and hence result in a net spontaneous magnetization. The crystal structure plays an important role in determining the overall behaviour. Ferrites are the best known ferrimagnets. Since the magnetization of each sublattice is different and has different temperature dependence, the Curie Weiss law is not obeyed as such.

**1.3 Magnetic Interactions**

The long range ordering of moments in magnetic materials is provided by different magnetic interactions [12].

*1.3.1 Magnetic dipolar interactions*

The magnetic dipolar interactions between two adjacent moments separated by a distance 'r' have energy

$$E_{d-d} = \frac{\mu}{4\pi r^3} \left[ \mathbf{m}_1 \cdot \mathbf{m}_2 - \frac{3}{r^2} (\mathbf{m}_1 \cdot \mathbf{r})(\mathbf{m}_2 \cdot \mathbf{r}) \right] \quad (1.4)$$

The dipolar interactions are weaker for atomic moments compared to the exchange mechanism and are dominant only at large distances and /or large moments.

*1.3.2 Exchange interactions*

Magnetic exchange interactions are the governing phenomena that explain the long range ordering in all kinds of ordered magnetism. This is of quantum mechanical origin with coulomb electrostatic nature. These exchange interactions are strong in nature and act only among nearest neighbours. The strength of interaction rapidly diminishes with distance. The exchange interaction is mathematically explained as equation 1.2.

*(a) Direct exchange interactions*

The exchange between electrons of the neighbouring magnetic moments (atoms) occurs directly. The low degree of overlapping of magnetic orbitals makes the direct exchange mechanism insufficient to explain the magnetic properties. The indirect exchange mechanism can explain the exhibited magnetic properties.

*(b) Super exchange interactions*

This is an indirect exchange interaction among magnetic moments mediated by a nonmagnetic ion. This kind of interaction is preferably exhibited in ionic solids. The interaction occurs via, the orbital overlap of the nonmagnetic ion (say oxygen in oxides) and the magnetic atom. The degree of overlap and hence the super exchange depends on the angle of the M-O-M bond. This super exchange usually results in antiferromagnetic ordering.

*(c) Double exchange interaction*

Double exchange dominates in oxides where the magnetic ions can exist with mixed valence states such as in spinel ferrites and manganites. The ferromagnetic alignment occurs via a double exchange between these multivalent ions through a neighbouring oxygen atom. The energy criteria favours the ferromagnetic alignment of the magnetic ions among which the hopping of electrons takes place with the spins parallel.

*(d) Indirect exchange in metals by RKKY interactions*

In metallic systems the interactions between the magnetic ions can be mediated via the conduction electron. A localized moment can polarize the conduction electrons which get coupled to another localized moment at a distance. This interaction results in long range ordering and has an oscillatory dependence on the inter moment distance.

*(e) Anisotropic exchange interaction*

The anisotropic exchange interaction results from the spin-orbit interaction, where the ground state of a moment interacts with excited state of the other ion formed by spin-orbit interaction. This forces the spins to be aligned to make the energy negative. This occurs in antiferromagnetic material with a component of ferromagnetism such as in  $\alpha$ -Fe<sub>2</sub>O<sub>3</sub>.

**1.4 Magnetic Anisotropy**

The magnetic properties depend on the direction in which they are measured. This makes the shape of the hysteresis curves measured. The anisotropy is practically important and is exploited for materials of commercial importance. The anisotropy can be of crystalline origin or from the size and shape of the particles and induced anisotropy and exchange anisotropy also assume importance [13].

**1.4.1 Magneto crystalline anisotropy**

There are certain crystallographic directions along which the moments prefer to align than other directions and are known as easy directions of magnetisation. Iron bcc has its easy directions along (100) and fcc Ni is easy along (111). The spontaneous magnetization remains the same along all directions but the field required to reach the saturation is different. This anisotropy originates from the spin orbit coupling and the spins align along a direction of minimum energy.

For a cubic crystal, the appropriate expression for anisotropy energy can be written as

$$E_k = K_1(\alpha_1^2\alpha_2^2 + \alpha_2^2\alpha_3^2 + \alpha_3^2\alpha_1^2) + K_2(\alpha_1^2\alpha_2^2\alpha_3^2) \quad (1.5)$$

$K_1$  and  $K_2$  are anisotropy constants and  $\alpha_1, \alpha_2, \alpha_3$  are direction cosines of the magnetisation vectors with respect to the crystallographic axes. The anisotropy

decreases with temperature and near Curie temperature the preferential orientation is no more expected.

#### **1.4.2** *Shape anisotropy*

A non spherical specimen of polycrystalline material with no preferential orientation can present anisotropy due to its shape. It is easier to magnetize along the longer dimension, since the demagnetizing fields are strong in the shorter direction. This shape anisotropy is exploited in one dimensional nanostructure for high density data storage.

#### **1.4.3** *Surface anisotropy*

The surface anisotropy is prominent in nanoparticles system where the relative amount of spins at the surface is large. This occurs due to the symmetry breaking at the surface and lesser coordination with the neighbour spins. The electronic environment of the surface such as core shell structures or ligands play important role in deciding the surface anisotropy. This depends on the shape of the nanoparticles as well.

#### **1.4.4** *Exchange anisotropy*

This is exhibited in core shell particles with ferromagnetic core and antiferromagnetic shell. The exchange coupling between the spins at the interface bias the ferromagnetic moment. This causes a unidirectional anisotropy which is exhibited as a shift in hysteresis loop. Exchange anisotropy has found great applications in magnetic data read heads.

#### **1.4.5** *Induced anisotropy*

Anisotropy can be induced in otherwise random anisotropic materials by annealing. The direction and magnitude of anisotropy can be altered. Casting or rolling can be applied to induce anisotropy.

### **1.5 Ferromagnetic Domains**

The spontaneous magnetisation exhibited by ferromagnetic materials and the way they get saturated in applied magnetic field are of great fundamental interest. The symmetry breaking of various order are of great interest in condensed matter. The ferromagnetic ordering results in symmetry breaking and the transition to symmetric paramagnetic state is a second order transition. A macroscopic system can break the symmetry by different ways in different regions of it.

The existence of ferromagnetic domains, small regions in which the spontaneous local magnetisation reaches the saturation value, was proposed by Weiss [14]. The direction of magnetisation need not be the same in all the domains and are aligned randomly that in zero external fields the net magnetisation of the specimen remains zero. The formation of domains minimizes the magneto static energy and the domains are separated by domain walls. The spins at the wall are differently oriented, which require energy expense since the exchange interaction tries to align the spins parallel. So the competition between the domain wall energy and the reduction in magneto static energy decides the splitting of ferromagnetic material into domains.

The external field aligns the domains in the direction of field and this explains the saturation of magnetisation of ferromagnetic specimens at low applied fields. The shape and size of the domains and the type of domain walls are determined by the different energy such as magneto static, magneto crystalline and exchange interaction energy. The magnetisation dynamics can be explained by domain theory. In the demagnetized state the moments of all the domains are oriented randomly and magnetisation averages to zero. In an external applied field, the domain aligned near to the field direction grows at the expense of neighbouring domains by domain wall motion aided by the external applied field. This wall motion occurs till the specimen exists as single domain with all moments parallel. Further increase in magnetisation

occurs by the rotation of the magnetisation from easy direction to the direction of applied field.

## **1.6 Magnetism of nanoparticles**

Magnetic nanoparticles exhibit a variety of modified properties from the bulk counter parts. The hysteresis loop parameters such as the coercivity and remanence get modified significantly. The particles exist as single domain and further decrease of size leads to superparamagnetism. The modification in magnetic properties at the nano dimensions arise from finite size effects and surface effects.

### **1.6.1 Single domain particles**

Magnetic particles broadly exist in three categories. When the size is fairly large enough that contains more than a domain and the magnetization reversal occurs by domain wall motion followed by coherent rotation. This in a crystalline material with high order and low magneto crystalline anisotropy leads to small coercivity. When the particle sizes are such that the energy minimized by splitting into domains are less than the energy expended in domain wall formation, they prefer to be exist as single domain. A SD (Single Domain) particle has large magneto static energy and in zero applied fields, the domain magnetisation prefers to be along the easy direction determined by the magneto crystalline and shape anisotropies. In an external field, the moments coherently rotate towards field. This rotation results in large change in energy determined by the anisotropy of the material. So the SD particles possess large coercivity compared to the multi domain particles. The magnetisation for the SD particles is given by the Stoner- Wohlfarth model [15]. For a magnetic field of strength  $H$ , applied at an angle  $\theta$  with easy axis of the domain, the energy density of the system whose magnetisation lies at an angle  $\phi$  to the magnetic field direction is given by

$$E = K \sin^2(\theta - \phi) - \mu H M_s \cos\phi \quad (1.6)$$

The minimum energy condition for the given applied field decides the magnetisation of the particles. This model predicts the anisotropy contributing to the coercivity and hysteresis.

### **1.6.2 Superparamagnetism**

When the particles sizes are further decreased, the thermal energy wins over the anisotropy energy which depends on the volume of the particles. Thermal energy become sufficient to fluctuate the magnetisation vector of the entire particle to reverse from one easy direction to the other without any external field in a time shorter than the measurement window. The particles behave like a paramagnetic gas, but with large moments of the order of thousand Bohr magnetons. They being randomly aligned in zero applied fields, an assembly of such particles has zero net moment. An applied field tries to align the moments parallel to it, whereas the thermal fluctuations keep them randomized. These particles exhibit *superparamagnetism* [16-17] with zero coercivity and zero remenance. Figure 1.1a illustrates the variation in coercivity with particle size. When the particles are in contact, there exists exchange interaction through the interfaces. Such cases are accomplished with random anisotropy when the anisotropy of individual particles is averaged over the aggregates.

The non-interacting superparamagnetic nanoparticles independently reverse and the magnetisation follow classical Langevin theory of paramagnets given by

$$\frac{M}{M_s} = L(x) = \text{Coth}(x) - \frac{1}{x} \quad (1.7)$$

where  $x = \mu H/k_B T$ ,  $\mu$  is the particle magnetisation equal to  $M_s V$ ,  $M_s$  the saturation magnetisation,  $V$  the volume of the particle, and  $k_B T$  the thermal energy. When magnetisation curves are measured at different temperatures, they superimpose when plotted as a function of  $H/T$ .

The anisotropy energy (KV) forms the energy barrier for magnetisation reversal in thermal fluctuation. The probability for this can be represented by Boltzmann factor  $\exp(-KV/k_B T)$ . The relaxation time  $\tau$  for a moment to undergo reversal is given by

$$\tau = \tau_0 \exp\left(\frac{KV}{k_B T}\right) \quad (1.8)$$

Where  $\tau_0$  varies from  $10^{-9}$  to  $10^{-12}$

At high temperatures the relaxation occurs rapidly; as the temperature is lowered the thermal fluctuation reduces and when the relaxation time become larger than the measurement window, the system appears away from superparamagnetic state. The temperature at which the thermal energy and anisotropy energy compromises can be found. For a typical measurement time of 100 s in static magnetic measurements, this amount to

$$T_B = \frac{KV}{25 k_B} \quad (1.9)$$

Where  $T_B$  is called the blocking temperature, below which the anisotropy block the thermal relaxation of the moments. A critical volume for a material with definite anisotropy, to remain superparamagnetic is given by  $V_p = 25 k_B T/K$  which gives the upper limit of superparamagnetism.

### ***1.6.3 Variation of Coercivity***

The decrease in particle size causes the existence of particles as SD, and the magnetisation requires coherent rotations through the hard direction. This presents a large anisotropy as seen by an external magnetic field and results in large coercivity. With decrease of particle size, the coercivity increases and the dependence of coercivity on particle size is given by

$$- \quad (1.10)$$

Where  $a, b$  are constants and  $D$  the particle diameter. Below a critical size decided by energy and anisotropy, particles remain SD and coercivity increases, and further decrease of size, the thermal effects decreases the coercivity as given by

$$- \quad (1.11)$$

At sufficiently small size, the particles exhibit superparamagnetism with zero coercivity. Figure 1.1a depicts the variation of coercivity with particle size. [a,b,12]

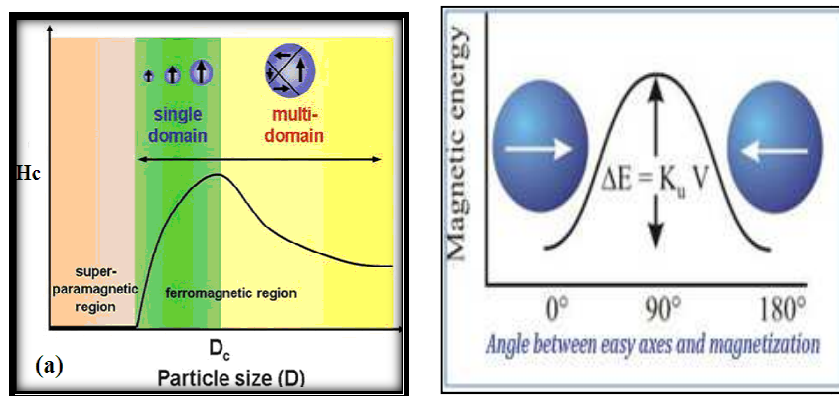


**Figure 1.1: (a) The variation of coercivity with particle size, (b) energy barrier showing superparamagnetism ()**

The dynamic behaviour (relaxation time) of a concentrated nanoparticle system gets modified due to the strong inter-particle interactions. The dipolar interactions which always exist and the interaction through the surface of particles mainly contribute. This increases the effective magnetic volume and hence the energy barrier for superparamagnetism. They act as collective system and possess a spin glass like behaviour owing to some ordering phenomena exhibited by fine particles. This can be controlled by tuning the inter-particle distance. The Neel-Brown model for relaxation

time could be modified with the introduction of the interaction effects.  $T_0$  denotes the effective temperature that account for interaction.

$$\tau = \tau_0 \exp\left(\frac{KV}{k_B(T_B - T_0)}\right) \quad (1.12)$$

#### ***1.6.4 Surface effects and finite size effects***

The magnetic properties of nanoparticles have contribution both from the finite size and the surface effects, and they are counteracting in certain cases. Finite size results from the characteristic dimensions resulting from the decrease of volume. The surface effects occur simultaneously since as the size decreases, the surface to volume ratio increases, and the surface plays an important role. These surface effects originate from the translational symmetry breaking at the surface of fine particles, where the coordination number is lowered. The broken magnetic exchange leads to surface spin disorder and frustration of spins. The misalignment of surface spins cause strong deviation from the expected behaviour. For a 1.6 nm sized fcc Co particles 60% of spins exists at the surface and hence the effect is dominated by the surface spins rather than the bulk or core spins. The magnetisation of fine particles is composed of contributions from both.

##### ***(i) Surface anisotropy***

Coercivity of fine particles is assumed to be zero. The anomalous anisotropy exhibited in fine magnetic particles is attributed to be arising from the surface. The existence of structural disorder or lattice vacancies and the contraction of surface layers results in crystal fields that are directed normal to the surface which may produce easy planes of magnetisation. The surface and core behave differently when the anisotropy becomes comparable to ferromagnetic exchange of the core moments. Surface become magnetically hard compared to core. The effective anisotropy is defined for fine particles of diameter  $D$

$$K_{eff} = K_b + \frac{6}{D} K_s \quad (1.13)$$

Where  $K_b$  and  $K_s$  are contribution from bulk and surface respectively.

*(ii) Surface spin disorder*

Magnetisation in nanoparticles is reduced from the bulk value in many systems. It was considered to be due to the formation of a dead magnetic layer from the demagnetizing effect of surface spins, which does not contribute to net magnetisation. Reduction of saturation in ferrimagnetic oxides were proposed by a random canting of antiferromagnetic spins at surface. The later studies show that the spin canting occurs throughout the volume of nanoparticles and is due to the finite size. The magnetic moment does not get saturated even at high fields, and this indicates the existence of spin canting in these materials. A model in which the nanoparticles undergo a spin glass like transition below a temperature has been proposed for a magnetically ordered core with a canted spins at the surface. The shell below the freezing temperature imposes an exchange field over the core and a shift of hysteresis loop is observed.

Enhancement in magnetisation is exhibited by fine metals particles or clusters of few to few hundred atoms of iron and cobalt [18-19]. Some 4f elements paramagnetic in bulk show ferromagnetic moment [20-21]. This enhancement is attributed to the surface atoms whose atomic neighbourhood is different. The modified symmetry at the surface changes the electronic structure and band narrowing due to reduced orbital overlap at the surface causing an enhancement in moment. Atomic clusters of few nanometer sizes possess spin wave excitations that present thermo dynamical properties such as the variation of moment with temperature at saturating fields.

**(iii) Curie temperature ( $T_c$ )**

The Curie temperature strongly depends on size and follow a scaling law [22-24] proposed as

$$\frac{T_c(\alpha) - T_c(D)}{T_c(\alpha)} = \left( \left( \frac{D}{D_0} \right)^{-1/\nu} \right) \quad (1.14)$$

Where  $T_c(\alpha)$  is the bulk curie temperature,  $T_c(D)$  curie temperature as a function of diameter and  $\nu$  is the initial exponent of the correlation length. This scaling is a consequence of finite size effects and surface effects. The decrease in  $T_c$  is mainly contributed from the predominant surface effects. Some oxide ferrimagnets increased the Curie temperature [25] and this is due to suppression of surface effects.

**1.6.5 Transport properties**

The electron scattering at the interface of granular magnetic/ nonmagnetic systems are influenced by the surface disorder and roughness. This is seen in multilayer of alloys and magnetostrictive compounds. Dispersion of ferromagnetic particles in an insulating matrix exhibits variety of transport properties due to the finite size effects and the matrix effects. Spin dependent scattering of conduction electrons is exploited in giant magneto-resistance (GMR) materials. Granular metals exhibit phenomena like spin polarized tunneling [26] conduction and coulomb blockade.

**1.7 Ferrites**

Ferrites are technologically important materials extensively applied in modern electronic and communication industry, and ferrofluids technology. Nanoparticles and suspensions of ferrites assume importance in high density data storage, electromagnetic systems, magnetic resonance imaging and drug delivery, and of fundamental interest since they are ideal templates to study various interactions occurring at the atomic and electronic level.

### 1.7.1 Structure of ferrites

Ferrites are mixed metal oxides that combine with iron (III) oxides and crystallize in three types mainly spinel type and garnet type with cubic structure, and Magnetoplumbite with hexagonal crystal structure. Spinel ferrites are the simplest of these with a structure of natural spinel and have a chemical composition of  $MFe_2O_4$  where M is a divalent metal ion such as Ni, Co, Fe, Mg, Zn and Mn. Figure 1.2 shows spinel structure.[a]

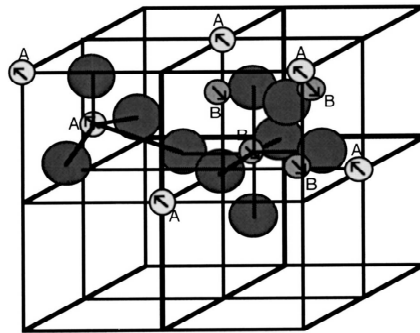


**Figure 1.2: Unit cell of a spinel structure (dark circles denote oxygen anions)**

The crystal structure is comprised of lattice of oxygen atoms which are in the face centered packing such that there are two kinds of voids or interstitial sites; A sites with tetrahedral coordination and B sites with octahedral coordination. A unit cell comprises 64 tetrahedral sites of which 8 and 32 octahedral sites out of which 16 are occupied. A unit cell possesses eight formula units.

The distribution of cations in the respective sites is collectively determined by the ionic radii, the crystal field and Madelung energy. The electrical and magnetic properties of spinel arise from the distribution of divalent ion and ferric ion in different lattice sites. The cobalt ions have strong octahedral preference while zinc prefers tetrahedral site. In general, the cation distribution can be represented by  $M_{1-\delta}^{2+} Fe_{\delta}^{3+} [M_{\delta}^{2+} Fe_{2-\delta}^{3+}] O_4$  where bracket indicate the octahedral sites.  $\delta$  is the

degrees of inversion;  $\delta= 0$ , represent normal spinel structure,  $\delta= 1$ , inverse spinel and fraction indicate the mixed spinel structure. Magnetite is an inverse spinel, a soft ferrimagnet which is semiconducting at room temperature, a thoroughly studied material for various engineering and biomedical applications.

### **1.7.2      *Magnetic properties of ferrites***

Ferrites exhibit ferrimagnetic ordering, which can be explained on the basis of Heisenberg's exchange interactions. Super exchange interactions exist between the magnetic ions occupying the different lattice sites mediated by the oxygen atoms. The three possible interactions are A-A, B-B and A-B interactions all of which favours antiferromagnetic ordering. The strength of interaction in various interactions depends on the inter-atomic distances and the angle between magnetic ions through the anion. Strongest interaction occurs when the angle is  $180^0$  and the distance is least. The A-A and B-B interactions (large distances and comparatively smaller angles) become much weaker compared to the A-B interactions and this makes the spins at A and B sites to order antiferromagnetic in nature. Neel proposed a two sub lattice theory in which the unit cell can be assumed to be comprising of two interpenetrating sublattices with the moments in one are anti parallel to the other. The net magnetisation can be written as the difference of the moment at two sub lattice.

Moving to nanolevel systems of ferrites, the redistribution of cations are observed in a number of ferrites [27-30]. Most interestingly this redistribution modifies the electrical and magnetic properties with regard to ac conductivity, saturation magnetisation, and Curie temperature. The deviations from the expected bulk magnetic properties are attributed to the finite size effects and surface effects and the redistribution of cations at different lattice sites.

## **1.8 Ferrofluids**

Ferrofluids combine specifically magnetic property as well as flow ability. Magnetic fluids constitute colloidal sized superparamagnetic particles suspended in a carrier liquid of desired properties. Ferrofluids find innumerable applications in the fields of sensors and actuators, as dynamic sealing-zero leakage rotary shaft seals, vacuum feed through, pressure seals, in heat exchangers, and in ferrofluidic micropumps in lab-on-a-chip applications [31-34]. Ferrofluids has been studied as magnetic fluid inks in high speed printing [35]. These fluids are applied to detect domains in alloys and crystals.

Ferrofluids, could be easily guided through circulatory system, with an external magnetic field present a wide span of applications in biomedical fields such as site specific drug targeting where optimum drug could be delivered to the infected tissues. They are applied in enzyme immobilization, imaging, cell separation, and labeling and in diagnostics. The magnetic hyperthermia is a proposed field in which the magnetic fluid guided and attached to malignant cells are heated and destroyed without affecting the healthy tissues. Hysteresis or relaxation loss of the attached magnetic particle in an applied AC magnetic field will cause the rupture of the cell.

Not found naturally, since every magnetic material has its curie temperature well below the melting point, a ferrofluid need to be synthesized. They are prepared by dispersing magnetic nanoparticles coated with a surfactant in a liquid. Brownian motion keeps the particles suspended and the surfactant prevents the particles from coalescing. Ferrofluids are expected to be free from settling under gravitational force and magnetic interaction of permanently magnetized particles. This is due to small size of the suspended nanoparticles. A typical ferrofluid has  $10^{23}$  particles per cubic meter. Stability of a fluid is an important requirement for application and scientific investigations.

### 1.8.1 Stability criteria

There are different mechanism involved in the existence and stability of ferrofluids. The different energies possessed by a fluid particle are

- a) Thermal energy  $k_B T$
- b) Magnetic energy  $\mu H V$
- c) Gravitational energy  $\rho V g L$

Where  $k_B$  is the Boltzmann constant,  $T$  the absolute temperature,  $V$  the particle volume, and  $L$  is the elevation in gravitational gradient. The ratio of one energy to another may affect the stability of the fluid.

When ferrofluid is subjected to an external magnetic field, particles are attracted to high intensity regions of the field, whereas the thermal energy keeps the particles in random motion. The stability against settling in force field is given by a high ratio of thermal to magnetic energy, i.e. Thermal energy/ magnetic energy,

$$\frac{kT}{mHV} \geq 1 \quad (1.15)$$

Considering the spherical shape of particle, the particle size for stability is given by,

$$D = \left( \frac{6kT}{\pi\mu H} \right)^{1/3} \quad (1.16)$$

For a magnetite particle at room temperature in a field of 1000 gauss requires the size to be around 8 nm.

Gravitational field is being constantly acting on the particles which are forced downwards, and the stability against sedimentation is provided by the thermal motion. When considering the influence of magnetic energy, gravitational energy is very less. Once stable in magnetic field the fluid is stable in gravitational pull as well.

A colloidal ferrofluid particle undergo collisions during the motion, and it is plausible for them to adhere together forming agglomerations. As the particles are permanently magnetized, there could be dipolar exchange resulting in dipole–dipole pair energy. When the particles' surfaces are in contact, this energy is given by

$$E_{dipole} = \mu M^2 V / 12 \quad (1.17)$$

Thermal agitation should be greater than this dipolar energy so as to keep the particles from agglomeration and this stability criterion demands the ratio, Thermal energy/dipole dipole pair energy;

$$\frac{24kT}{\mu M^2 V} > 1 \quad (1.18)$$

to be greater than unity. This gives the stable size of the particles in fluid as

$$d \leq (144kT / \pi \mu_0 M^2)^{1/3} \quad (1.19)$$

for magnetite particles this size at room temperature is 9.8 nm. Normally in a ferrofluid with good shelf life, the particle size is found to be around 10 nm.

There occur van der Waals forces which are attractive in nature between neutral particles. The fluctuating orbital electrons in one particle induce dipoles in the neighbouring particle and this quantum mechanical interaction is responsible for this electric dipole-dipole forces. From the dipolar interaction theory, the field varies as  $r^{-3}$  and field gradient as  $r^{-4}$ , the forces vary as  $r^{-7}$  and energy as  $r^{-6}$ . Hamaker extended the sixth power law for spheres

$$\text{Dipole energy} = A/6(2/(l^2+4l)+2/(l+2)^2 + \ln(l^2+4l)/(l+2)^2) \quad (1.20)$$

This shows that the surfaces should be prevented from being in contact.

### **1.8.2 Stabilization techniques**

The particles are stabilized in the suspensions by surface treating them so that the van der Waals forces are overcome. Broadly the stabilization techniques are classified as electrostatic stabilization and steric stabilization and the resulting fluids

are known as ionic fluids and surfacted fluids respectively. Figure 1.3 shows the surfactant effects on particles.[32]

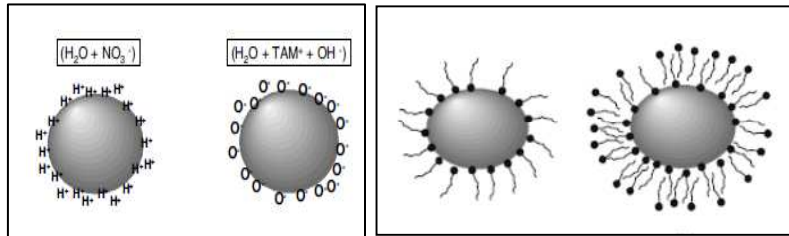


**Figure 1.3 : electrostatic and steric surfactants in action**

In electrostatic stabilization the particles are surface treated with acidic or basic radicals such that charges exist at the particle surfaces and get repelled from one another due to coulomb interaction. Tetra methyl ammonium hydroxide and citric acid are surfactants that provide ionic repulsion.

Steric stabilization is provided by adsorption of a long chain molecule that physically prevents the particles from coming closer. The polar tail well suspends the particle in base liquid as well. Oleic acid and its derivatives are best known steric surfactants. Figure 1.4 shows the net interaction curve for different energy.

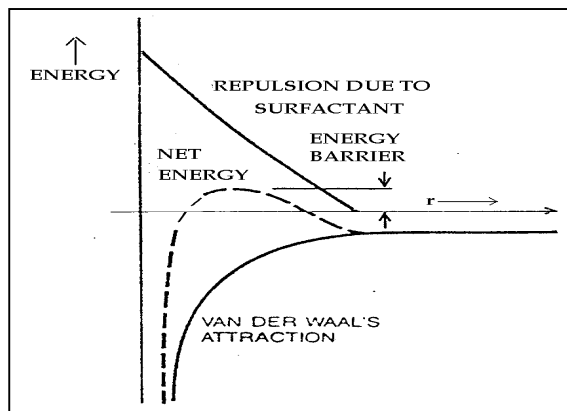


**Figure 1.4: The significant energies that affect the particle agglomeration**

### **1.8.3 Modified Bernoulli's equation**

The flow property of the ferrofluids is influenced by an external field. The energy conservation in flow modified the Bernoulli's equation as

$$p + \frac{1}{2}\rho v^2 + \rho g z - \int_0^H M dH = \text{constant} \quad (1.21)$$

This equation could be analyzed in important fields where hydrodynamics are to be studied in detail such as magneto controlled seals and nozzles, levitations in fluid and conical meniscus formed in fluid surfaces.

### **1.9 Nanofluids**

Nanofluids are fine suspensions of nanoparticles in base liquid, originally proposed to improve the heat transfer properties in heat engineering by increasing the thermal conductivity. The large surface area provides more heat transfer interface between the solid particles and liquid. High stability and dispersibility, reduced clogging in channels, adjustable wettability make these nanofluids superior over conventional solid liquid composites.

Extensive studies are carried out in alumina and copper oxide [36] suspensions in water and ethylene glycol and all exhibited an enhanced thermal conductivity with particle concentration in the low volume percentages. The enhancement is explained as the increase in surface area. Suspensions of 10 nm Cu particles exhibited a 40% enhancement at a 0.3% concentration [37]. Recently the most vigorously studied graphene and its composites [38-39] presented an enhanced thermal conductivity. The classical theories predict the effective thermal conductivity of the solids and matrix depending on the conductivities of solid and liquids. There are models that predict the dependence of size and shape of the constituent solid particles other than

the thermal conductivity itself. Mechanisms such as local clustering, concentration, and size and the interfacial characteristics between the nanoparticles and solvent and Brownian motion contribute to the total conductivity.

Ferrofluids or magnetic nanofluids could be easily controlled by an external magnetic field. The magneto optical studies show the field induced chain formation in these fluids and they could act as thermally conducting channels. The thermal conductivity enhancement in applied field [40] is explained as the effect of aggregates rather than the micro convection. The study of heat transfer of ferrofluids and the underlying mechanism of field dependent variation are quite interesting for heat transfer applications.

#### **1.10 Nanoparticles and fluid synthesis**

Present day material science requires the expertise to organize materials with controlled morphology low dimensionality and functionality. The synthesis of few atoms or molecules with the desired property and stability is rather challenging. The size, size distribution, morphology and dimensionality of the nanoparticles and their distribution greatly modify the physical, chemical and mechanical properties that their synthesis requires careful manipulation. There are basically two methods employed for nanoparticles synthesis. Top down approach where the nanoparticles are synthesized from the bulk cutting down into nanosized ones by machining or etching ,and bottom up approach where the buildup of nanoparticles occurs from the fundamental molecules or atoms which in turn self assemble to form nanoparticles of desired size and shape.

Top down approaches include conventional grinding and high energy ball milling process where micron sized particles are milled for hours to days with very high energy consumption and non-homogeneity in size distribution. These methods

also tolerate other functional shortcomings. Bottom up approach include vapour phase route and solution phase approach. The solution phase approach includes sol- gel and wet chemical routes involve chemical reactions of few reagents in liquid state. Vapour phase method involves production of a supersaturated reactive vapour in which nucleation and growth occur in vapour phase by condensation. Inert gas atmosphere is employed for metal nanoparticles and air for oxide particles. Synthesis techniques such as pyrolysis, laser ablation, plasma synthesis and chemical vapour deposition form vapor phase methods. The size and morphology of the condensed particles can be controlled and preserved by adding proper stabilizing agents. The metal nanoparticles, oxides and alloys are synthesized in large quantities by these methods. The vapour phase condensation is a preferred technique to synthesize nanofluids of metals and inter-metallics. The stabilizing agents act at the surface of nanoparticles and arrest the growth process at some stage of reaction. This controls the size of nanoparticles. The size and morphology can also be controlled by reaction parameters. Bottom up approach has the flexibility to expand the reaction conditions and choice of parameters for a wide variety of applications and is cheap and tunable for the desired size and morphology of nanoparticles.

Sol gel methods include hydrolysis, condensation and decomposition of alkoxides/precursors. Sol which is a stable solution of metal salts in organic solvent of desired properties at optimum pH undergoes hydrolysis and forms a network structure, gel. Water, alcohol or base or acid are used to control the chemical kinetics. The concentration of the precursors, the rate of heating the sol and the pH, collectively decide the size of the resultant particles. During aging the water or the solvent is removed. Finally the decomposition of the gel results in removal of precursors or reagents to obtain nanoparticles.

Poly-ol condensation requires a high boiling solvent alcohol and the condensation occurs at elevated temperatures. Normally a surfactant is applied and refluxing at high temperatures results in nanoparticles formation. FePt nanoparticles are reported to be synthesized by this method. The usual surfactants used are oleic acid, oleylamine and poly vinyl pyrole.

Micro emulsion method uses an emulsion of either water in oil, or oil in water mixture. A surfactant is employed for reducing the surface tension. The choice of surfactant and the desired ratio of surfactant to water decide the size and shape of the nanoparticles formed. They form micelles that act as nano reactors in which the nucleation occurs and the growth is controlled inside these nano reactors thus giving the desired size with narrow size distribution. This method is widely used to synthesize metal nanoparticles, inter-metallic and multi-metallic nanoparticles and oxide nanoparticles as well. The micelles formed can be spherical, cylindrical or of required shape which in turn decides morphology of the nanoparticles.

Chemical co precipitation from metal salts is an economic synthesis technique, widely accepted. Reaction in the solution results in freshly formed molecules or atoms which act as nucleation centers for precipitation. These grow to form nanoparticles. The nucleation and growth conditions can be altered to engineer the size and shape of the nanoparticles.

A supersaturated solution is thermodynamically unstable and can generate small sol particles. The free energy of the tiny particles at the surface is so large that they grow to form particles. Nucleation stops when the concentration decreases below a critical value. The particles continue to grow to equilibrium. Size can be controlled by the rate of reaction. When the reaction is rapid, more nucleation centers are formed and arresting the growth of particles can lead to formation of monodispersed particles at lower dimensions. The supersaturated state can be maintained to help nucleation

preventing the growth thus controlling the size. Growth stops when the reactants are depleted and this is followed by Oswald ripening. Particles below critical sizes coalesce to form larger ones, and a kind of secondary growth process takes place when the particles aggregate together. This aggregation can be controlled if at this stage the particles are provided with capping of organic ligands or polymers.

The stable suspension of nanoparticles of any material requires proper stabilization mechanism. The metal nanoparticles such as gold, silver, copper, nickel, cobalt and semiconducting compounds ZnO, alumina, titania, CdS, ZnS, iron oxide, and their colloids are commercially available in the desired nanosize for various optical, magnetic and medical applications. There are many multifunctional core-shell nanostructures that possess application potential, and self protection for metal nanoparticles by own oxides are studied recently. Nanoparticles with large surface energy and van der Waals interaction combine together to form aggregates under gravity or grow to form larger particles. They are also protected by electrostatic charges at the surfaces to remain stable in suspensions.

The stability of the nanoparticles suspension in the required base liquid for any desired application need the optimum particle size, the proper surface stabilization of the nanoparticles and the proper choice of the suspending medium.

### **1.11 Motivation of present work**

Ferrofluids are increasingly pursued for many technological applications in engineering and biomedical fields being the only class of fluid magnetic materials. These fluids with special mechanical and flow properties are applied in dynamic seals, dampers, thermal management, shock absorbers, sensors and actuators owing to their magneto controllability. They also present many modified optical properties under an applied magnetic field. The constituents being superparamagnetic in nature, offer complex relaxation behaviour in magnetic field and hence are interesting to

study the fundamental magnetism at nanolevel. The fluids functionalized with antibody or any other functional chemical species could be guided through the circulatory system of living beings by applied magnetic field to the desired site and hence find innumerable applications in medical diagnostics and therapy.

Synthesis of nanoparticles and ferrofluids are quite challenging since one needs control over the size as well as size distribution and shape of the particles. These particles need to be dispersed in liquid to form fine suspensions with good shelf life and stability. A number of synthesis techniques are available for the synthesis of nanoparticles and fluids, among which wet chemical routes with in situ surface modification is economic and simplified. The synthesis conditions for each system varies considerably and for best results one has to optimize the parameters involved in the chemical reaction. High energy ball milling is another technique which can be used to further cut down the size of nanoparticles.

Ferromagnetic metal nanoparticles assume importance from a fundamental perspective since they are ideal templates for studying magnetism at the nanolevel interfaces. Nickel with least anisotropy is an ideal template to study the finite size effects on magnetic properties. Nanoparticles of nickel with desired size and high purity find applications in pigment industry and catalytic conversion. These demand a large scale synthesis of nanoparticles. The metal nanoparticles are highly prone to oxidation and hence their synthesis needs extreme care with definite synthesis protocol. Dispersing the metal nanoparticles to form stable suspensions is still a challenge regarding the stability and uniformity in dispersion. The size when brought down to 5 nm range, the magnetic properties are often found to be resulting from the oxide phase evolved and from the frustrating spins at the surface. The study of solely finite size effects demand purity of the metal nanoparticles.

Ferrite nanoparticles and their ferrofluids are significant in electronic and communication industry due to their complex dynamics and applications thereof. Conventionally these ferrimagnetic oxides are studied with substitution of different divalent metal ions. The properties such as magnetisation, coercivity and remanence of ferrite nanoparticles get modified from the bulk ones with many superior applications. The cobalt substituted iron oxides are found to enhance the anisotropy and is superparamagnetic at lower sizes compared to iron oxide. The cobalt containing nano ferrites are studied for high density data storage applications, magneto-strictive and magneto caloric applications, since the size can be tuned to obtain blocking near room temperature. Manganese zinc ferrites and their fluids are particularly of importance in ferrofluid technology and Magnetocaloric applications since the Curie temperature can be manipulated by varying the zinc substitution. The nanoparticles of ferrites are interesting since they are often susceptible to cation redistribution that results in different degree of inversion which is different from the bulk configuration. This modifies the magnetic properties to a great extent. The fluids of ferrites with different surfactants offer varied inter particle interactions and a comparison of these could give the effect of inter-particle interaction on magnetic properties.

The nano ferrites are increasingly applied in biomedical fields such as cancer imaging, diagnosis cell separation, drug delivery and bio-labeling. Iron oxide nanoparticles coated with dextran are widely used in MRI to enhance the contrast in imaging. The nanoparticles functionalized with drug and made into a fluid can be easily guided through the blood stream to the infected tissue by external magnets. This allows optimum dosage of drugs or radiation without damaging nearby healthy tissues. With high specificity by proper functionalisation, the magnetic nanoparticles could absorb energy from external alternating magnetic field and heat the cells to

which they are attached. This is magneto hyperthermia which is superior to other hyperthermia techniques. The heating efficiency of magnetic particles is primarily due to the relaxation process and depends on the magnetic properties of the nanoparticles, the viscosity and heat capacity of the surrounding medium. The biomedical applications require the particles to be bio compatible. Iron oxide is bio-compatible and this could be improved by surface modification with more biocompatible coating. The analysis for energy dissipation in an AC field and cell compatibility studies could be interesting for hyperthermia applications.

The magneto optical properties of ferrofluids are governed by intrinsic properties and the field induced structural anisotropy. The optical transmission is found to vary with the applied field and is explained as the result of field induced clustering or chain formation. The variation of intensity with polarization of the light could give details of the inter-particle interaction and the relaxation dynamics. These fluids are proposed to have applications in field controlled gratings, optical switches and polarizer. The analysis of light transmission as a function of applied field could give details of the relative strength of particle's interaction with field and the inter-particle interaction. The ionic and steric ferrofluids have different stabilization techniques and this could be studied with respect to magneto optical transmission signals.

The advent of lasers and their increased application in various fields including, research, medicine and common man's day today life, necessitated the protection of sensitive devices and components against high intensity light. The optical limiting devices require nonlinear materials which limit the intensity of light to a threshold value and transparent at lower intensities. The active control of such nonlinear responses by an external electric or magnetic field could be of great interest. The search for nonlinear optical properties in diluted ferrofluids would be interesting

from this point of view since they form interesting microstructures under an applied magnetic field.

Ferrites are enormously studied for the microwave absorbing properties. They can be good electromagnetic interference shields and find applications in electronic circuits and antennae. The flexible composites of ferrite nanoparticles with polymers such as poly vinyl alcohol are more advantageous. The uniform dispersion of fillers in matrix can be achieved if the composites are mixed in solution preferably suspensions such as ferrofluids. Thick films of the composites can be made from PVA based ferrofluids and can be mould into desired size and shape. The volume fraction of the magnetic component can be varied for tuning the total absorbance.

The nanofluids research has been intensified due to the want of highly efficient thermal management systems for energy saving in electronic, automotive and power plants industry. The addition of nanoparticles in coolant liquids is found to be effectively improving the heat transfer properties. Ferrofluids are known be good coolants in loud speakers. The drastic enhancement in the thermal conductivity in ferrofluids with applied magnetic field has made them promising for externally controllable coolants and could especially applied in space systems and nuclear power plants. Nanofluids as coolants would allow smaller size and better positioning of radiators in automobiles owing to their high heat exchanging efficiency.

Here the main objectives of the present investigation can be summarized as follows.

#### **1.11.1 Objectives**

- Synthesis of pure Nickel nanoparticles by auto combustion technique
- Synthesis of nanofluid based on nickel in kerosene by high energy ball milling process
- Synthesis of kerosene based iron oxide and cobalt substituted iron oxide ferrofluids by co-precipitation at ambient temperatures.

- Synthesis of  $Mn_{0.6}Zn_{0.4}Fe_2O$  ferrofluids in water and kerosene by controlled co-precipitation technique.
- Synthesis of biocompatible ferrofluids of SPIONs (Super paramagnetic iron oxide nanoparticles) in water and silica modified SPIONs in poly ethylene glycol.
- Optimization of the preparation conditions for ferrofluids.
- Structural and magnetic characterization of the prepared fluids by XRD technique, TEM, Selected Area Electron diffraction and SQUID magnetometer measurements.
- Magneto optical dichroism measurements on the ferrofluids
- Nonlinear optical measurements on the prepared fluids by z scan technique
- Thermal conductivity measurements of ferrofluid
- Microwave studies on PVA composite
- Correlation of results

*References*

1. H. S. Nalwa, nanostructured materials and nanotechnology: an introduction to modern concepts in nanoscience, 2<sup>nd</sup> ed. *Wiley John & Sons* (2006)
2. George C. Hadjipanayis, Nanophase Materials: Synthesis - Properties – Applications, *Springer* (1994)
3. X battle and A. Labarta, *J. Phys.D: Appl.Phys.* **35** R15 (2002)
4. V. Sunny, T. N. Narayanan, D.Sakthi kumar, Y.Yoshida, P.A.Joy and M R Anantharaman, *Nanotechnology*, 17(2006) 4765-4772
5. K. Lance Kelly, Eduardo Coronado, Lin Lin Zhao, and George C. Schatz *J. Phys. Chem. B* **107** 668-677 (2003)
6. Stephan Link and Mostafa A. El-Sayed, *J. Phys. Chem. B* **103** 4212-4217 (1999)
7. M. Claudia Troparevsky,a) Leeor Kronik,b) and James R. Chelikowsky, *J.Chem. Phys.* **119** 2284-87 (2003)
8. Michael U. Niemann, Sesha S. Srinivasan, Ayala R. Phani, Ashok Kumar, D. Yogi Goswami, and Elias K. Stefanakos, *J. Nanomater.* 950967 (2008)
9. J. C. Slater, *Rev. Mod. Phys.* **25** 199 (1953)
10. J C Slater, , *Phys. Rev.* **52** 198 (1937)
11. L. Pauling, *PROC. N. A. S. Physics:* **39** 551 (1953)
12. S. J. Blundell, Magnetism in condensed matter, *Oxford press* (2003)
13. B D Cullity, *Introduction to magnetism and magnetic materials*, II edition
14. C. Kittel, *Phys.Rev.* **70** 965-971(1946)
15. C Tannous and J Gieraltowski , *Eur. J. Phys.* **29** 475–487 (2008)
16. C. P. Bean and J. D. Livingston, *J.Appl.Phys.* **30** 120 (1949)
17. M. Knobel, W. C. Nunes, L. M. Socolovsky, E. De Biasi, J. M. Vargas, and J. C. Denardin, *J. Nanoscience and Nanotechnology* **8** 2836–2857 (2008)

18. G. M. Pastor, J. Dorantes-Da, vila, and K. H. Bennemann, *Phys. Rev. B* **40** 7462-54 (1989)
19. J. P. Chen, C. M. Sorensen, K. J. Klabund, and G. C. Hadjipanayis, *Phys.Rev B* **51** 11527 (1995)
20. Feng Liu, S. N. Khanna, and P. Jena , *Phys. Rev. B* **43** 8179-8182 (1991)
21. A. J. Cox, J. G. Louderback, and L. A. Bloomfield, *Phys. Rev. Lett.* **71** 923 – 926 (1993)
22. M. E. Fisher and A. E. Ferdinand, *Phys. Rev.Lett.* **19** 169-172 (1967)
23. Jun Wang, Wei Wu, Fan Zhao and Guo-meng Zhao, *Appl. Phys. Lett.* **98**, 083107 (2011)
24. V. I. Nikolaev and A. M. Shipilin, *Physics of the Solid State*, **45** 1079–1080 (2003).
25. R. H. Kodama, *J. Magn. Magn. Mater.* **200** 359-372 (1999)
26. J. S. Moodera, T.H. Kim, C. Tanaka and Cornelis h. De Groot, *philos. Mag. B.* **80** 195-206 (2000)
27. Chao Liu, Bingsuo Zou, Adam J. Rondinone, and Z. John Zhang *J. Am. Chem. Soc.* **122**, 6263-6267 (2000)
28. R. Arulmurugan, G. Vaidyanathan, S. Sendhilnathan, B. Jeyadevan, *J. Magn. Magn. Mater* **298** 83–94 (2006)
29. L. D. Tung, V. Kolesnichenko, D. Caruntu, N. H. Chou, C. J. O’Connor, and L. Spinu, *J. Appl. Phys.*, **93** 7486-88 (2003)
30. L.D. Tung, V. Kolesnichenko, G. Caruntu, D. Caruntu, Y. Remond, V.O. Golub, *Physica B* **319** 116-121 (2002)
31. Sun, Y., Kwok Y. C. and Nguyen, N. T. *Lab Chip.* **7** 1012–1017 (2007).
32. R.E. Rosensweig, *Ferrohydrodynamics*, Cambridge University Press, 1985
33. Mao, Leidong.; and Koser, Hur, *Nanotechnology.* 2006, 17, S34–S47

## *Chapter 1*

---

34. Melikhov, Y.; Lee, S. J.; Jiles, D. C.; Schmidt, D. H.; Porter, M. D.; Shinar, R. *J. Appl. Phys* **93** 8438-8440 (2003)
  35. K.Nakatusuka, *J. Magn. Magn. Mater.* **122** 387-394 (1993)
  36. J. A. Eastman, S. U. S. Choi, S. Li, W. Yu, L. J. Thompson *Appl. Phys. Lett.* **78** 718-20 (2001)
  37. T. T. Baby and S. Ramaprabhu, *Nanoscale Res. Lett.* **6** 289 (2011)
  38. Tessy Theres Baby and S. Ramaprabhu, *J. Mater. Chem.* **21** 9702 (2011)
  39. John Philip, P. D. Shima, and Baldev Raj, *Appl. Phys. Lett.* **91** 203108-10 (2007)
- (a). Ph. D thesis, E. Veena Gopalan, Dept. of Physics, Cochin University of Science and Technology (2008).
- (b). [www.tu-chemnitz.de/physik/OFGF/research/magnetic\\_recording](http://www.tu-chemnitz.de/physik/OFGF/research/magnetic_recording).

## *Chapter 2*

### **Experimental Techniques**

The developments in material science demands ingenious synthesis methodologies along with the simultaneous characterization of intermediate stages employing sophisticated characterization/analytical tools specific for low dimensions. The first part of this chapter describes the synthesis methodologies adopted in the present study. Conventional, modified as well as novel techniques were employed for the preparation of magnetic metal and oxide fluids. These magnetic nanofluids are characterized using sophisticated analytical tools namely X-ray diffraction, scanning electron microscopy, transmission electron microscopy, energy dispersive X-ray spectroscopy, Fourier transform infrared spectroscopy, Raman spectroscopy and UV-Vis-NIR spectroscopy. Details of magnetic characterization tools like vibrating sample magnetometer, SQUID magnetometer are also mentioned. Experimental setup for the determination of magneto optic, microwave and nonlinear optical properties of materials are explained in the latter section of this thesis.

## **2.1 Synthesis of metal and metal oxide nanoparticles and fluids**

Recently magnetic nanoparticles are extensively being investigated due to their wide and important applications in medicine, electronic industry and ferrofluid technology. The main difficulty encountered is the synthesis of monodispersed nanoparticles. Nanoparticle synthesis methodology can be broadly classified into two, namely, physical and chemical [1, 2]. *Physical methods* include inert gas evaporation technique, sputtering, sonication, laser pyrolysis, high energy ball milling [2-4]. Meanwhile *chemical methods* often used are sol-gel process, wet co-precipitation, UV irradiation, thermal decomposition of metal carbonyls, inverse micelle technique, electrode deposition, chemical reduction of metal salts [4-7] etc. In the present work the nanoparticles were prepared by both top-down as well as bottom-up approaches and the details of which are described below.

### **2.1.1 Sol-gel method**

Sol-gel process [8-9] is widely used for the synthesis of metal oxide nanoparticles. In this process, inorganic metal salts like nitrates, chlorides or sulphates are dissolved in an organic solvent to form the sol which is allowed to undergo gelation forming highly porous gel. Chemical reaction in the first stage of the process leads to the formation of a network of metal hydroxides. Gelation takes place when all the hydroxide species are linked in a single network like structure. This gel is a thick and porous solid structure surrounding the interconnecting pores and is a polymer of hydroxides, formed in three dimensions. By heating, the solvent can be removed completely and highly porous and ultrafine powder can be obtained. Here the same technique is devised to synthesize pure metal nanoparticles of Ni. The gel formation is followed by a violent exothermic reaction that causes a reduction of the complex in its own environment yielding highly porous and pure Ni nanoparticles.

### **2.1.2 Chemical co-precipitation technique**

Ferrofluids are easily synthesized by chemical co precipitation of ferrite nanoparticles from metal salts (chlorides, nitrates and sulphates) followed by *in situ* surface modification with surfactant and dispersing in selected carrier liquid. The super saturation is attained by careful control over the heating rate and pH by adding NaOH or NH<sub>4</sub>OH and the concentration of the starting solution of salts. This can provide control over the particle size as well. The nucleation and growth decides the crystallinity, size and size distribution. The lower particle size can be achieved with creating nucleation faster and arresting the growth by varying the super saturation as well as introducing surfactants. Iron oxide and cobalt substituted ferrites are synthesized by supersaturating with ammonium hydroxide solution. Chlorides and sulphates of iron and cobalt are used as precursors. And the reaction was carried out at room temperature and elevated temperature with increasing cobalt substitution. The manganese Zinc ferrites were precipitated from chlorides of Mn, Zn and Fe and super saturation is attained by boiling NaOH solution under vigorous stirring. The surface modification of nanoparticles with required surfactant can easily attained by this method and hence is better for ferrofluid synthesis.

### **2.2 High energy ball-milling**

High energy ball-milling (HEBM) was developed in 1970s as an industrial process to synthesize new alloys and phase mixtures. This is a powder metallurgical process which allows the preparation of alloys and composites which cannot be synthesized by conventional techniques. This top-down technique is widely employed in research of nanomaterials mainly to achieve reduced grain sizes of particles. Ball-milling devices (BMDs) come in a variety of designs like tumbler mills, attrition mills, shaker mills, vibratory mills, planetary mills etc [10].

### **2.2.1 Planetary ball-mill**

In the present work a planetary type ball-milling device by Fritsch model Pulverisette 7 (figure 2. 1) was used for the HEBM studies on zinc ferrite and cadmium ferrite samples. In a planetary type BMD there are two grinding bowls, with heavy and hard grinding balls inside, fixed on diametrically opposite points of a rotating circular platform and capable of rotating about their own axis. The platform and the bowls rotate in opposite directions. The motion resembles the planetary motion of a planet. The grinding balls inside the bowls are constantly acted by centrifugal force, and due the two simultaneous rotatory motions the direction to which the centrifugal force is acting changes abruptly at regular intervals (figure 2.2). This produces two kinds of motion on the grinding balls. The grinding balls running along the walls of the bowl, and the balls striking the diametrically opposite side of the wall. The first kind of motion produces frictional effect and second kind of motion causes high impact between the balls and the material inside the bowl. The impact energy is many times greater compared to conventional grinding devices resulting excellent grinding performance in a shorter time. After the bowls are charged with the powder, they are sealed with O rings to minimize atmospheric contamination. Wet milling is usually done by introducing an organic fluid in the bowl, in order to prevent wear of the bowls and the sides of the bowls.



**Figure 2.1: Planetary ball-milling unit**

The following parameters of a BMD determines the size reduction that can be achieved by milling [11]

- Type of mill
- Milling atmosphere
- Milling media
- Intensity of milling
- Ball to powder weight ratio (BPR)
- Milling time
- Milling temperature

The reduction in grain size is accomplished by the kinetic energy transfer from balls to powder. Since the kinetic energy of the balls depend on their mass and velocity, materials with high density are preferred for the as the balls. Tungsten carbide or steel are the commonly employed material for making grinding balls. In the present study vials with a thick internal coating of tungsten carbide and tungsten

carbide balls were used for milling. The high density balls ( $14750 \text{ kg/m}^3$ ) are suitable for grinding ceramics like zinc and cadmium ferrites.

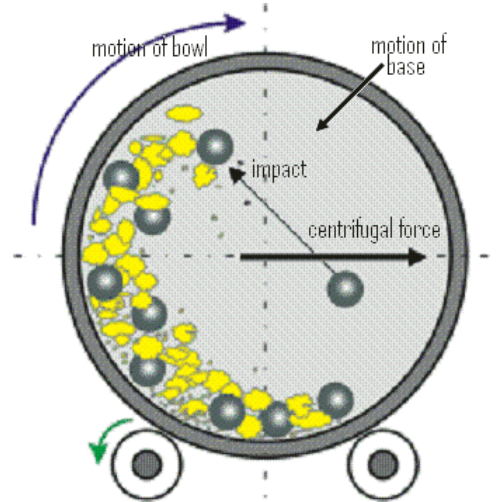


**Figure 2.2: Schematic of the ball-movement**

In any milling experiment the grain size reduction is rather rapid in the initial stages and slows down after reaching a maximum size reduction. The mechanism of grain size reduction is understood as the result of formation of an array of dislocations produced by atomic level strains caused by kinetic energy transfer. Initially this process extends the entire sample, but after a particular level of size reduction very high stress levels are required to continue the process. In addition to this, temperature developed inside the bowls is a prohibitive factor for size reduction beyond a limit. The impact speed is a decisive factor which determines the kinetic energy transfer. The ball-bowl contact time is given by the relation

$$t = (1 + 1.2e) \sqrt{\frac{\pi m}{30YR}} \quad 2.1$$

where  $Y$  is the yield strength of the bowl,  $R$  is the ball radius,  $e$  is the coefficient of restitution of the bowl's inner walls and  $m$  is the mass of the ball [12].

### 2.3 X-Ray Diffraction Analysis

X-ray diffraction patterns have been widely used in nanoparticles research as a primary characterization technique for obtaining features like crystal structure, crystallite size, lattice constants and strain.

In XRD a collimated beam of X-ray with a wavelength of 1.5406Å is incident on a specimen and is diffracted by the crystalline planes in the specimen according to the Bragg's law [13]

$$n\lambda = 2d\sin\theta \quad (2.2)$$

where  $\lambda$  is the wavelength of the X-radiation,  $n$  is an integer,  $d$  is the spacing between atomic planes in the crystalline planes and  $\theta$  is known as diffraction angle. The intensity of the diffracted x-rays was measured and plotted as a function of diffraction angle  $2\theta$ . From the  $2\theta$  values of the peaks, the lattice spacing ( $d$ ) values are calculated using the equation (2.2). we have for any plane with index (h k l)

$$d_{hkl} = \frac{1}{\sqrt{\frac{h^2}{a^2} + \frac{k^2}{b^2} + \frac{l^2}{c^2}}} \quad (2.3)$$

$$\text{when } a = b = c, \quad d_{hkl} = \frac{a}{\sqrt{h^2 + k^2 + l^2}} \quad (2.4)$$

Sample identification can be easily done by comparing the experimental pattern to that in the International Centre for Diffraction Data (ICDD) file. Except for single crystalline particles, the randomly oriented crystals in nanoparticles cause broadening of the diffraction patterns. The effect becomes more pronounced, when the crystallite size is of the order of few nanometers. The simplest and most widely used method for estimating crystallite size is from the Full Width at Half Maximum (FWHM) of a diffraction peak by Debye-Scherrer formula [14].

$$D = \frac{0.9\lambda}{\beta \cos \theta} \quad (2.5)$$

where 'D' is the crystallite size,  $\lambda$  is the wavelength of the X-radiation,  $\beta$  is the angular width (in radians) which is equal to the (FWHM). Rigaku Dmax– C, X-ray Powder Diffractometer was used here to obtain the X-ray diffraction pattern of the samples using Cu K $\alpha$  lines.

#### 2.4 Transmission Electron Microscopy (TEM)

Transmission Electron Microscopy is a straight forward technique to determine the size and shape of the nanostructured materials as well as to obtain structural information. In TEM, electrons are accelerated to 100KeV or higher projected on to a thin specimen by means of a condenser lens system, and penetrate in to the sample [15]. TEM uses transmitted and diffracted electrons which generates a two dimensional projection of the sample. The principal contrast in this projection or image is provided by diffracted electrons. In bright field images the transmitted electrons generate bright regions while the diffracted electrons produce dark regions. In dark field image the diffracted electrons preferentially form the image. In TEM, one can switch between imaging the sample and viewing its diffraction pattern by changing the strength of the intermediate lens. The greatest advantage that TEM offers are the high magnification ranging from 50 to  $10^6$  and its ability to provide both image and diffraction information from a single sample.

The high magnification or resolution of TEM is given by

$$L = \frac{h}{\sqrt{2mqV}} \quad (2.6)$$

where  $m$  and  $q$  are the electron mass and charge,  $h$  the Planck's constant and  $V$  is the potential difference through which the electrons are accelerated.

The schematic of a transmission electron microscope is shown in figure (2.3). From the top down, the TEM consists of an emission source, which may be a tungsten filament, or a lanthanum hexaboride (LaB<sub>6</sub>) source.

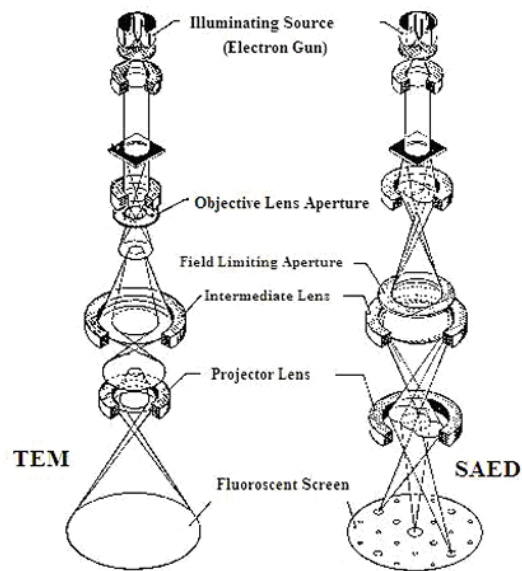


**Figure 2.3 Transmission Electron Microscope for imaging and Selected Area Diffraction Pattern**

Typically a TEM consists of three stages of lensing. The stages are the condenser lenses, the objective lenses, and the projector lenses. The condenser lenses are responsible for primary beam formation, whilst the objective lenses focus the beam down onto the sample itself. The projector lenses are used to expand the beam onto the phosphor screen or other imaging device, such as film. The magnification of the TEM is due to the ratio of the distances between the specimen and the objective lens' image plane imaging systems in a TEM consist of a phosphor screen, which may be made of fine (10-100 $\mu$ m) particulate zinc sulphide, for direct observation by the

operator. Optionally, an image recording system such as film based or doped YAG screen coupled CCD's. High resolution transmission electron microscope (HRTEM) [4] can generate lattice images of the crystalline material allowing the direct characterisation of the samples atomic structure. The resolution of the HRTEM is 1nm or smaller. However, the most difficult aspect of the TEM technique is the preparation of samples.

Joel JEM-2200 FS TEM was used here for carrying out the different electron microscopic studies. Electron Diffraction and HRTEM images obtained along with the images helped in the material characterisation to great extent.

#### **2.4.1 Selected Area Electron Diffraction Pattern (SAED)**

Selected area diffraction offers a unique capability to determine the crystal structure of individual nanomaterials and the crystal structure of the different parts of a sample. A small area of the specimen can be selected from a high resolution transmission image and its electron diffraction pattern (rings or spots) produced on the screen of the microscope by making appropriate arrangement in the lenses of TEM. This is an optional arrangement in HRTEM. The arrangement for taking the diffraction pattern is shown in figure (2.3). The SAED allows the researcher to determine lattice constant of the crystalline material which can help in species identification. Basically diffraction patterns are distinguishable as spot patterns resulting from single crystal diffraction zones or ring patterns are obtained from the randomly oriented crystal aggregates (polycrystallites). For nanocrystallites, the diffraction patterns will be a diffused ring patterns. The 'd' spacing between lattice planes can be estimated radius  $r$  of the diffracted rings from the relation  $\lambda L = rd$ , if the camera constant  $\lambda L$  is known. The estimation of  $d$  values enable us to describe the crystal structure of the crystalline specimen [16-17].

#### **2.4.2 Energy Dispersive X-ray Spectroscopy (EDS)**

Energy dispersive X-ray spectrometer (EDS) attached to the transmission electron microscope analyses characteristic X-ray radiation emitted from the specimen when the electron beam interact with the specimen. The main use of EDS is to accurately determine the composition of the sample under investigation. Upon exposing the samples to high energy electron beams the various atoms present in the sample emit characteristic X-rays which can be observed as several distinct peaks on an energy scale. The intensities of the peaks can be compared with the peaks of a standard sample to obtain the relative amounts of each atomic species, whereby accurate composition of the sample can be determined. The use of EDS has been demonstrated in oxide nanoparticle research in a number of reports [18-19].

#### **2.5 Scanning Electron Microscopy (SEM)**

Scanning electron microscopy (SEM) is one of the most widely used techniques used in characterisation of nanomaterials and nanostructures. It provides the image of the morphology and microstructures of the bulk and nanostructured materials and devices. The resolution of SEM approaches a few nanometers and the instrument operates in the range of 10-30,000. SEM is carried out by scanning an electron beam over the samples surface and detecting the yield of low energy electrons (secondary electrons) and high energy electrons (backscattered) according to the position of the primary beam. The secondary electrons which are responsible for the topological contrast provide mainly information about the surface morphology. The backscattered electrons which are responsible for the atomic number contrast carry information on the samples composition [15, 21]. A new generation of SEM has emerged and is an important tool to characterize nanostructured materials. In this SEM, Field Emission Gun provides the electron beam and the resolution is as high as 1nm.

JSM-6335 FESEM Scanning Electron Microscope was employed to check the morphology of our samples.

### **2.6 Fourier Transform Infrared Spectroscopy (FTIR)**

Vibrational motion of chemical bonds occurs in the infrared region of the energy beam. The Fourier Transform Infrared Spectroscopy exploits this phenomenon. When a material is exposed to IR energy this energy couples with the energy of the sample. If the impinging IR energy is in resonance with the vibration of the chemical bond in the sample the intensity of the beam is measured before and after it interacts with the sample. The incident radiation can be detected in transmission or reflection experiments. The intensity is then plotted as a function of the frequency in the IR spectrum [22]. Thus infrared spectroscopy is a useful technique for characterizing materials and obtaining information on the molecular structure, dynamics and environment of a compound. In an infrared spectrum, the absorption or transmittance peaks correspond to the frequencies of vibrations between the bonds of the atoms making up the material. From the characteristic peaks, different functional groups present in the compound can be identified. This aspect makes infrared spectroscopy quite useful in material characterization. FTIR spectra of the samples were taken using Thermo Nicolette Avatar DTGS model spectrophotometer.

### **2.7 Raman Spectroscopy**

Raman spectroscopy is used to identify different molecules and even functional groups within larger molecules. The bonds formed between atoms have specific vibrational frequencies that correspond to the atom's masses and the strength of the bond between them. Complex molecules therefore exhibit many peaks and can be readily identified by the pattern or "fingerprint" created by those peaks. As such, there are many uses for micro Raman spectrometers as they can non-destructively

identify microscopic samples or microscopic areas of larger samples. When an intense monochromatic light beam impinges on the sample, the electric field of the incident radiation distorts the electron clouds that make up the chemical bonds in the sample, storing some energy. When the field reverses as the wave passes, the distorted electron clouds relax and the stored energy is reradiated. Although, the incident beam may be polarized so that the electric field is oriented in a specific direction with respect to the sample, the scattered beam is reradiated in all directions, making possible a variety of scattering geometries. Most of the stored energy is reradiated at the same frequency as that of the incident exciting light. This component is known as the Rayleigh scattering and gives a strong central line in the scattering spectrum. However, a small portion of the stored energy is transferred to the sample itself, exciting the vibrational modes. The vibrational energies are deducted from the energy of the incident beam and weak side bands appear in the spectrum at frequencies less than that of the incident beam. These are the Raman lines. Their separation from the Rayleigh line is a direct measure of the vibrational frequencies of the sample [23].

## **2.8 UV-Visible Spectroscopy**

Ultraviolet-visible spectroscopy or ultraviolet-visible spectrophotometry (UV/ VIS) involves the spectroscopy of photons in the UV - Visible region. It uses light in the visible and adjacent near ultraviolet and near infrared ranges. In this region of the electromagnetic spectrum, molecules undergo electronic transitions. The instrument used in ultraviolet-visible spectroscopy is called a UV/Vis spectrophotometer. It measures the intensity of light passing through a sample ( $I$ ), and compares it to the intensity of light before it passes through the sample ( $I_0$ ). The ratio  $I / I_0$  is called the transmittance, and is usually expressed as a percentage (%T). The absorbance  $A$  is based on the transmittance [24].

$$A = -\log(\%T)$$

(2.7)

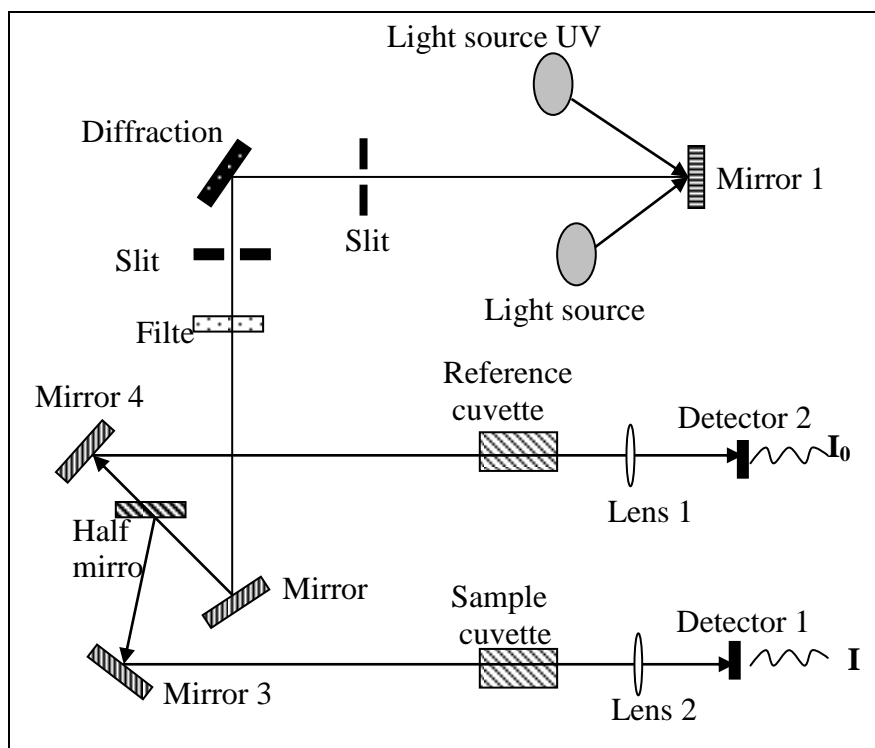


Figure 2.4: Schematic diagram of UV-Visible spectroscopy.

The functioning of this instrument is relatively straightforward. A beam of light from a visible and/or UV light source (colored red) is separated into its component wavelengths by a prism or diffraction grating. Each monochromatic (single wavelength) beam in turn is split into two equal intensity beams by a half-mirrored device. One beam, the sample beam (colored magenta), passes through a small transparent container (cuvette) containing a solution of the compound being studied in a transparent solvent. The other beam, the reference (colored blue), passes through an identical cuvette containing only the solvent. The intensities of these light

beams are then measured by electronic detectors and compared. The intensity of the reference beam, which should have suffered little or no light absorption, is defined as  $I_0$ . The intensity of the sample beam is defined as  $I$ . Over a short period of time, the spectrometer automatically scans all the component wavelengths in the manner described. The ultraviolet (UV) region scanned is normally from 200 to 400 nm, and the visible portion is from 400 to 800 nm.

The absorption coefficient is calculated from the spectrum by dividing the  $\alpha d$  value by the thickness and it is plotted against the photon energy for polymer thin films. The intercept of this plot on the photon energy axis gives the band gap of the polymer. The probable energies for the transitions were estimated from the Tauc plot by plotting the  $(\alpha hv)^{1/2}$  vs.  $hv$  graphs.

## **2.9 Magnetic Characterisation**

### **2.9.1 Vibrating Sample Magnetometer (VSM)**

A vibrating sample magnetometer (VSM) operates on Faraday's Law of induction, which tells us that a changing magnetic field will produce an electric field. This electric field can be measured and provides us information about the changing magnetic field. A VSM is used to measure the magnetic behaviour of magnetic materials. Using VSM the hysteresis loop parameters namely saturation magnetisation ( $M_s$ ), coercive field ( $H_c$ ), remanence ( $M_r$ ) and squareness ratio ( $M_r/M_s$ ) can be derived. The schematic of a vibrating sample magnetometer is given in figure (2.5).

In a VSM, the sample to be studied is placed in a constant magnetic field. If the sample is magnetic, this constant magnetic field will magnetize the sample by aligning the magnetic domains or the individual magnetic spins, with the field. The stronger the constant field, the larger the magnetisation. The magnetic dipole moment of the sample will create a magnetic field around the sample, sometimes called the magnetic stray field. As the sample is moved up and down, this magnetic stray field

change as a function of time and can be sensed by a set of pick up coils. A transducer converts a sinusoidal ac drive signal provided by a circuit located in the console in to a sinusoidal vertical vibration of the sample rod and the sample is thus made to undergo a sinusoidal motion in a uniform magnetic field. Coils mounted on the pole pieces of the magnet pick up the signal resulting from the sample motion.

The alternating magnetic field will cause an electric field in the pickup coil as according to Faradays law of induction, the current will be proportional to the magnetisation of the sample. The greater the magnetisation, larger is the induced current. The induction current is amplified by a transimpedance amplifier and a lock-in amplifier. The various components are interfaced via a computer. Controlling and monitoring software, the system can tell you how much the sample is magnetized and how magnetisation depends on the strength of the constant magnetic field. For particular field strength, the corresponding signal received from the probe is translated into a value of magnetic moment of the sample. When the constant field varies over a given range, a plot of magnetisation versus magnetic field strength is generated.

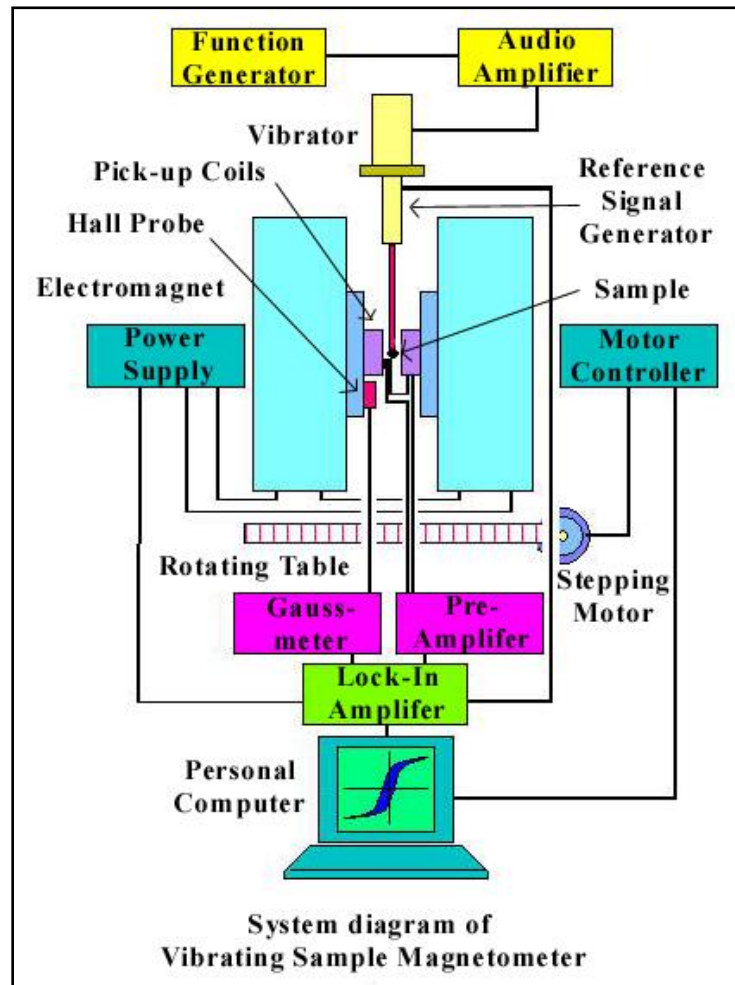


Figure 2.5 Vibrating Sample Magnetometer

The dipole moment is induced in the sample when it is placed in a uniform magnetic field be  $M$ . Then the amount of magnetic flux linked to the coil placed in the vicinity of this magnetic field is given by

$$\phi = \mu_0 n \alpha M \quad (2.8)$$

where ' $\mu_0$ ' is the permeability of free space, ' $n$ ' the number of turns per unit length of coil and  $\alpha$  represents the geometric moment decided by position of moment with respect to coil as well as shape of coil.

Anharmonic oscillator of the type,

$$Z = Z_0 + A \exp(j\omega t) \quad (2.9)$$

induces an emf in the stationary detection coil. The induced emf is given by

$$V = -\frac{d\phi}{dt} = -j\omega\mu_0 nMA \left(\frac{\partial\alpha}{\partial z}\right) e^{j\omega t} \quad (2.10)$$

If amplitude of vibration ( $A$ ), frequency  $\omega$  and  $\frac{\partial\alpha}{\partial z}$  are constant over the sample zone then induced voltage is proportional to the magnetic moment of the sample. A cryogenic setup attached to the sample permits low temperature measurements. This is the basic idea behind VSM [25-27]

The magnetisation measurements (hysteresis loop) were carried out employing DMAX VSM. The magnetisation isotherms over a wide temperature range were taken for MCE measurements.

### 2.9.2 Field Cooled and Zero Field Cooled Measurements

Zero Field Cooled (ZFC) measurements provide a means of investigating various magnetic interactions. First a sample is cooled to liquid helium temperatures under zero applied magnetic fields. Then small uniform external field is applied and the net magnetisation is measured while heating the sample at a constant rate. For small magnetic particles, this curve has a characteristic shape. As the particle cools in a zero applied magnetic field, they will tend to magnetize along the preferred crystal directions in the lattice, thus minimizing the magneto-crystalline energy. Since the orientation of each crystallite varies, the net moment of the systems will be zero. Even when a small external field is applied the moments will remain locked into the preferred crystal directions, as seen in the low temperature portion of the ZFC curve.

As the temperature increases more thermal energy is available to disturb the system. Therefore more moments will align with the external field direction in order to minimize the Zeeman energy term. In other words, thermal vibration is providing the activation energy required for the Zeeman interaction. Eventually the net moment of the system reaches a maximum where the greatest population of moments has aligned with the external field. The peak temperature is called blocking temperature  $T_B$  which depends on particle volume. As temperature rises above  $T_B$ , thermal vibrations become strong enough to overcome the Zeeman interaction and thus randomize the moments [28].

Field cooled measurements proceed in a similar manner to ZFC except that the constant external field is applied while cooling and heating. The net moment is usually measured while heating. However, the FC curve will diverge from the ZFC curve at a point near the blocking temperature. This divergence occurs because the spins from each particle will tend to align with the easy crystalline axis that is closest to the applied field direction and remain frozen in that direction at low temperature. Thermal Remnant Magnetisation (TRM) curves are obtained by cooling field to the measurement start temperature. The field is then removed and the magnetisation is recorded as a function of temperature while the sample is heated. It is important to note that ZFC, FC and TRM are non equilibrium measurements [29-30]. Care must be taken to ensure the same heating rate is used during the measurements in order to properly compare the measurements.

### **2.9.3 SQUID Magnetometer**

SQUID magnetometer is the instrument used to measure extremely sensitive magnetic fields of the order of  $10^{-14}$  T. The superconducting quantum interference device (SQUID) consists of two superconductors separated by thin insulating layers

to form two parallel Josephson junctions. The great sensitivity of the SQUID devices is associated with measuring changes in magnetic field associated with one flux quantum ( $h/2e$ ). The basic principle that follows in a SQUID magnetometer is that, if a constant biasing current is maintained in the SQUID device, the measured voltage oscillates with the changes in phase at the two junctions, which depends upon the change in the magnetic flux. Counting the oscillations allows evaluating the flux change which has occurred. Hence, when the sample is moved through the superconducting magnetic coils, a flux change is induced in the pickup coils. Highly magnetic sample should be moved slowly through the coils in order not to exceed the maximum slewing rate of the electronic system [31].

### **2.10 Transient hot-wire method for thermal conductivity measurement**

The transient hot wire technique is known to be a fast and accurate method for fluid thermal conductivity measurements. The principle of the hot wire method is based on ideal, constant heat generation source, an infinitely long and thin continuous line, dissipating the heat into an infinite test medium. In practice, the ideal case is approximated with a finite long wire embedded in a finite medium. While the wire is electrically heated, the change in resistance of the wire, and hence its temperature, is measured as function of time using a Wheatstone bridge circuitry and a computerized data acquisition system. Finally, the thermal conductivity value is determined from the heating power and the slope of temperature change in logarithmic time [32]. The mathematical expression for thermal conductivity  $k_f$  being

$$k_f = \frac{q}{4\pi} \cdot \frac{1}{d(\Delta T)/d(\ln t)} \quad (2.11)$$

Where  $q$  is the heat produced per unit length per unit time,  $t$  is the time,  $\Delta T$  is the change in temperature in time  $t$ . Thermal conductivity can be calculated directly from the slope of  $\Delta T$  versus  $\ln(t)$ .

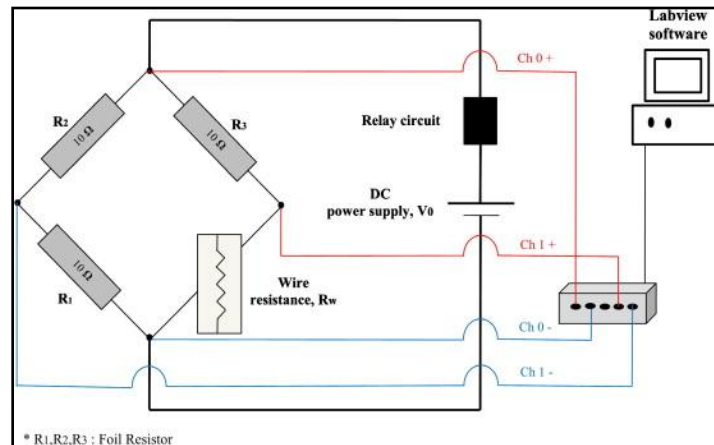


**Figure 2.6: schematic of a hot wire set up for thermal conductivity measurement**

Figure 2.6 is a schematic of transient hot wire set up. The measurement is carried out in short interval of time since the transience is lost otherwise.

**References:**

1. Hari Singh Nalwa. Nanostructures materials and nanotechnology, *Academic Press*, California USA, 2002
2. Dhirendra Bahadur, Satish Vitta, Om Prakash. Inorganic Materials, recent advances. *Narosa Publishing House*. Mumbai India, 2004
3. Vijutha Sunny, T N Narayanan, US Sajeev, PA Joy, D Sakthi Kumar, Yasuhiko Yoshida and M R Anantharaman. *Nanotechnology*, 174765-4772 (2006)
4. T Kameyama, K Sakanaka, A Motoe, T Tsunoda, T Nakanaga, NI Wakayama, H Takeo, K Fukuoda. *J Mater. Sci.* **25** 1058 (1990)
5. V `Sepel`ak, D Baabe, KD Becker. *Journal of Materials Synthesis and Processing*, **8**(5) 333 (2000)
6. Min Nie, Kai Sun, Dennis Desheng Meng. *J Appl Phys* **106** 054314 (2009)
7. Urs O Hafeli, Gayle J Pauer, *J Magn Mag Mater* **194** 76 (1999)
8. Jhunu Chatterjee, Yousef Haik, Ching-Jen Chen. *J Magn Magn Mater* **246** 382 (2002)
9. QA Pankhurst, J Connolly, SK Jones, J Dobson, *J Phys D: Appl Phys* **36** R167 (2003)
10. H. J. Fetch: Proceedings of the NATO advanced study institute on Nanophase materials synthesis, Properties and applications: *Kluwer academic publications* (1994) 18 original.
11. C. Suryanarayana, G. H. Chen, F. H. S. Froes: *Scripta Metallurgica* **26** 1727 (1992)
12. S. D. Shenoy, Ph. D. Thesis, Department of Physics, Cochin University of Science and Technology

13. Charles Kittel, *Introduction to Solid State Physics*, John Wiley and Sons, New York (1997)
14. B.D. Cullity, *Elements of X-ray diffraction*, Philippines, Addison-Wesley Publishing Company, Inc., 2<sup>nd</sup> Edition. California (1978)
15. M. Watt, *The Principles and Practice of Electron Microscopy*, 2<sup>nd</sup> Edition, Cambridge University Press, Cambridge (1997)
16. A. Subramanian, L.D. Marks, *Ultramicroscopy*, **98** 151(2004)
17. C.T. Schamp, W.A. Jesser, *Ultramicroscopy*, **103** 165 (2005)
18. Lawrence E Murr, *Electron and Ion Microscopy and Microanalysis, Principles and Applications*, Mc.Graw Hill Inc.New York,1982
19. C.H. Lin, P.C. Kuo, J. L. Pan, D. R. Huang, *J. Appl. Phys.* **79** 6035(1996)
20. X. Xu, G. Freidman, K. D. Humfeld, S. A Majetich,S A. Asher, *Chem. Mater.***14** 1249 (2002)
21. Linda C. Sawyer and David T. Grubb, *Polymer Microscopy*, 2<sup>nd</sup> Edition. Chapman and Hall, London (1987)
22. Brian Smith, *Infrared Spectral Interpretation-A systematic Approach*, CRC Press, Boca Raton, London, New York, Washington D C, (1999)
23. Brundle, C. R.; Evans, C. A. Wilson, S. Encyclopedia of materials characterisation, *Reed Publishing, USA* (1992).
24. Pankov J.J Optical Processes in Semiconductors, *Printice-Hall, New Jersey, USA* (1971)
25. Simon Foner, *Rev. Sci. Instrum.*, **30** 548 (1959)
26. Joseph A. Pesch, *Rev. Sci. Instrum.*, **54** 480(1983)
27. R.V. Krishnan and A. Banerjee, *Rev. Sci. Instrum.*, **70** (1999) 85
28. J. C. Denardin, A. L. Brandl, M. Knobel, P. Panissod, A. B. Pakhomov, H. Liu, X. X. Zhang; *Phys. Rev. B* **65**, 064422 (2002)

## *Chapter 2*

---

29. Aparna Roy ,V. Srinivas, S. Ram, J. A. De Toro, *J. Appl. Phys.* 100 (2006) 094307
30. L Dormann, D Fiorani, *J. Magn. Magn. Mater.* 415 140-144 (1995)
31. K. Gramm, L. Lundgren, Beckman, *Physica Scripta.* **13**, 93 (1976)
32. P. D. Shima, John Philip and Baldev Raj, *J. Phys. Chem. C* **114**, 18825–18833 (2010)

## *Chapter 3*

### **On the synthesis and characterization of Nickel ferrofluid: Evidence for low temperature magnetic ordering in Nickel nanoparticles**

Oxide free metallic nanofluids of Nickel assume importance owing to the multitude of applications and of great fundamental interest. Synthesis of nanofluids demands careful tuning of the parameters due to the environmental sensitivity of the nanoparticles and stability criteria of the suspensions. Nanofluid of metallic nickel nanoparticles in kerosene are realized by a novel synthetic route. Nickel nanoparticles are synthesized by a modified poly-ol process. Size reduction of these particles together with *in situ* surface modification is performed by high energy ball milling in presence of an oleic acid surfactant. The surfacted particles are dispersed in kerosene to form stable nanofluid and effect of aging is conducted on these suspensions. The structural analysis with X -ray diffraction and electron microscopy confirms the formation of pure nickel nanoparticles with a narrow particle size distribution. Superconducting quantum interference device magnetometry is performed to study the magnetic behavior of the nanoparticles. Evidence for surface spins is observed in magnetization studies and was further verified by a detailed temperature dependant magnetisation studies. This novel synthesis technique employed for the preparation of nickel based ferrofluids could be adopted for the preparation of nanofluids based on other metals.

### **3.1 Introduction**

The colloidal assemblies has immense practical importance with a strong fundamental interest aimed at understanding the self-assembly occurring at molecular length scales [1-2]. Transition metals exhibit important electronic, magnetic and optical properties owing to their electronic configuration. The ultrafine atomic clusters of 3d-transition metals such as iron, nickel and cobalt exhibit modified properties due to quantum size effects and surface effects [3-6]. Their physical properties such as superparamagnetism, saturation process, magnetic anisotropy, surface spin disorder and Curie temperature get modified with particle sizes and shapes [3-7]. Magnetic properties of nano objects are governed by the spins at the particle surface, owing to the large surface to volume ratio. In metallic nanoparticles, the surface symmetry breaking or the spin disorder at the surface could contribute much to the magnetic response. The temperature dependence of the magnetic behaviour has been reported as a result of exchange bias of antiferromagnetic (AFM) oxide shell and surface spin disorder as well [6-8].

Nickel, belonging to the transition d-block elements is one among the ferromagnetic trio that shows room temperature ferromagnetism, with a saturation magnetisation of 57.5 emu/g [1]. Nickel nanoparticles are industrially pursued systems for its catalytic activity and also would form good templates to study the fundamental magnetism in terms of the ferromagnetic surface spin contributions in contrast to the oxide layer at the surface. The nanoparticles owing to their high surface area are sought after as a catalyst in methane cracking, methanation, partial oxidation steam reforming [9-11] and in the synthesis of ferrofluids. They are also applied in pigment industry, component of data storage devices, and in chemical and biological sensing.

Magnetic particles broadly exist in three categories. When the size is fairly large enough, they contain more than a domain and the magnetization reversal occurs by domain wall motion. Nickel, normally a crystalline material with high order and low magneto crystalline anisotropy offers small coercivity in bulk. When the particle size is decreased, such that it has the volume of a single domain, the domain magnetization needs to be rotated. This rotation results in large change in energy determined by the anisotropy of the material. So single domain particles are bound to have large coercivity compared to the multi domain particles. When the particle size is decreased such that the thermal energy is sufficient to fluctuate the magnetization of the entire particle to reverse the vector in a time shorter than the measurement window, the particles behave paramagnetically but with large moments and order randomly. Hence they exhibit superparamagnetism with zero coercivity. Now when the particles are in contact with each other, there exists exchange interaction through the interfaces. Such cases are accomplished with random anisotropy when the anisotropy of individual particles are averaged over the aggregates.

Metal particles being increasingly prone to oxidation with reduction in particle size, they need to be surface passivated against oxidation. Oxides of iron (Fe), nickel (Ni) and cobalt (Co) are either ferro/ferri magnetic or antiferromagnetic in nature [1,12]. Hence magnetic properties of these metal/metal oxide nanoparticles gets modified from the individual metal nanoparticles due to the core-shell exchange interaction [13,14]. The saturation magnetization was found to decrease in the nanosized nickel nanoparticles [15,16] and is explained as the surface contribution either from the symmetry change of the lattice defects or due to the presence of oxide dead layer. Fine clusters of few to few hundred atoms of ferromagnetic metals (Fe, Ni and inter metallic) are found to have increased magnetic moment per atom than the bulk. It has been explained with respect to the decreased dimensionality, the

coordination of atoms [17,18] and the cluster shape. Clusters with smaller surface area decided by the shape, are found to have lower magnetization [17]. Hence the study of the finite size effects in metallic system requires phase pure (oxide free) particles. Attaining pure metallic nanoparticles below the size of 10 nm is challenging.

There are different routes for the synthesis of nickel nanoparticles, such as arc melting submerged in solvent, laser ablation technique, evaporation of metal atoms, microemulsion method, and polymeric ion exchange technique, solution phase chemical reduction and thermal decomposition from organometallics [9,19-21]. Reduction from the aqueous solution of Nickel salts with suitable reducing agents such as sodium borohydride [22] and, hydrazine hydrate are pursued for nanoparticle synthesis. Microemulsion techniques with oil in water are devised to obtain uniform sized nanoparticles with size around 5 nm [23]. The choice of surfactants and optimisation of precipitation condition gives varied results in the properties of the resulting nanoparticles. Sahoo *et. al.* reported laser decomposition of carbonyl vapors to form an aerosol followed by exposure to solvent with surfactant to form monodispersed Ni particles. Poly-ol condensation technique has been widely used for producing nanoparticle where glycols act as complexing as well as reducing agents. Refluxing of the solution for 4-6 hours is required for this synthesis technique. Spray pyrolysis method in which the metal salt solution is finely sprayed onto a reducing environment of hydrogen/nitrogen mixture is particularly used for synthesis of Ni nanoparticles in large quantities [24,25]. Ni nanoparticles being highly prone to oxidation, need to be surface protected in all the preparation techniques.

The magnetic properties are observed to vary with the kind of surfactants in metal nanoparticle systems. Ferromagnetic fine particles are observed to form aggregates due to inter-particle interactions. Nanoparticles of Ni are encapsulated in

various host materials such as silica [26,27] titania [28] and carbon [6,29] which provide high passivation from oxidation. This further reduces the particle-particle interaction and are good systems to study the magnetic properties of isolated moments that exhibit perfect superparamagnetism.

However their dispersion in a suitable solvent and the stability of the resulting fluid are still a challenge on ground. When dispersed in a solution, nanoparticles exhibit rather complex behaviour described in terms of Brownian or Neel relaxation models and studies on these aspects of pure metallic nanosuspensions are significant for various technological applications. Early stages of ferrofluids research searched the metallic fluids for high thermal conductivity and electrical conductivity, where the carrier was liquid metals such as mercury, gallium, tin etc [30]. With tremendous advances in preparation and stabilisation techniques and colloidal chemistry, the ferromagnetic metal fluids can be realised with a number of carrier liquids [19,31-32].

A template consist of Ni nanoparticles dispersed in a carrier fluid, kerosene is ideal for investigating the existence of surface spins in systems resembling Ni/Co/Fe nanoparticles. In the present chapter a synthesis technique for the preparation of large quantity of pure Ni nanoparticles is presented. This method is simple and could be carried out in ordinary laboratory conditions. The obtained particles are polydispersed in size and are non spherical in nature. These particles are used in preparation of nanofluids based on kerosene. Ni nanoparticles and their nanofluids are characterised by a series of elaborate experiments including X-ray diffraction, superconducting quantum interference device (SQUID) magnetometer, high resolution transmission electron microscopy (HRTEM) and micro-Raman analysis. The possibility of cooperative magnetization switching at low temperature is also probed by low temperature magnetisation studies.

### 3.2 Synthesis of Nickel nanoparticles and Nickel nanofluids

The synthesis involves a bottom up approach of a chemical sol-gel route and a top down method of high energy ball milling (HEBM) to reduce the particle size. Nickel nanoparticles were synthesized by a novel technique based on a modified sol-gel auto combustion technique [33]. Nickel nitrate dihydrate ( $\text{NiNO}_3 \cdot 2\text{H}_2\text{O}$ ) was used as the precursor with ethylene glycol as a complexing agent. The gel undergoes a violent exothermic reaction resulting in the formation of a highly porous spongy material. It was further ground to obtain highly crystalline oxide free nanoparticles labeled as Ni P. These nanoparticles were subjected to HEBM (Fritsch Pulverisette 7) which reduces the particle size along with the formation of little oxide phase. The sample was labeled as Ni M. The synthesis parameters were modified by changing the pH of the gel. At the neutral pH, grain size could be tailored to lower size without any oxide impurity. To synthesize nanofluids of Ni, the particles (Ni P) were milled in the presence of surfactant oleic acid in water medium for 30 minutes at a speed of 500 rpm. The particle size reduces and gets *in situ* surfacted with oleic acid while milling. The sample is then retrieved and stirred in slightly basic pH of 7.5, at warm conditions about 40°C. The larger particles were separated by magnetic decantation; water is removed by drying with acetone and lighter particles were dispersed in kerosene. The resultant oleic acid coated nickel nanoparticles dispersed in kerosene is labeled as Ni F. The ageing studies conducted on this Ni F indicate that they are highly stable even after 12 months and hence it has a long shelf life.

### 3.3 Structural and morphological analysis

The crystal structure of as prepared (Ni P) and Ni M powders is determined by X-ray diffraction technique. The diffraction pattern of Ni P and Ni M depicted in figure 3.1a, clearly indicates that the Ni has crystallized in the face centered cubic

structure (ICDD: 040850). Also Ni P is phase pure even though these metallic nanoparticles are highly prone to oxidation. So this novel preparation method for nickel nanoparticles is superior with respect to other methods of preparation . The crystallite size D is calculated using the Debye Scherrer's formula given by

$$D = 0.9\lambda/\beta \cos\theta \quad (3.1)$$

where,  $\lambda$  is the X-ray wavelength (1.5418 Å),  $\theta$  the diffraction angle and  $\beta$  the full width at half maximum of the diffraction peak.. The average size calculated from the maximum intensity peak corresponding to (111) plane is 30 nm for Ni P. The lattice constant is calculated to be 3.55 Å (3.524 Å in ICDD table).

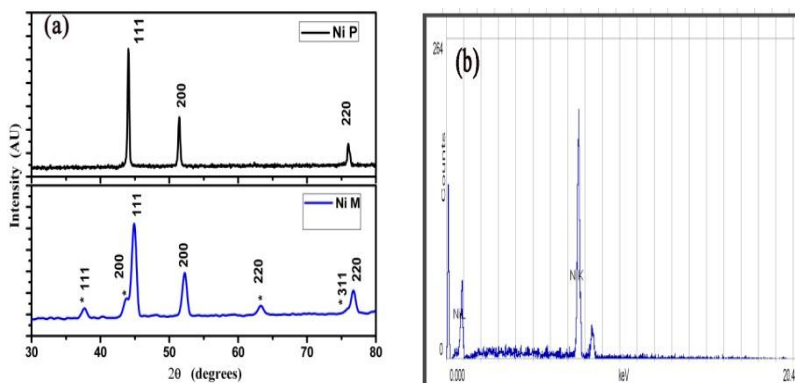


**Figure 3.1: (a) X-ray Diffraction pattern of Ni P and Ni M; \* denotes the peaks corresponding to NiO (b) EDS of Ni P**

The energy dispersive spectrum (EDS) depicted in figure 3.1b reveals that the impurity present in the sample, if any, are below the detection limit of the experiment. The XRD pattern of the Ni M sample shows peak broadening with ball milling indicating reduction in crystallite size. The average crystallite size of Ni in the milled sample is calculated to be 13 nm. It could be observed that ball milling has resulted in

the evolution of impurity peaks corresponding to NiO. This is expected as the Ni nanoparticles are prone to oxidation and since high energy is imparted to the particles during milling, and the surface area increases which causes faster reaction with the environment. The lattice constant reduces to 3.49 Å as evidenced from the diffraction peaks which are shifted towards larger diffraction angle.

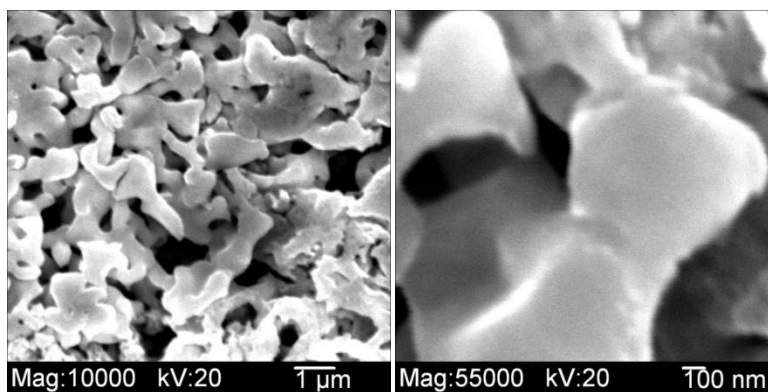


**Figure 3.2: SEM images of as prepared Ni P**

Figure 3.2 depicts scanning electron microscopy (SEM) images of the Ni P sample. It is clearly seen that the system is highly porous and sponge like. The lattice expansion of Ni P samples as observed in X- ray diffraction measurements might be the reason for this highly porous nature.

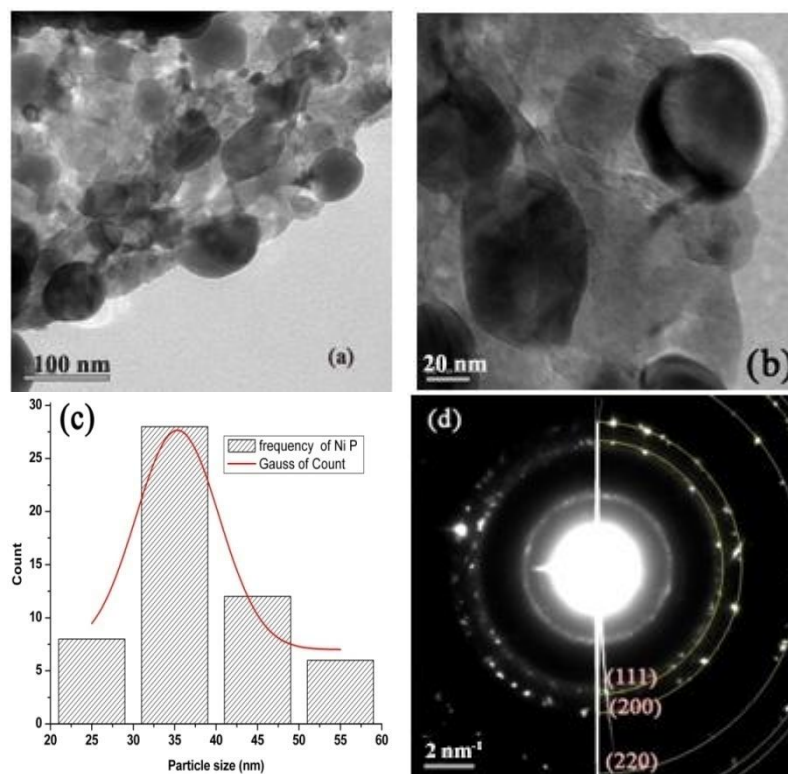


**Figure 3.3:** (a),(b) TEM images of Ni P (c) Particle size distribution and (d) SAED pattern of Ni P

The transmission electron microscopy (TEM) (CM 20 FEG) measurements carried out on Ni P is depicted in figure 3.3. The particles have an average size of 35 nm but also larger particles upto 58 nm are present. It could be seen from the TEM images that the particles are distributed in size (3.3a and 3.3b) and have deviations from the ideal spherical shape. The size distribution is plotted in figure 3.3c. The selected area electron diffraction (SAED) pattern of Ni P (figure 3.3d) corresponds to the fcc structure. The diffraction rings corresponding to (111), (200), and (220) planes of fcc structure of Ni are indexed. It is clear from the sharp diffraction spots in SAED pattern that the particles are highly crystalline in nature.

Figure 3.4a depicts the TEM images of the milled sample, Ni M. The particle size has reduced considerably and are uniformly distributed (figure 3.4b) with an average size of 11 nm and a width of 4 nm. Particles as large as 18 nm are also present in the sample.

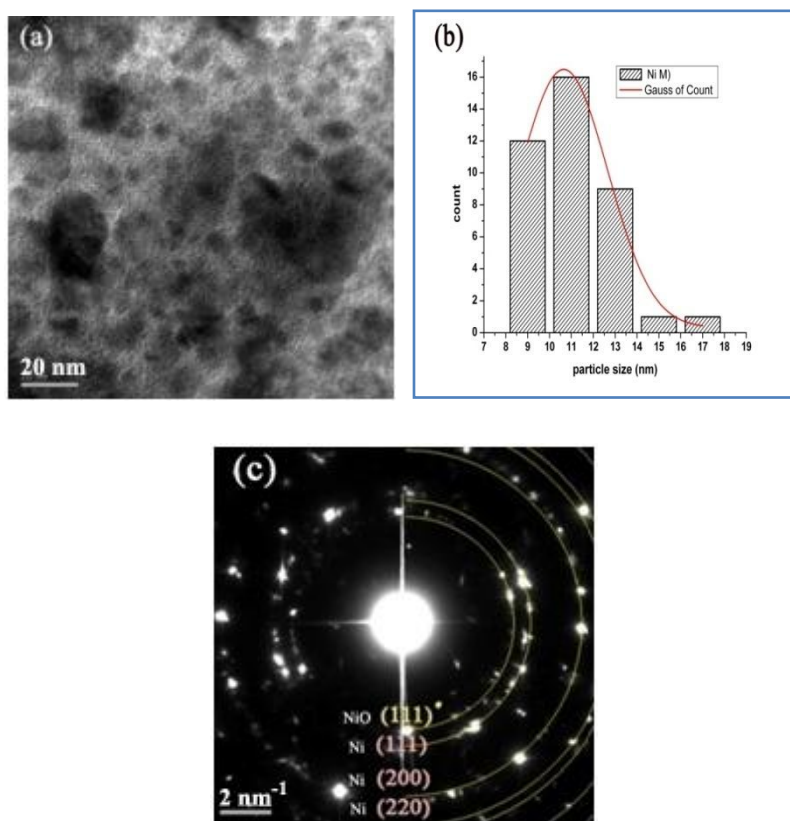
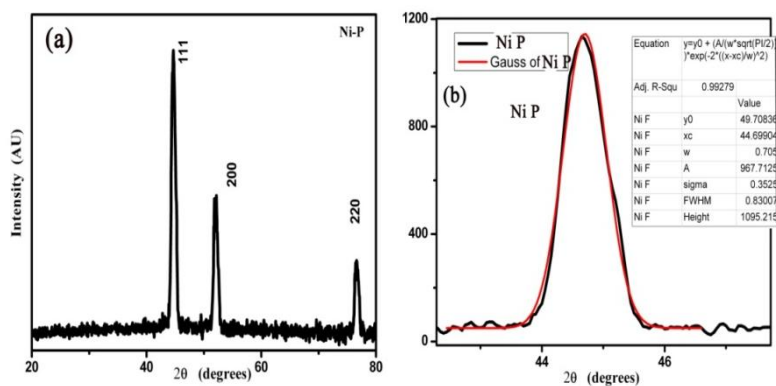


**Figure 3.4: (a) TEM images of Ni M (b) Distribution of particle size (c) SAED pattern of Ni M**

The SAED pattern (figure 3.4c) shows that the particles are randomly oriented with slightly diffused diffraction spots. This spreading of diffraction shows the reduced crystallite size of Ni M. The planes are fit using an fcc structure and

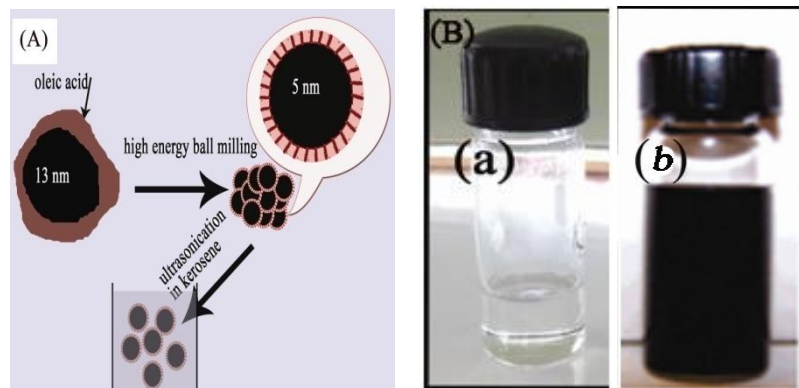
lattice constant of 3.47 Å for nickel and 4.10 Å for NiO. The good agreement proves the presence of NiO in the Ni M sample. This is evident in XRD measurements as well.

Figure 3.5 shows the XRD pattern of nickel synthesised by varying the pH value of the sol to 7 (neutral). The crystallite size from the Scherrer formula gives 11 nm. The peaks are perfectly Gaussian in nature, the lattice parametr is 3.51 Å close to the ICDD value of fcc Ni. So the synthesis route is promising with the neutral pH of the sol which can be the optimum for synthesis of Ni nanoparticles.



**Figure 3.5: (a) The XRD pattern of Ni P prepared with sol of neutral pH (b) (111) peak including the Gaussian fit**

The schematic for the preparation of nanofluid is shown in figure 3.6a. Figure 3.6b is the photograph of nanofluid and base liquid kerosene. Nanoparticles of desired size, selected by the stability criteria, get self-assembled in kerosene to form the nanofluid. The fluid is found to be stable against gravity settling over one year. The stability criteria are collectively decided by the density and magnetisation of the nanoparticles, the viscosity of the carrier liquid. Details are given in section 1.10.1.



**Figure 3.6: (A) Schematic of Ni F preparation from Ni P, (B) Photograph of (a) kerosene and (b) fluid Ni F**

TEM measurements are carried out on suspended particles (Ni F) by dropping the fluid on a copper TEM grid and allowing to dry off the carrier fluid. Figure 3.7a depicts the TEM image of Ni F, revealing narrowly distributed (the width of distribution is  $\sim 1$  nm (inset)) particles with a mean size of 4.5 nm. The stability criteria [30] has selected the size of nickel nanoparticles suspended in kerosene. The SAED pattern (Figure 3.7b) shows the random fcc orientation of single crystalline nanoparticles. The rings corresponding to (200) and (220) planes again confirms the formation of fcc Ni. The HRTEM (JEM 2100F TEM) image (figure 3.7c) of the Ni F particles indicates that the Ni is highly crystalline and is also free from nickel oxide (NiO), that normally appears as a shell with Ni as core. This is an indication that milling the sample in the presence of a surfactant results in shielding the nanoparticles from oxidation even when the size is reduced. To further confirm the absence of NiO formation, micro-Raman studies were carried out on Ni F, and it is depicted in figure 3.7d. There are no signatures for NiO (at  $\sim 500$   $\text{cm}^{-1}$ ) as is observed from micro Raman studies [34] conducted with both 514.5 nm and 633 nm excitation wavelengths.

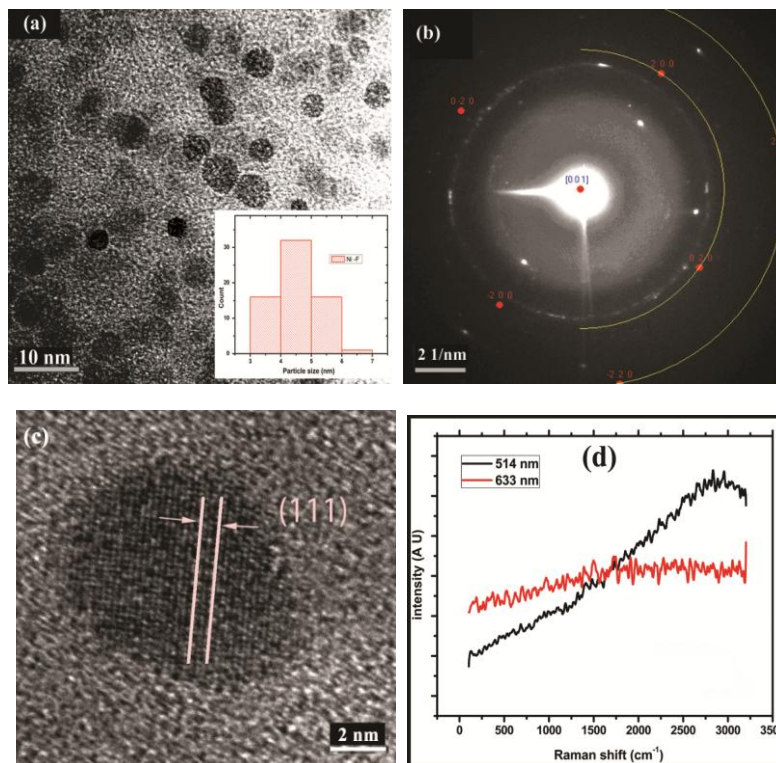


**Figure 3.7:** (a) TEM (inset: particle size distribution), (b) SAED, (c) HRTEM images, (d) micro-Raman spectrum, of the Ni F

The structural analysis by different measurement techniques shows that the synthesis route is easy and superior for Ni nanoparticle synthesis; HEBM could bring down the particle size, and together with surfactants can prevent oxidation. Suspending particles in kerosene could form a size selective process with more or less uniform distribution.

### 3.4 Magnetic measurements

The magnetic measurements were carried out using a SQUID magnetometer (MPMS Quantum Design). Magnetisation isotherms (hysteresis loops) were obtained at different temperatures from room temperature down to 2 K. The temperature

dependent relaxation studies were carried out by field cooled (FC) and zero field cooled (ZFC) moment measurements at a constant applied field. The field cooled isotherms were also measured to explore the presence of exchange bias (EB) expected for the core-shell Ni /NiO samples.

### 3.4.1 Magnetisation measurements on Ni P

Figure 3.8 shows the hysteresis curves obtained for Ni P. The sample was heated to 380 K, a magnetic field of 70 kOe was applied and cooled to the measurement temperature and then the hysteresis curves were measured. Cooling the sample in high applied field causes the moments to align in the field direction. A shift in hysteresis loop is expected when the field is applied in the reverse direction due to the presence of exchange anisotropy. Such anisotropy is expected for ferromagnetic core-antiferromagnetic shell structures in which core and shell spins are coupled at the interface, when the sample is cooled below the Neel temperature [1]. However no exchange bias is observed even when cooled down to 2 K confirming the purity of the Ni nanoparticles.

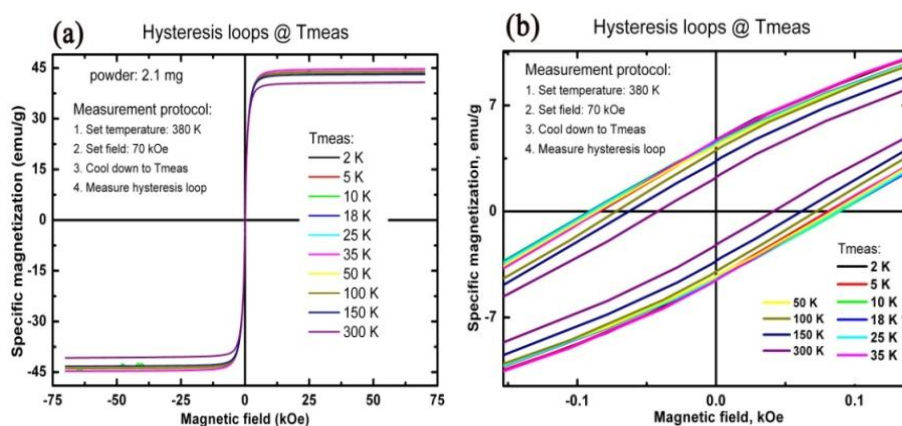
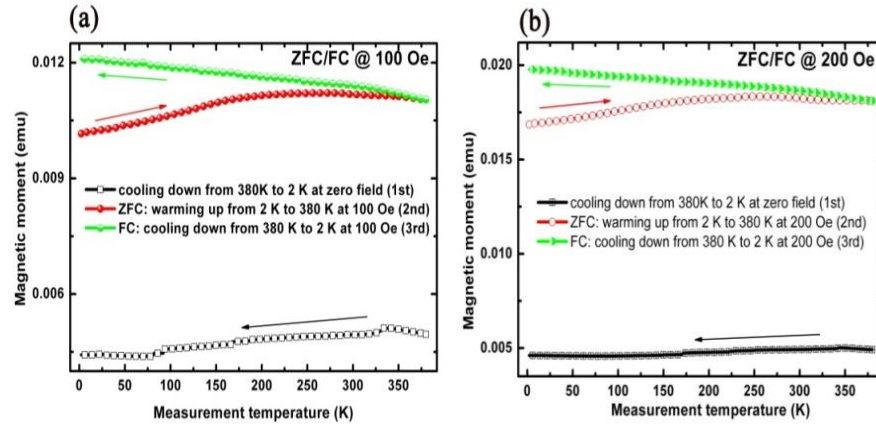


Figure 3.8: (a) FC hysteresis loops of Ni P (b) enlarged view of hysteresis loops low field

All the hysteresis curves exhibit saturation. At room temperature, a saturation magnetisation of 44 emu/g is obtained, and it increases with the decrease of temperature. The reduction in magnetisation from the bulk value could be attributed to the nano size of the particles. This could be also due to the porous nature and the lattice relaxation, as explained in section 3.3. This temperature dependence of saturation magnetisation is as per Curie-Weiss law [1] of ferromagnetism. Coercivity at room temperature is 42 Oe which increases as the temperature is lowered and it goes up to 90 Oe for 2 K. For all the isotherms the hysteresis curves were seen to be symmetric with the magnetization axis. This indicates the nonexistence of any exchange bias and is a proof for the absence of oxide layer on nickel particles.

The ZFC and FC measurements are carried out on the Ni P at low applied fields. Figure 3.9 depicts the temperature dependent measurements at two different applied fields. The measurement is carried out as follows: the sample is cooled in zero applied fields to 2 K; the moments will be arranged at random. The moment at this cooling will be very small. At low temperatures, measuring field is applied and the moment is measured while warming the sample to 380 K. This gives the ZFC moment variation with respect to temperature. With the same measuring field applied, the sample is cooled to 2 K and the moment is measured while cooling, providing the FC magnetic moment.



**Figure 3.9: ZFC/FC moment variation at an applied field of (a) 100Oe and (b) 200Oe (arrow points the direction of measurement)**

When the sample is cooled from high temperature without any external field, the particles as well as the moments are randomly organized. Each particle is spontaneously magnetized and this gives an averaged moment which is very small. Now when the field is applied the moments try to align in the field and the component in the measurement direction contribute to the net measured moment. This increases with temperature as the thermal energy competes with anisotropy of the particle moment. In the FC measurement, the moments are aligned in the measuring field and hence are in preferred direction with respect to measurement direction at 380 K. When the temperature is lowered, the thermal fluctuation decreases and the moments have their component more aligned to field direction and hence a slight increase in the measured moment. The measurements were carried out for an applied field of 100 Oe and 200 Oe which exhibited a similar behaviour with doubling of net moment as the applied field is doubled. A broad distribution of blocking is exhibited for the sample which is expected for poly dispersed particles of obtained size and distribution.

The saturation moment with temperature,  $M_s(T)$  measurements were carried out at a high applied field of 70 kOe, a field at which saturation occurs. The  $M_s(T)$  curve is presented in figure 3.10.

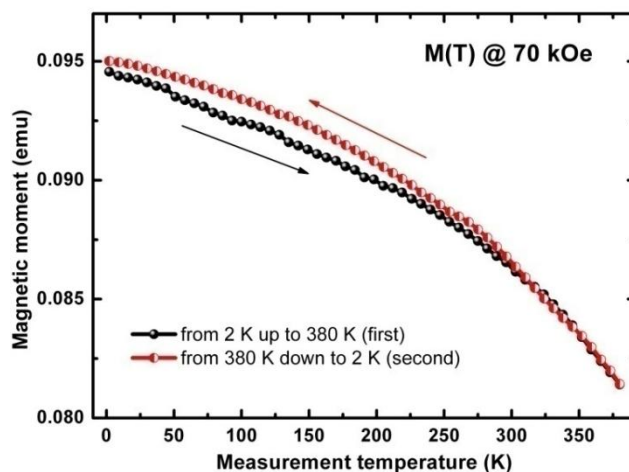


**Figure 3.10:  $M(T)$  measurements at 70kOe**

The moment variation with temperature under saturating field is typical for a ferromagnetic material. This follows the Curie-Weiss law and the moment's variation with temperature in ascending and descending order is similar.

### **3.4.2 Magnetisation measurements on Ni M**

Magnetic measurements on Ni M are carried out in SQUID magnetometer. The magnetisation isotherms are depicted in figure 3.11a. The measurement protocol is similar to the measurements performed on Ni P (section 3.4.1).

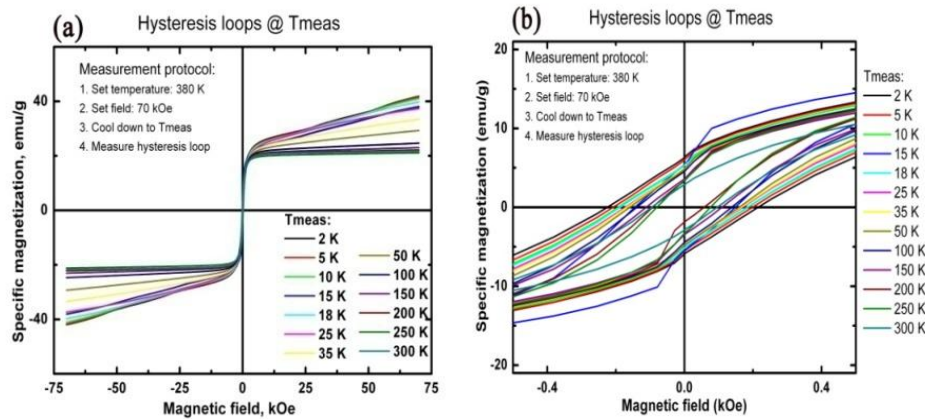


**Figure 3.11: (a) Hysteresis loops of Ni M, (b) enlarged view at low fields**

The specific magnetisation is reduced from that of Ni P, which can be explained due to the presence of oxide as is evident from structural analysis. The moment does not get saturated even at high applied fields indicating the presence of anisotropy or impurity phase which is antiferromagnetic or paramagnetic in nature. NiO is antiferromagnetic in nature and this could be the reason for the behaviour at saturating fields. The coercivity is found to be enhanced in the milled sample. This may arise because of the surface random anisotropy [12] induced due to reduction in size as well as the oxide present in it. The coercivity increases with decrease in temperature. The hysteresis loop shift amounts to 5 Oe at high temperatures which do not vary with temperature and no shift is visible at lower temperatures indicating the non-existence of exchange bias (EB) [35,36] irrespective of the fact that the sample contains NiO. This shows that the oxide particles are separated from the Ni particles and may not be in the form of a core shell structure.

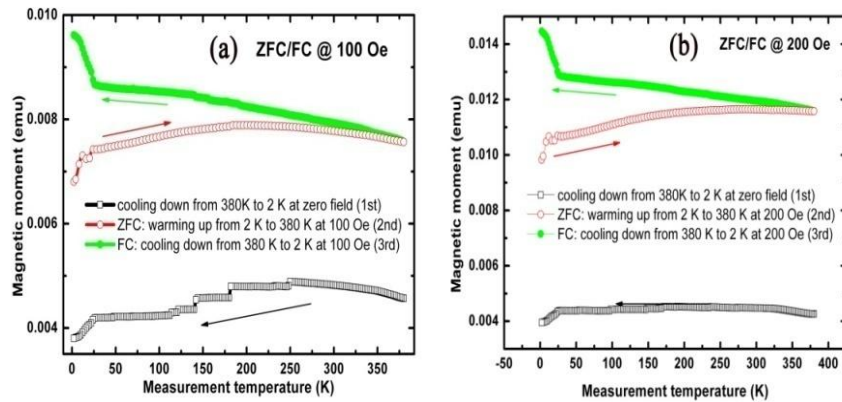


**Figure 3.12: ZFC/FC moment variation of Ni M at an applied field of (a) 100 Oe (b) 200 Oe**

Figure 3.12 shows the ZFC/ FC moment variation in Ni M at two different low applied magnetic fields. It could be seen that a broad distribution in blocking temperature is visible in either cases which is attributed to the interaction as well as the particle size distribution. At low temperature, for both applied fields a local minimum could be seen in the ZFC moment correlated with an increase in moment in the FC curves which may be considered as a kind of magnetic ordering. This could be from the magnetic moments of the smaller particles present in the sample.

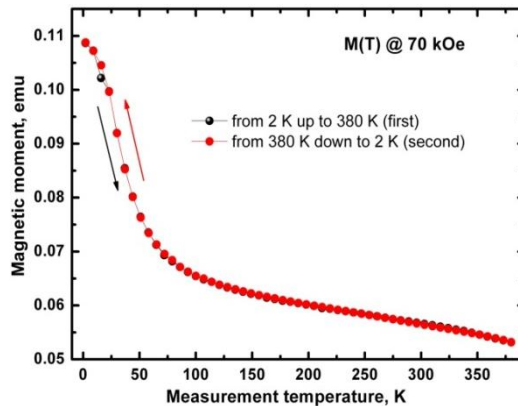


**Figure 3.13: M (T) curve at an applied field of 70kOe on Ni M**

Figure 3.13 depicts the variation of moment of Ni M sample at saturating fields. The moment deviates from ferromagnetic nature. For high temperatures ( $T > 100$  K) the moment variation follow ferromagnetic behaviour. As the temperature is lowered a deviation in slope with a sudden increase in moment is visible. This rapid increase in moment with decrease of temperature again evidences for a magnetic ordering occurring at low temperature as proposed from the ZFC/FC measurements. The proposed magnetic ordering occurs at low as well as saturating fields which need to be analysed further. ZFC/FC measurements with smaller applied fields of the order of 10 Oe could give better insight into the mechanism of ordering. NiO particles of 10 nm size could behave super antiferromagnetically (SAF) and thus contribute to the temperature dependent magnetic moment.

### 3.4.3 Magnetic studies on Ni F

The magnetisation isotherms (figure 3.14a) and FC/ ZFC (figure 3.15) measurements were carried out in a SQUID system. All the isotherms were measured without cooling the sample in high applied field. The coercivity extracted from the isotherms is presented in figure 3.14b.

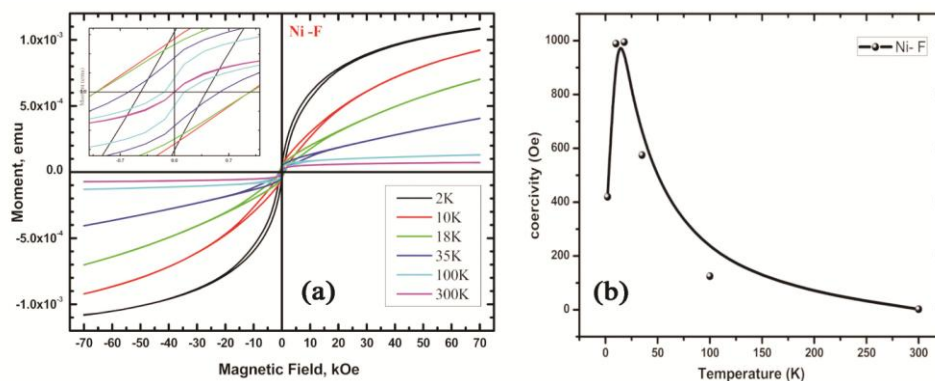


Figure 3.14: (a) Magnetisation curves of Ni F at different temperatures (b) Variation of coercivity with temperature in Ni F

The magnetic measurements on suspended particles (Ni F) were carried out after drying off the carrier liquid, kerosene.

The negligible coercivity (2 Oe) and remanence magnetization measured at room temperature indicates perfect superparamagnetic nature of the nickel nanoparticles. Table 3.1 consolidates the coercivity of all the three samples at different temperatures.

**Table 3.1 : Coercivity of Ni P, Ni M and Ni F at different temperatures (in Oe)**

Temperature	2K	5K	10K	18K	25K	35K	50K	100K	150K	300K
<b>Ni P (in Oe)</b>	86	82	91	89	88	83	84	71	61	42
<b>Ni M (in Oe)</b>	220	205	193	182	171	167	158	138	110	95
<b>Ni F (in Oe)</b>	420	-	989	995	-	575	-	125	-	2

The coercivity of Ni P remain more or less the same below 100 K. Only at high temperatures coercivity decreases and reaches 42 Oe at 300 K. Comparing the room temperature coercivity, Ni M has double the coercivity as Ni P, this could be arising from the size reduction and the surface anisotropy induced by the ball milling. It is to be noted that the particle size is reduced to half the value by ball milling. Moreover the oxide formed could induce an anisotropy as well. In the case of Ni F, its almost zero; showing that the particles are superparamagnetic as expected for a 5 nm Ni particle.

To analyse the magnetic transition with temperature, the zero field cooled (ZFC) and field cooled (FC) moment measurements were carried out from 2 K to 400 K at an applied field of 200 Oe (figure 3.15).

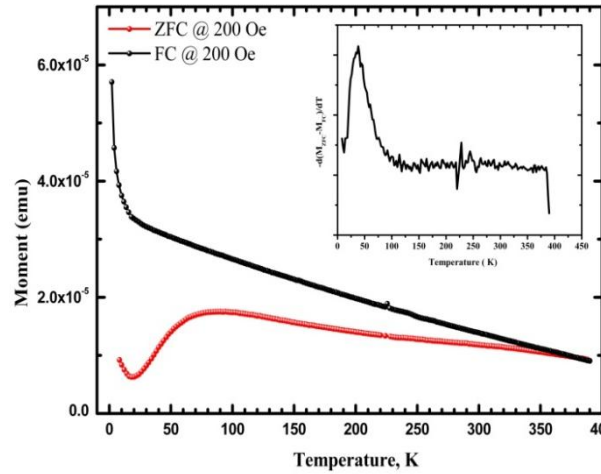


**Figure 3.15: ZFC-FC moment variation with temperature (Inset: The derivative plot showing blocking temperature)**

The derivative of difference in FC moment to ZFC moment w. r. t. the temperature, plotted in inset of figure 3.15 has a maximum at 38 K correspond to the average superparamagnetic blocking temperature of the metallic nanoparticles. The distribution of blocking temperature from the derivative curve is found to be narrow, which corresponds to minimised interparticle interaction and narrow particle size distribution. The anisotropy is calculated from the equation

$$K \cdot V = k_B T_B \cdot \ln(\tau_m / \tau_0) \quad (3.2)$$

Where  $\tau_0 \approx 10^{-10}$  s.  $\tau_m$  represents the measurement time typically 100 s for static measurements. For an average size of 4.5 nm the K value is calculated to be  $2.7 \times 10^6$  erg/cc. The enhanced anisotropy (bulk value  $0.5 \times 10^5$  erg/cc) could be due to the

surface contribution where the spins may be frustrated. This surface anisotropy accounts for the enhanced coercivity at lower temperature.

There is a minimum in the ZFC curve at still lower temperature of 18 K, below which both the FC and ZFC moments follow same kind of relaxation with lowering of temperature. This kind of variation has been reported for ultrafine cobalt nanoparticles [14] and is explained as contribution from surface spins which are in the oxide phase. The FC moment take a deviation in slope beyond this minimum at 18 K in the ZFC curve.

This variation of moment with temperature in the low applied field has a close correlation with the coercivity variation with temperature (figure 3.14b), where coercive field increases sharply from almost zero value at room temperature to nearly 1000 Oe at 18 K and then decreases with further decrease of temperature. As the temperature decreases, the nanoparticles go to the blocked state and the effect of surface spins becomes dominant [21]. There occurs a relaxation lag between the surface spins and the core causing increase of surface anisotropy which enhances the coercivity. At still lower temperatures, spins at the surfaces and the core perform cooperative switching following the applied field causing a decrease of coercivity and a sharp increase of magnetic moment [13,21]. The sharp variation in FC curves and local minimum in ZFC curves (figure 3.12) corresponding to Ni M sample can be considered here. Since the fluid particles contain narrow distribution of 5 nm sized particles which undergo magnetic ordering at low temperature, a sharp increase in moment and decrease of coercivity can be accounted. The Ni M contained broad distribution in size and hence the effect could be seen superimposed to a dominant response from larger particles.

The magnetization curves get saturated at temperatures down to 100 K (figure 3.14a). At lower temperatures they reveal combined ferro and paramagnetic like

behaviour with linear relation for M-H, at applied fields greater than 10 kOe. It is also visible that the moment increase with decrease in temperature and the variation is drastic for temperatures below 18 K : the moment is increased by almost an order. This is also characteristic of magnetic ordering which become prominent at low temperatures and could be from the surface spins of nanoparticles [22,23]. These prominent features are exhibited at very low temperatures well below the superparamagnetic blocking temperature, where the thermal energy is insufficient to fluctuate the net moment of the atomic cluster. The reduction in coercivity at 10 K and 2 K (figure 3.14) also points to the increased ordering at these temperatures. Similar properties are found in Co/CoO core shell systems [13,37] but with strong exchange bias. But there has been no confirmation whether the uncompensated spins originate at the AFM surface, or the interface or the metallic surface or the shell itself contributes to paramagnetic moment. Since the oxide shell could not be detected over Ni particles from HRTEM measurements, the contribution from the AFM shell can be considered negligible. The drastic increase in magnetic moment at high applied field below 100 K which go on increasing as the temperature is lowered, further conclude the magnetic ordering taking place in these nanoparticles.

### **3.5 Conclusion**

Sol-gel auto combustion is found to be a preferred technique for the synthesis of phase pure metal nanoparticles and these particles could be finely divided (reduction in particle size) further by ball milling. The structural and magnetic characterisation of the as prepared nickel shows that they are phase pure without any oxide impurity even though the metal nanoparticles are highly susceptible to oxidation. The high energy imparted to the nanoparticles during ball milling results in reduction of particle size with a little evolution of oxidation. An *in situ* surface passivation with surfactant during ball milling can help to get oxide free

nanoparticles. Ball milling causes increase in local temperature, causing the peptisation of surfactant to the particle and hence this could give protection from being oxidised when size is reduced. The surfacted nanoparticles are suspended in kerosene and stable metallic nanofluid is realised by this two step synthetic route. The particles with size around 5 nm are suspended in kerosene while the heavier particles settle owing to the stability criteria. This method could be generalised to synthesize suspensions of any metal.

The reduced size of the suspended nickel nanoparticles increases the relative amount of surface atoms. The magnetic properties get prominent contribution from the surface spins as well. The surface spins in Ni F nanoparticles causes modified magnetic properties which become highly temperature dependent. The large increase in coercivity with decrease of temperature is attributed to the surface-spin disorder combined with the blocking of fine metallic particles. To elucidate the mechanism of low temperature magnetic ordering occurring at low and saturating fields as observed from ZFC measurements and hysteresis curves require further studies. These oxide free stable nano suspensions can find immense applications in various fields of engineering and technology like heat transfer fluids, removal of large oil spills and in mines and space ships.

**References**

1. B. D Cullity and C. D. Graham, Introduction to magnetic materials, Second edition, Pg 127, John Wiley& Sons, 2009.
2. T. N. Narayanan, A. P. Reena Mary, P. K Anas Swalih, D. Sakthi Kumar, D.Makarov, M. Albrecht, J. Puthumana, A. Anas and M. R. Anantharaman *J. Nanosci. Nanotechnol.* doi:10.1166/jnn.2010.3578
3. X. Batlle, and A. Labarta *J. Phys. D: Appl. Phys.* 2002, 35, R15–R42.
4. V. Sunny T. N. Narayanan, U. S Sajeev. P. A Joy, D. S. Kumar, Y. Yoshida and M. R. Anantharaman *Nanotechnology.* 2006, 17; 4765.
5. V. F Puentes, K. M Krishnan and P. Alivisatos, *Appl. Phys. Lett.* 2001, 78, 15, 2187-2189.
6. V. Sunny, D. Sakthi Kumar, Yasuhiko Yoshida, M. Makarewicz, W. Tabiś and M.R. Anantharaman *Carbon* 2011 48 5 1643-1651
7. J.Fernández C. de. *Phys. Rev. B* **2005**; 72; 054438
8. M. Jagodić, Z. Jagličić, A. Jelen, J. B. Lee, Y-M Kim, Kim Hae J, Dolinšek J.; *Phys. Rev. B.*; 2005,72, 064404.
9. De Jesús, Juan Carlos. González, Ismael. García, Miguel. and Urbina, Caribay.; *J. Vac. Sci. Technol. A*; 2008; 26 (4), 913-918.
10. A. Henglein, *Chem Rev.* **1989**, 89 1869
11. T.Yonezawa and N. Toshima, *J Chem. Soci. Faraday Trans.* **91** 4111-30 (1995)
12. Löffler, Jörg F. Meier, Jürg P. Doudin, Bernard and Ansermet, Jean-Philippe. Wagner, Werner. *Phys.Rev. B.* 1998; 57; 2915-25.
13. D. Srikala, V. N. Singh, A. Banerjee, B. R Mehta, and S. Patnaik, *J. Phys. Chem. C*, 2008, 112 (36), 13882–13885.
14. Johnston-Peck, Aaron. C. Wang, Junwei and Tracy Joseph. B. *ACS NANO*, 2009, 3(5), 1077-1084,

15. Dong-Hwang Chen and Szu-Han Wu , *Chem. Mater.* 2000 12 1354-60.
16. Y.Sahoo, Y.He, M.T.Swihart, S.Wang, H.Luo, E.P.Furlani, and P.N.Prasad  
*J.Appl.Phys.* 98 054308.
17. F. A. Reuse and S. N. Khanna Geometry, 1995 *Chem. Phys. Lett.* 234 77-81
18. S. E. Apsel, J. W. Emmert, J. Deng, and L. A. 1996 *Phys. Rev. Lett* 76 1441.
19. Lo, Chih-Hung.; Tsung, Tsing-Tshih and Chen, Liang-Chia.;*JSME International Journal series B*, 2005; 48 ( 4); 750-755.
20. Hou, Yanglong.; and Gao, Song.; *J. Mater. Chem.* 2003, 13, 1510 – 1512.
21. Chen, Yuanzhi.; Peng, Dong-Liang.; Lin, Dongxing.; and Luo, Xiaohua.;  
*Nanotechnology*, 2007, 18, 505703.
22. Y. Hou, H. Kondoh T. Ohta and S. Gao , *Appl. Surf Sci.* 2005 241 218-222
23. Dong-Hwang Chen and Szu-Han Wu , *Chem. Mater.* 2000 12 1354-60.
24. Kyeong Youl Jung, Jong Ho Lee, Hye Young Koo, Yun Chan Kang and Seung Bin Park, *Materials Science and Engineering B* 2007 137 10–19.
25. Bin Xia, I. Wuled Lenggoro, and Kikuo Okuyamav , *J. Am. Ceram. Soc.* 200184 [7] 1425–32.
26. V. Singh, M.S.Seehra, J.Bonevich, *J.Appl.Phys.* 2008 103 07D524.
27. F. C. Fonseca, G. F. Goya, R. F. Jardim R. Muccillo, N. L. V. Carren˜o, E. Longo, and E. R. Leite , *Phys. Rev. B* 2002 **66** 104406.
28. Peng Li, Jingyue Liu, Nabin Nag, and Peter A. , *J. Phys. Chem. B* 2005 109 13883-13890.
29. Yuri Koltypin, Asuncion Fernandez, T. Cristina Rojas, Juan Campora,Pilar Palma, Ruslan Prozorov, and Aharon Gedanken , *Chem. Mater.* 1999 **11** 1331-1335.
30. R.E. Rosensweig, *Ferrohydrodynamics*, Cambridge University Press, 1985.

### Chapter 3

---

31. K. T. Wu, Y. D. Yao, C. R. C. Wang, P. F. Chen, and E. T. Yeh , *J. Appl. Phys.* 1999 85 5959.
32. Y. Bao, A. B. Pakhomov, and Kannan M. Krishnan , *J. Appl. Phys.* 2006 99, 08H107.
33. Muhammad Abdul Jamal E.; Joy P.A.; Kurian Philip.; and Anantharaman M.R.; *Mater. Chem. Phys.* 2010, 121(1-2), 154-60.
34. Mironova-Ulmane N.; Kuzmin A.; Steins I.; Grabis J.; Sildos I.; and Pärsl M.; *J. Phys.: Conf. Ser.* 2007, 93, 012039 (1-5).
35. M. Respaud, J. M. Broto, H. Rakoto, A. R. Fert L. Thoma, B. Barbara M. Verelst, E. Snoeck, P. Lecante, A. Mosset J. Osuna, T. Ould Ely, C. Amiens, and B. Chaudret , *Phys. Rev. B* 1998 57 2925–2935.
36. Set T.; Akinaga H.; Koga K.; Orii T.; and Hirasawa M.; *J.Phys. Chem. B. Lett*, 2005, 109, 13403-405.
37. Cheng Guangjun.; Dennis Cindi L.; Shull Robert D.; and Hight Walker A. R.; *Langmuir* 2007 23 11740-46.

## *Chapter 4*

### **Ferrite based aqueous and hydrocarbon Ferrofluids : A case study on Surfactant mediated inter-particle interactions and substitution effect on the magnetic properties**

Ferrofluids based on spinel ferrites are investigated owing to a multitude of applications in engineering and biomedical fields. The nature of the divalent ions and their occupancy decides the magnetic properties of spinel ferrites. The nanoparticles of these ferrites and their suspensions in various liquids are of great fundamental interest. Fluids of manganese zinc ferrites of 5 nm sized particles both in kerosene and water were synthesized by coprecipitation followed by suspending in respective liquids. The structural characterization was carried out by X-ray diffraction and electron microscopy. The magnetic properties are studied by employing SQUID magnetometer. The temperature dependent static measurements and analysis reveal the interparticle interaction effects on the overall magnetic behavior of nanoparticles. Hydrocarbon based fluids of iron oxide and cobalt substituted iron oxide with the chemical formula  $\text{Co}_x\text{Fe}_{1-x}\text{O}_4$  where  $x$  varies as 0, 0.2, 0.4 are realised by wet chemical methods. The cobalt substitution enhances the magnetic anisotropy. The temperature dependent magnetic measurements on these substituted ferrites show blocking near room temperature due to the surface coating of long chain oleic acid.

#### **4.1 Introduction**

Spinel Ferrites are hotly pursued materials in the magnetic industry. They being soft ferrites with high permeability, tunable electrical resistivity and low loss, find applications in high frequency communication devices, in electromagnetic shields, transformer cores and inductors [1-4]. The relative percentage of divalent and trivalent anions and their distribution in tetrahedral coordinated lattice sites (A sites) and octahedral coordinated sites (B sites) decide the electrical and magnetic properties to a great extent [1,3]. Nanocrystalline ferrites are important in applications such as particulate recording media, digital data storage, high quality filters, antennae, read heads, and in biomedical fields [1,5,6]. The moment of the divalent anion (M) in the formula  $(M_{1-x}Fe_x)[M_xFe_{2-x}]O_4$  and their preferred occupancy in tetrahedral or octahedral site (x being the degree of inversion) decides the overall magnetisation of ferrites as per Neel's two sub lattice model [7]. The occupancy of the cations in a definite lattice site is decided by their ionic radii and depends on the synthesis techniques as well as on the crystallization conditions [5,8,9]. Moreover the multiple oxidation states of anions such as  $Mn^{2+}/Mn^{3+}$  and  $Co^{2+}/Co^{3+}$  and their redistribution owing to the variation in synthesis techniques modifies the lattice parameters.

Bulk ferrites are well ordered with either normal spinel structure or inverse spinel with proper degree of inversion. When going down to nanosize, ferrites are partially inverse, where the nature of crystallization decides the extent of inversion. This results in the modified occupancy of the  $Fe^{3+}$  in lattice sites. Some of the divalent anion may occupy altered sites and they may get oxidised to 3+ state. So to balance the charge some of the  $Fe^{3+}$  ions transform to 2+ state in the favourable chemical environments and all these decides the total magnetic and structural properties.

Manganese zinc ferrites with high electrical resistivity have been applied in high frequency devices especially in radar absorbers [10], heat transfer nanofluids

[11] and biomedicine [12]. Manganese ferrite is a mixed ferrite in bulk with 20% of the divalent ion occupying the octahedral sites [1]. When going through the nano regime, inversion up to 67% is reported [13-14]. Zinc ions ( $Zn^{2+}$ ) being spherical, (ionic radii smaller) when substituted for manganese is expected to go to tetrahedral sites. The magnetic permeability increases and the  $T_c$  decreases with zinc substitution.  $T_c$  depends on the relative strength of AA, AB and BB interactions. When nonmagnetic ions are introduced into the A site, the AA interaction become very weak and this progressively decreases the transition temperature [15]. In colloidal sized Mn-Zn ferrites [16] the size effects and inter-particle interactions play a leading role in deciding the overall magnetic behaviour. The zinc ion occupying octahedral sites or the manganese with mixed valency and the degree of inversion can contribute to the modified magnetic and structural properties. This kind of cation redistribution is found in manganese zinc ferrites prepared by pulsed laser deposition and co-precipitation methods [13, 17]. The cation redistribution will modify the structural, magnetic and electrical properties to a great extent in the case of mixed ferrites like manganese zinc ferrites. Co-precipitation is an easy method to prepare nanoparticles especially for synthesizing colloids. The particle size of the manganese ferrite is found to decrease with zinc substitution [18]. The increase in the zinc substitution causes an increase in reaction rate and hence the lowering of the particles sizes. The saturation magnetization slightly increases up to about 40% Zn substitution and then it decreases further since more and more diamagnetic ion is added.

Ferrofluids based on the manganese zinc ferrites assume importance because they are highly sought after for heat transfer applications [19]. The thermal conductivity varies with applied magnetic field and this is another added advantage. They could be better candidates for heat transfer fluids in high power electric transformers and motors. In a non uniform field, the magnetic constituents could

present magneto-convective heat transfer in addition to the conventional convection. Fluids with large pyromagnetic coefficient could be good candidates for thermo magnetic transfer. Ferrites with specific properties like low Curie temperature, high saturation magnetization, low viscosity and high specific heat are good candidates as heat transfer fluids and manganese zinc ferrites could be a near perfect system. The adiabatic magnetization causes considerable change in temperature close to Curie temperature [20]. The magnetic properties of Manganese zinc ferrites can be tuned to get the  $T_c$  close to the operating temperature, provided the boiling point of the carrier is above it. These fluids could also present other interesting mechanisms including Brownian relaxation and temperature dependent magnetization reversal depending on the surfactants and carrier liquid that result in modified magnetic properties. They also exhibit surface magnetic anisotropy effects originating from the surface of finite sized particles [21] together with the inter-particle interactions and cation redistribution. The synthesis routes decide the cationic occupancy in lattice sites and oxidation states of anions in MnZn ferrites [22-24].

The composition of the manganese zinc ferrite series for which maximum magnetization obtained by using the preparation methodology chosen, is  $Mn_{0.6}Zn_{0.4}Fe_2O_4$  (from previous studies in the same group). The particle size for this stoichiometry was found to be optimum for suspending in water as well as kerosene. Nanoparticles of this particular composition were prepared and dispersed in both hydrocarbon and aqueous bases. Since in either case the surfactant chosen is different and hence the inter-particle separation. This leads to varied inter-particle interactions and hence modified magnetic properties.

#### **4.2 Synthesis of Nanofluids**

The synthesis is performed by chemical co-precipitation method. Solution of anhydrous 13.32 millimolar (mM) ferric chloride ( $FeCl_3$ ), 4 mM manganese chloride

tetra hydrate ( $\text{MnCl}_2 \cdot 4\text{H}_2\text{O}$ ) and 2.66 mM zinc chloride ( $\text{ZnCl}_2$ ) are prepared in 40 ml water to obtain a stoichiometry of 2: 0.6:0.4. This solution is made to react with 1000 ml of 1 M boiling NaOH solution in water. This reaction mixture is stirred for five minutes using a magnetic stirrer. The formed brown coloured precipitate is filtered from the supernatant solution to remove the unreacted radicals and water soluble byproducts. 50 ml of distilled water and 2 ml oleic acid are added to the mixture and stirred for another 90 minutes at 40°C. Then the resultant precipitate is allowed to cool while stirring and then few drops of con. HCl are added to reduce the pH of the mixture below 7. The precipitate coated with surfactant oleic acid is washed several times with water and dried well with acetone and dispersed in kerosene by ultrasound agitation. The fluid obtained is named as MZFK.

The water based fluid is prepared from the precipitate obtained after supersaturating with NaOH and stirring for two minutes. The precipitate is magnetically decanted and to this 50 ml of distilled water and 2 g citric acid in 5 ml water is added. The temperature is raised to 90°C and stirred for 60 minutes. The mixture is cooled and kept under a strong electromagnet to remove the supernatant solution. It is then washed with water to remove excess of citric acid. At a pH of 7, the precipitate gets suspended in water and is labeled as MZFW.

It has been observed that the rate of addition of reactants and the reaction temperature during the whole reaction process are highly crucial in the formation of magnetic phase. The fluids prepared are highly stable against sedimentation and possess good shelf life.

#### **4.3 Structural characterization**

The structural characterization by X-ray diffraction (XRD) shows (figure 4.1) that the particles are crystallized in the fcc spinel structure. All the major diffraction peaks are identified (ICDD: 74-2401).

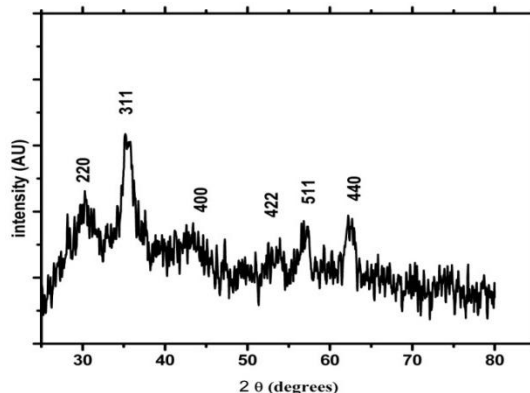


**Figure 4.1: X-ray diffraction pattern of MZFW**

The peak broadening clearly demonstrates the nanocrystalline nature of the ferrite. The crystallite size calculated by employing the Debye Scherrer's formula [section 3.3] is found to be 6.3 nm. Transmission electron microscopy (TEM) studies conducted on the samples indicate that the particle sizes match with x ray diffraction measurements and distribution of particle size is uniform. The samples for TEM are prepared by drying off the base liquids for both the samples. Figures 4.2a and b depicts the TEM images of MZFK and figure 4.2c is the particle size distribution obtained from the images. The mean size is obtained as 4.5 nm with standard deviation of 0.66 nm (figures 4.2c). Figure 4.3a shows the TEM image of MZFW and figure 4.3b, the size distribution with a mean size of 5.5 nm and standard deviation of 0.6 nm. It could be seen that the particles are uniformly distributed in size in both cases. A slight increase in size for water dispersed fluid particles is attributed to the digestion conditions. The MZFW is heated at 90°C and allowed to crystallize after the citric acid is added. While in MZFK, the sample is heated at lower temperature and the growth is more inhibited.

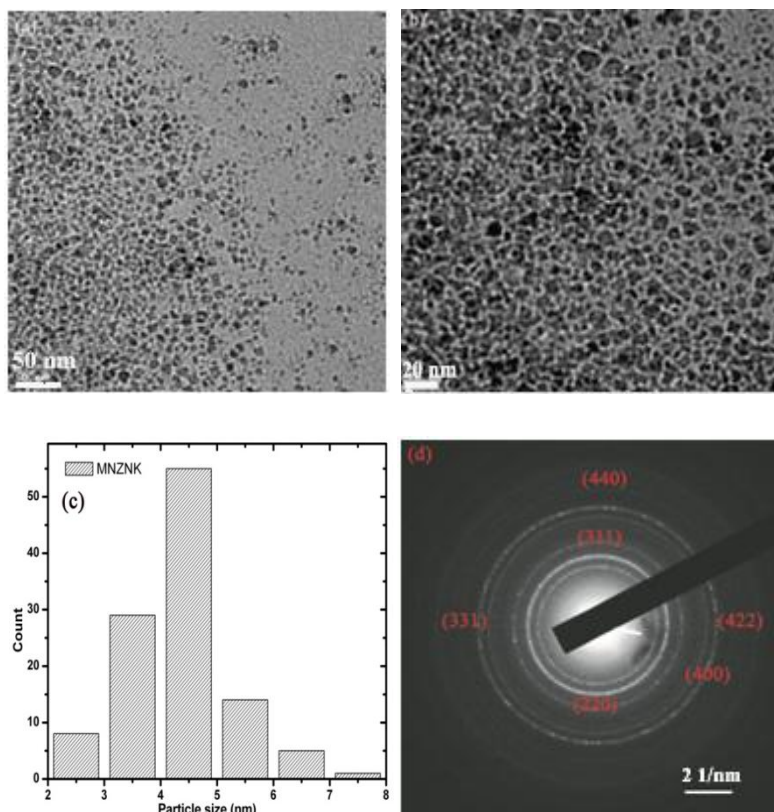


**Figure 4.2: (a)& (b)TEM images (c) Particle size distribution (d) SAED pattern of MZFK**

A close examination of figure 4.2b reveals the formation of tiny clusters consisting of 6 to 8 particles and the clusters are well separated from one another. This is reported for nanoparticles passivated with steric surfactants [25] which is due to interparticle interactions. Nevertheless each nanoparticle within the cluster is separately visible in TEM, since the particles are coated with oleic acid which separates them.

The selected area electron diffraction (SAED) pattern of the MZFK is shown in figure 4.2d. The diffused rings indicate the randomly oriented single crystalline particles in the sample. The major crystallographic planes (311), (331), (220), (400),

(422) and (440) of fcc spinel structure of  $\text{Mn}_{0.6}\text{Zn}_{0.4}\text{Fe}_2\text{O}_4$  are identified (ICDD No.74-2401).

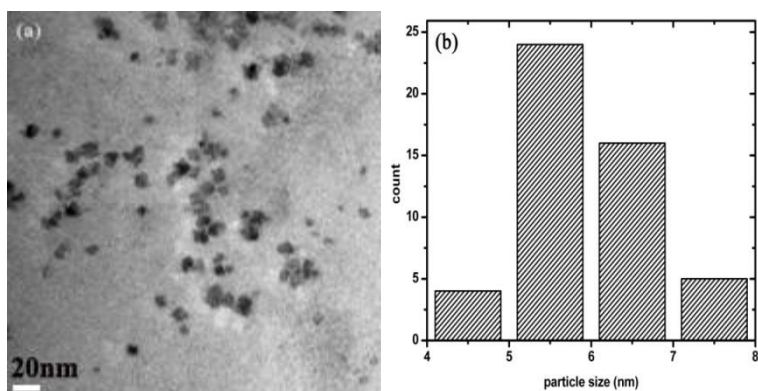
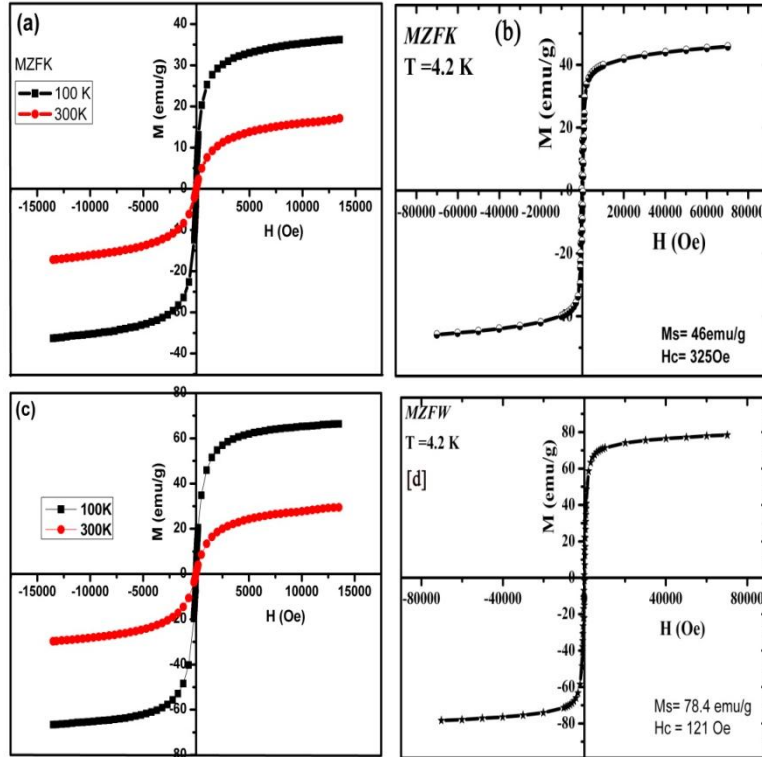


**Figure 4.3: (a) TEM image of MZFW (b) particle size distribution**

The TEM image of MZFW shows well distributed particles and no pattern formation is visible as in oleic acid coated MZFK (figure 4.2b) sample.

#### 4.4 Magnetic hysteresis measurements

Magnetic measurements were carried out in both vibrating sample magnetometer (VSM) and superconducting quantum interference device (SQUID) VSM. Figure 4.4 depicts the magnetisation loops of MZFK and MZFW measured at different temperatures. The moment increases with decrease in temperature as expected. The moment is not saturated even at high applied magnetic field, owing to the surface effects and superparamagnetic nature exhibited by the nanoferrites [26]. The magnetic order at the surface gets deformed from the bulk moment and when the surface become prominent, these effects are reflected in the net magnetic behaviour.



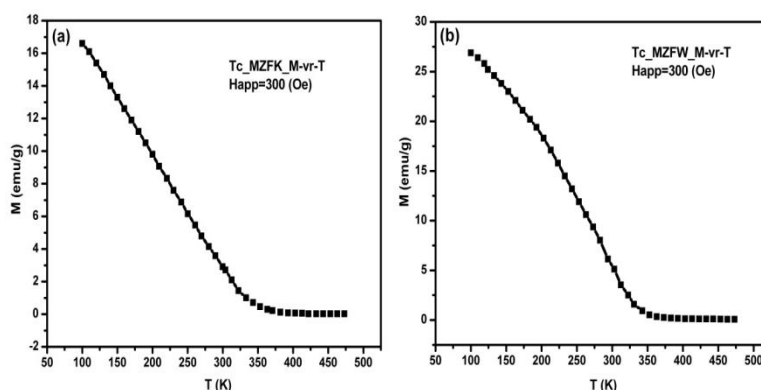
**Figure 4.4:** (a) M-H loop (VSM) measurements on MZFK at 300 K and 100K  
 (b) M(H) graphs (SQUID VSM) at 4.2K on MZFK (c) M-H loop (VSM) at 300 K and at 100K on MZFW (d) M (H) graphs (SQUID VSM) at 4.2K on MZFW

Table 4.1 consolidates the saturation magnetisation of MZFK and MZFW at different temperatures. The surface spins in ferrites are reported to form a dead layer that decrease the net magnetisation of the material from the bulk. The saturation magnetisation for both the samples decreases with increase of temperature, as expected by Curie-Weiss law, while at all temperatures MZFK present a lower specific magnetisation than MZFW. This is because oleic acid (with a molecular weight 282g) is a larger surfactant than citric acid (molecular weight 192 g); hence the weight fraction of nanoparticles is smaller in MZFK and thus a smaller value of

saturation magnetisation for particles with comparable sizes in both the samples. The magnetisation loop at room temperature presents negligible remenance and hysteresis showing the superparamagnetic nature of both samples as expected for a single domain particle with size of 5-6 nm.

**Table 4.1: comparison of magnetisation at varoius temperatures**

Sample	300K	100K	4.2K
<b>MZFK</b>	20 emu/g	36 emu/g	46 emu/g
<b>MZFW</b>	30 emu/g	66 emu/g	78.4 emu/g



**Figure 4.5: Moment variation with temperature showing  $T_c$   
(a) MZFK and (b) MZFW**

Figure 4.5 shows the temperature dependent moment variation at an applied field of 300Oe. The measurement has been recorded from liquid nitrogen temperature to 200°C, showing that at the Curie temperature the moment reduces to zero. The  $T_C$  value obtained is 393 K (120°C) which is lowered than that for the bulk value. A detailed study regarding Curie temperature with respect to the zinc substitution shows

that  $T_c$  increases upto 30% zinc ions and then it decreases [27]. The variation in  $T_c$  could have the origin in the cationic redistribution. Further studies are required to rule out other possibilities. The variation seen in figure 4.5a is of typically paramagnetic in nature with a linear function of temperature following the Curie's law. This indicates the Langevin type behaviour for non-interacting superparamagnetic particles. The particles in MZFK are well separated from one another by surfactant oleic acid, which is covalently bound to the particle surface. Whereas, the citric acid (CA) coated particles (figure 4.5b) shows slight deviation from the linear behaviour. This indicates the presence of inter-particle interaction. Since CA provides ionic/electrostatic stabilisation in water besides the nominal steric repulsion, when water is dried off, the electrostatic repulsion decreases and this causes the interaction among particles in MZFW.

#### **4.5 FC/ZFC measurements**

The field cooled (FC) and zero field cooled (ZFC) magnetic moment variation as a function of temperature is measured in a SQUID at two different applied fields. The results are presented in figures 4.6 and 4.7. In ZFC measurement, the sample is cooled down to 5 K from room temperature with zero applied field. The particles get cooled with their moments in random directions. An external magnetic field corresponding to the initial magnetisation is applied and moment of the sample is measured by increasing the temperature. In FC measurement, the sample is cooled in an applied field equal to the measurement field and the moment at different temperature is recorded. Both ZFC and FC measurement are carried out for two applied fields for both the samples, MZFK and MZFW. In the beginning of ZFC measurement, the moments are in random directions and the anisotropy of the particles try to align the moments in the random directions itself. The anisotropy energy makes the energy barrier, given by

$$E_{\text{anis}} = KV \quad (4.1)$$

where  $K$  is the anisotropy constant and  $V$  the particle volume. The particles are under an external field of strength  $H$  and hence have Zeeman energy

$$E_{\text{Zeeman}} = mH \quad (4.2)$$

where  $m$  is the moment of particle with  $m = M_s V$ .

The thermal energy acting on the particles is

$$E_{\text{therm}} = k_B T \quad (4.3)$$

at temperature  $T$ , where  $k_B$  is the Boltzmann constant. As the temperature is raised, the particles get disturbed and the Zeeman energy tries to align the moment in the field direction causing an increase in the susceptibility. The moments with a component in the measurement direction contribute to the net measured moment, and are kept at that condition by the anisotropy of the material. The particles are said to be in the blocked state along the easy axis. The moment increases with temperature and at a particular temperature the thermal energy equals the anisotropy energy and moment become maximum. This particular temperature is known as blocking temperature  $T_B$ . When the thermal energy become greater than the anisotropy energy, the moments are thermally randomised (moments are no more blocked) and the measured moment decreases monotonically with temperature. The FC moment increases with decrease in temperature along with the ZFC moment, since both the measurements are at same applied field. Near the maximum of the ZFC, the FC curve diverges and continue to increase.

The interparticle interactions modify the energy barriers and relaxation of the individual particle can no longer be considered. When the dipole-dipole interaction is considered, the classical superparamagnetism model need to be revisited. The  $T_B$  is

the temperature at which the relaxation time of the particles become equal to the measurement time. The relaxation time  $\tau$  is given by Neel-Brown expression

$$\tau = \tau_0 \exp(KV/k_B T) \quad (4.4)$$

where  $\tau_0$  amounts  $10^{-9}$  to  $10^{-12}$  s. Assuming the time window to be 100 s in static measurements, the deblocking and randomisation occurs when

$$KV = 25 k_B T \quad (4.5)$$

The point at which FC and ZFC curves bifurcate is the irreversibility temperature,  $T_{irr}$ , which is the highest blocking temperature which corresponds to the largest particles [28], when the particles are non interacting. Particles show hysteresis in blocked state below  $T_B$ , and above it, no hysteresis is measured. In the case of interacting systems, the energy barrier gets modified with the energy of interaction, where the particles are closer, the dipole-dipole strong interaction exists, and the energy could be calculated by mean field model as given below [1]. The energy possessed per particle of volume  $V$  in an external magnetic field become

$$E = V(K \sin^2 \theta + H M_s \cos \theta) \quad (4.6)$$

The energy barrier gets modified to

$$\Delta E = KV \left(1 - \frac{H M_s}{2K}\right)^2 \quad (4.7)$$

The blocking in static measurements is shifted to a lower temperature in applied field.

Figure 4.6a and 4.6b shows the FC-ZFC measurements at two different applied fields on MZFK. Both  $T_B$  and  $T_{irr}$  get shifted to low temperatures as the applied field is increased. Blocking is affected by Zeeman energy, reflected in the energy for the magnetisation reorientation.  $T_B$  is a function of the measuring field (inset of figure 6b). The ZFC moment increases, reaches a maximum at the blocking

temperature and then monotonically decreases in all the cases. This shows that the particles undergo magnetisation reversal more or less independently. The two temperatures,  $T_B$  and  $T_{irr}$  are closer with a separation of 23 K in both fields. The interaction among the particles are less, which is evident from the TEM images that the particles are uniformly distributed and are well separated. The clustering effects could be a reason for the increased effective size of the particles, which is reflected in this difference in  $T_B$  and irreversibility temperature. The FC curve is measured from room temperature down to 5 K. The moment increases with decrease of temperature since the thermal fluctuation is minimised as the temperature is lowered, deviates from ZFC moment at  $T_{irr}$  and continue to increase further. Below  $T_B$ , moment increases, but with a different slope. This may be due to the tiny cluster formation.

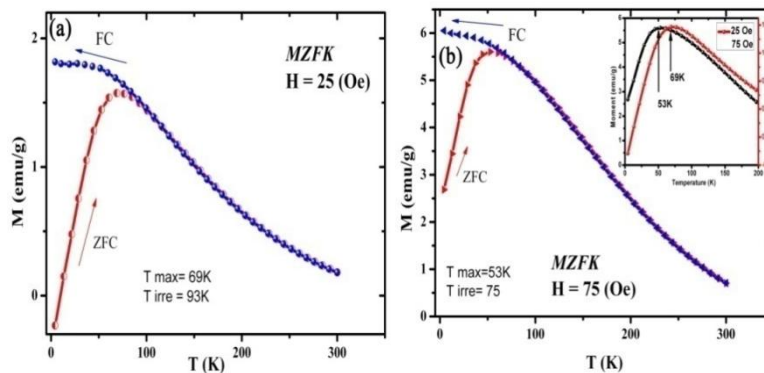


**Figure 4.6: ZFC-FC moment variation at applied fields (a) 25 Oe, (b) 75 Oe on MZFK**

In each cluster of few particles, the particles interact through surfaces, increase the energy barrier and hence are not free to rotate independently. This impedes otherwise free moments, to align in field and result in a gradual increase of magnetic moment with decrease of temperature below blocking. The narrow distribution of blocking temperatures (the  $T_B$  and  $T_{irr}$  are quite closer) indicate the uniform particle size and absence of strong interaction among the particles.

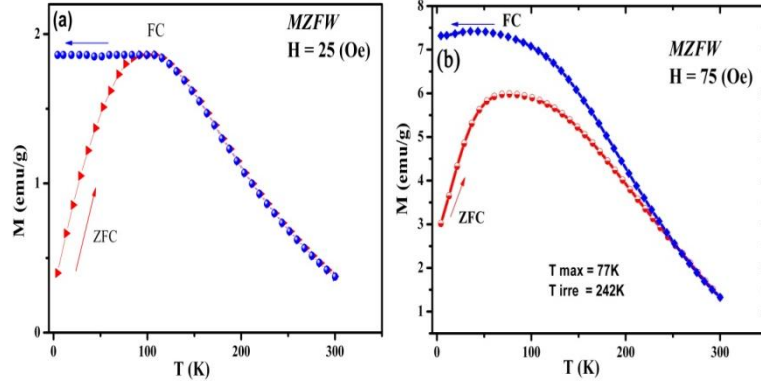


**Figure 4.7: ZFC-FC moment variation at applied fields (a) 25 Oe, (b) 75 Oe on MZFW**

Figure 4.7 depicts the ZFC-FC measurements on MZFW at two measuring fields. For low field, the blocking and irreversibility occurs at same temperature which is spread around 100 K at a measuring field of 25 Oe. The ZFC curve exhibit a broad maximum typical of a superparamagnetic but for interacting nanoparticles. Progressive deblocking of nanoparticles results in this broad blocking phenomena. At  $T > T_B$  both curves follow decrease of moment obeying a Curie-Weiss law. The FC moment for  $T < T_B$  remains constant, which could be explained as a result of inter-particle interaction which increases the anisotropy, making the moments pinned to one another and the thermal energy is too small to overcome the energy barriers and cause a magnetisation reversal. The anisotropy get modified with energy of interaction and the reversal or blocking can be expressed as

$$KV + E_{interaction} = 25 k_B T_B \quad (4.8)$$

The curves obtained at 75 Oe measuring field shows lowering of blocking temperature which is quite expected similar to the case of MZFK. However, the bifurcation takes place at a far higher temperature from  $T_B$ . This shows the presence of larger particles in the sample. The strength of interaction depends on the moment of the particles and the increased measuring field causes stronger interaction resulting

an increase in effective volume and hence the higher  $T_{irr}$ . The ZFC curve show a broader maximum and the magnetic relaxation for  $T > T_B$  slightly deviates from exact Curie-Weiss law indicating the existence of dipole-dipole interaction among the particles.

#### **4. 6 Cobalt substituted iron oxide ferrofluids ( $Co_x Fe_{(1-x)} Fe_2O_4$ )**

Magnetite ( $Fe_3O_4$ ) exists in fcc inverse spinel structure with tetrahedral voids occupying  $Fe^{3+}$  ions while octahedral sites are occupied by equal number of  $Fe^{2+}$  and  $Fe^{3+}$  ions. When the size is reduced to about 10 nm they may exist as maghemite ( $\gamma$ - $Fe_2O_3$ ), a magnetic phase of ferrite with modified oxidation states. Cobalt ions when substituted, prefer to occupy the octahedral (B) sites [1] and will modify the magnetic properties. Cobalt ions, with high magnetocrystalline anisotropy, when substituted for iron, enhances structural and magnetic anisotropy. This is attributed to the increase in both the exchange field due to neighboring spins and the effect of spin-orbit coupling [29]. The experimental magnetisation of cobalt ferrite deviate from the spin only moment due to the absence of the complete quenching of orbital moment. When cobalt is introduced into the spinel ferrite matrix, depending on the precipitation condition, they could also exist as  $Co^{3+}$  and also could occupy the tetrahedral site with unstable structures. This alters the expected magnetization value. However their existence in any site will increase the anisotropy [30] and will be reflected in the hysteresis of the resulting material. This increase in anisotropy will decrease the size limit of the particles to exhibit superparamagnetism. The method of preparation by co-precipitation may induce defects in the surfaces of the nanoparticles and may also result in non stoichiometric ferrites. Such defects lead to spin canting effects in magnetisation. It has been reported that in coated or surface modified particles the surface effects do not show altered magnetic properties and they are ideal templates to study the finite size effects.

Colloidal sized cobalt ferrites with high magnetocrystalline anisotropy are technologically explored for high density data storage, magneto caloric applications (MCE) and in biomedical applications. The study of dependence of cobalt ion concentration in the spinel lattice is of great fundamental interest with respect to their structural and magnetic properties.

#### **4.7 Synthesis of cobalt substituted iron oxide nanofluids**

Ferrofluids of magnetite and cobalt substituted iron oxide nanoparticles are prepared by chemical co-precipitation technique.  $\text{Co}_x\text{Fe}_{(1-x)}\text{Fe}_2\text{O}_4$  with x varying as 0, 0.2 and 0.4 are precipitated out from aqueous solution of cobalt sulphate ( $\text{CoSO}_4\cdot\text{H}_2\text{O}$ ), ferrous sulphate ( $\text{FeSO}_4\cdot 7\text{H}_2\text{O}$ ) and ferric chloride ( $\text{FeCl}_3$ ) in the appropriate stoichiometric molar ratio (x:(1-x):2), by controlled addition of aqueous ammonia (8%) upto a pH of 10.5. While in solution, these particles are peptized with oleic acid at 40°C. Water soluble by-products are removed by washing several times with de-ionised water. Moisture content of the obtained slurry is dried off with acetone and then dispersed in kerosene by ultrasound agitation. The samples are named as CF0(x=0), CF2 (x=0.2) and CF4 (x= 0.4).

#### **4.8 Structural characterization**

Figure 4.8 shows the XRD pattern of the samples. It is seen that the all the three diffraction patterns corresponds to fcc spinel structure, with the major diffraction planes. The XRD measurements are taken after drying off the kerosene from fluid. The peaks are found to be broadened due to the finite size of the particles. Applying Scherrer's formula, the particle size is evaluated to be around 8.5 nm.

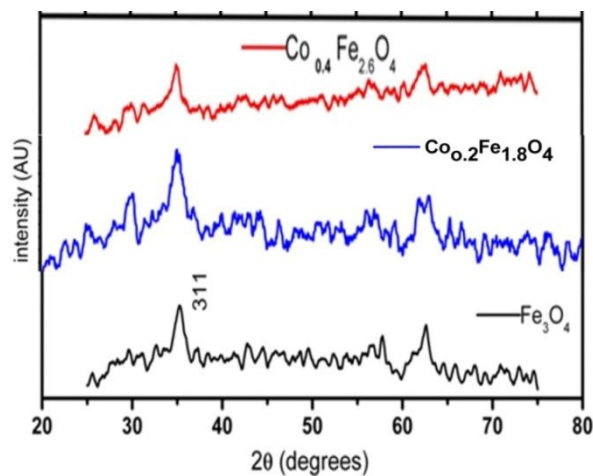


Figure 4.8 : XRD pattern of cobalt substituted magnetite

The peak broadening clearly shows that the particles are nanocrystalline and the noisy background originate from the surfactant (oleic acid) present in the sample.

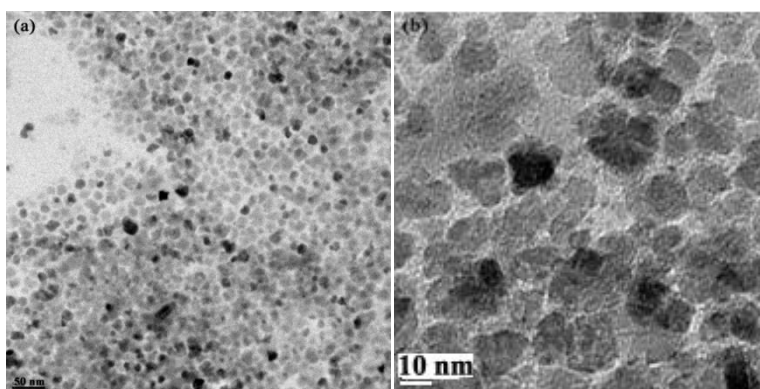
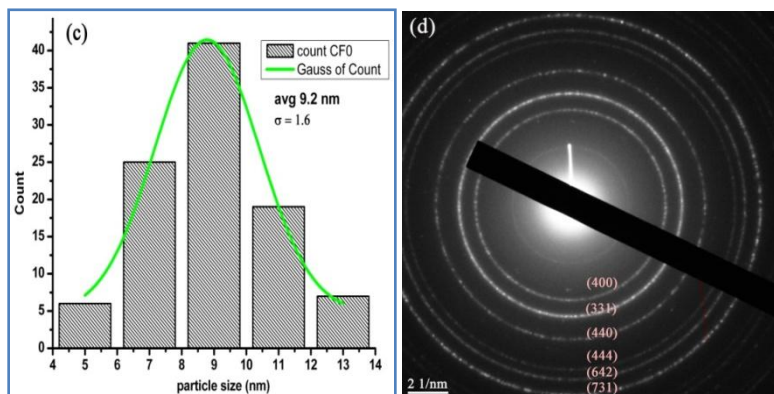


Figure 4.9: (a)& (b) TEM images of iron oxide nanoparticles



**Figure 4.9: (c) the particle size distribution (d) the SAED pattern**

Figure 4.9a and b depicts the TEM images of iron oxide nanoparticles, which shows uniformly distributed suspended particles. 4.9c depicts the size distribution obtained from TEM images which give a mean size of 9.2 nm and standard deviation of 1.6 nm. The SAED pattern (figure 4.9d) shows the diffused rings corresponding to the crystal planes of fcc spinel ferrites with a lattice constant of 0.859 nm.

Figure 4.10 depicts the TEM measurements on  $\text{Co}_{0.2}\text{Fe}_{2.8}\text{O}_4$ . The particles are uniformly distributed in size with an average size of 9.5 nm and SD of 1.12 nm. The SAED pattern have diffraction rings corresponding to spinel fcc with a lattice parameter of 0.819 nm. The lattice is contracted by the introduction of cobaltous ions in spinel lattice.

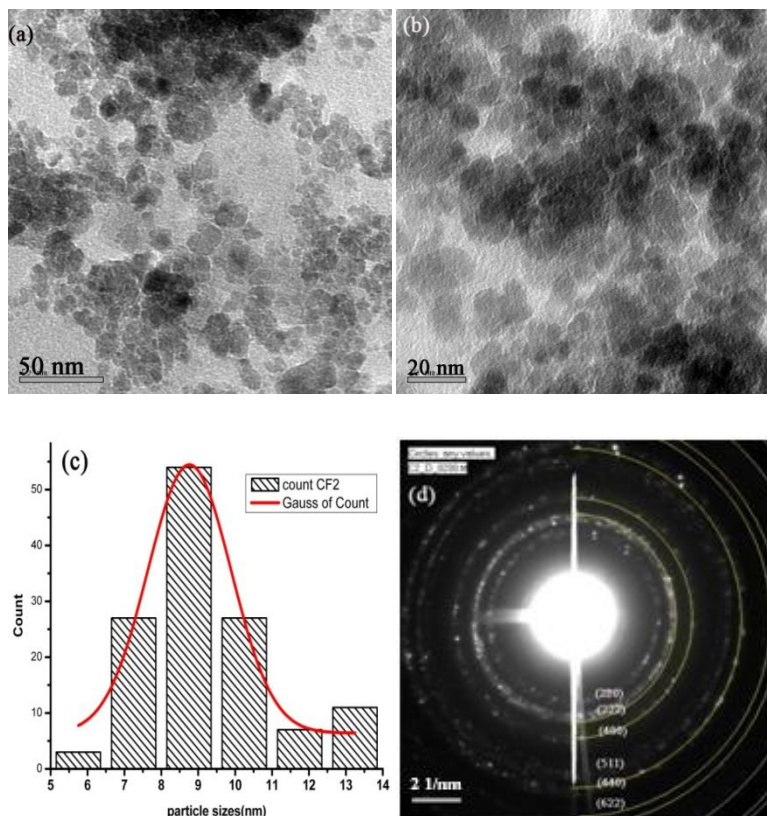


Figure 4.10: (a), (b) TEM images (c) the particle size distribution (d) the SAED pattern  $\text{Co}_{0.2}\text{Fe}_{2.8}\text{O}_4$

#### 4.9 Magnetic measurements

Magnetic hysteresis curves (figure 4.11) are measured in a SQUID VSM at 300 K and 10 K on all the three samples CF0, CF2 and CF4. The loop parameters are consolidated in table 4.2. The samples are prepared by drying off the kerosene followed by washing with acetone which might have removed the oleic acid coating from the particles. It could be seen that the coercivity at room temperature is more or less equal in all the three samples. At 10 K, the coercivity has enhanced as expected for single domain particles. For iron oxide the coercivity has increased to 104 Oe,

whereas for cobalt ion substituted ferrite coercivity get enhanced by two orders, and it increases with cobalt ion concentrations. This shows that the coercivity could be tuned to desired value by carefully selecting the substitution percentage of cobaltous ion. The saturation magnetisation is found to be less than the bulk values and could be due to the surface dead magnetic layer in nanosized oxides. This could also be related to the lattice expansion, and the resulting density variation, measured in the SAED. At 20% substitution, the moment has increased where as for higher substitution of 40% (CF4), saturation magnetisation get reduced. This kind of variation in magnetization saturation has been found in cobalt substituted iron oxide particles of size 4.3 nm [31]. The cobalt ions occupancy in tetrahedral sites and the oxidation states of Co and their relative distribution need to be further probed to find the real mechanism for this kind of variation of magnetic moment. The increase in coercivity shows that cobalt ions has been progressively introduced into the spinel lattice.

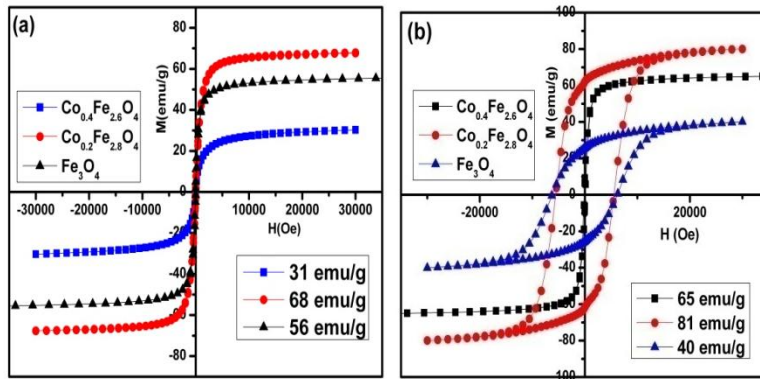


Figure 4.11: Hysteresis curves of  $\text{Co}_x\text{Fe}_{3-x}\text{O}_4$  at (a) 300 K and (b) 10 K

The hysteresis loop parameters are consolidated in table 4.2.

Table 4.2: Loop parameters from hysteresis curves

Sample	$M_s$	$H_c$ (RT)	$H_c$ (10K)
$Fe_3O_4$	56 emu/g	39 Oe	104 Oe
$Co_{0.2}Fe_{2.8}O_4$	68 emu/g	46 Oe	5550 Oe
$Co_{0.4}Fe_{2.6}O_4$	31 emu/g	32 Oe	6250 Oe

The ZFC-FC moment variation is depicted in figure 4.12 and 4.13. The ZFC curve of iron oxide (figure 4.12a) shows a broad maximum at 275 K. The flatness of FC moment indicates the strong interparticle interaction among the particles. For 20% Co (CF2) substituted particles, no blocking is visible from ZFC moment, and the initial slope is concave. The anisotropy increase in these particles make them intrinsically superparamagnetic below the size of 5 nm. Since oleic acid has been removed with acetone, the inter-particle interaction could also contribute to the ferromagnetic behaviour upto room temperature.

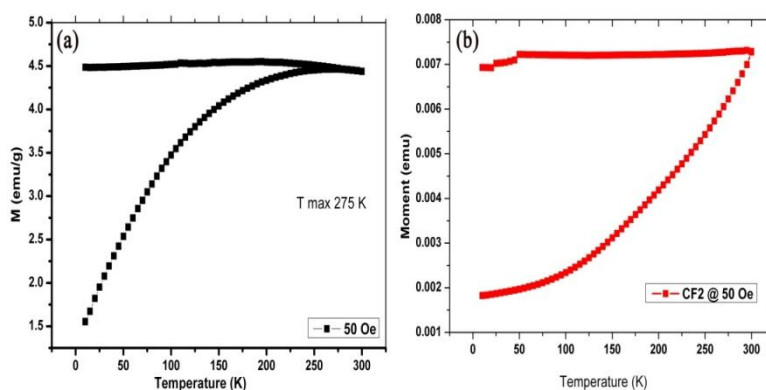
Figure 4.12: ZFC-FC curves of  $Co_xFe_{3-x}O_4$  for (a)  $x=0$ , (b)  $x=0.2$ 

Figure 4.13a-c shows the ZFC-FC moments for 40% cobalt substituted  $Fe_3O_4$  sample at three different applied fields (50, 200 and 1000 Oe). The initial variation of the

ZFC moment is similar to the CF2 sample, but shows blocking below room temperature. The enhancement in coercivity measured at 10 K indicates that the anisotropy has increased with cobalt addition. The blocking could be arising from the extrinsic superparamagnetism owing to the oleic acid coating which has remained even after washing with acetone. This could also explain the lowered saturation magnetisation value of CF4 (table 4.2).

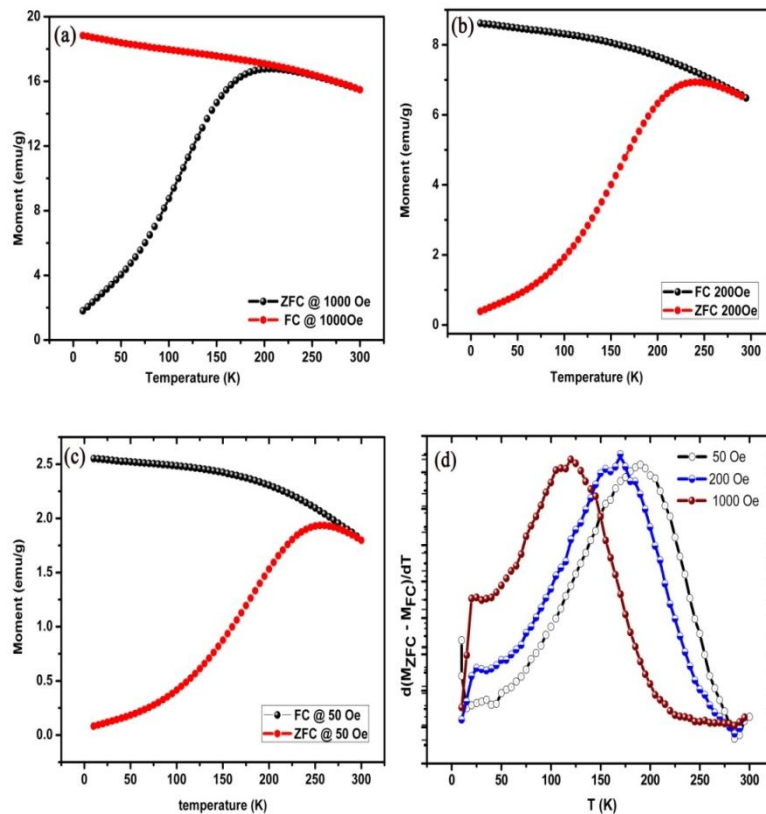


Figure 4.13: ZFC/FC curves of  $\text{Co}_x\text{Fe}_{3-x}\text{O}_4$  for  $x=0.4$  at an applied field of (a) 1000Oe, (b) 200 Oe, (c) 50Oe and (d) Differential plot for (a),(b) and (c)

The FC moments increases with decrease of temperature showing that the inter-particle interactions are weak. The blocking temperature progressively shift towards

the lower values as the applied field is increased as per equation 4.7. The first derivative of the difference in ZFC and FC moments with respect to temperature is plotted in figure 4.13d, for all the three applied fields. The maximum of the derivative plot corresponds to the average deblocking of magnetisation or moment reversal with thermal energy. The maximum shifts to lower temperature as field strength is raised. The presence of surfactant and the weakened interaction thereof, among the particles cause the blocking below room temperature of otherwise anisotropic CF4 particles.

#### **4.10 Conclusion**

Ferrofluids (both aqueous and hydrocarbon based) of spinel manganese zinc ferrite particles of size around 5 nm, in the composition  $Mn_{0.6}Zn_{0.4}Fe_2O_4$  is synthesized by supersaturating with sodium hydroxide at boiling temperature. Water based fluids are surfacted with citric acid, which provides electrostatic stabilization. The repulsion gets diminished when the carrier is dried off. The dipolar interaction is strong in the suspended particles. The oleic acid coating of nanoparticles provides separation between particles and hence the dipolar exchange is found to be lowered. The inter-particle interactions among superparamagnetic particles are explained based on temperature dependent static magnetic measurements.

Hydrocarbon based ferrofluids of spinel iron oxide and cobalt substituted iron oxide nanoparticles are synthesized using ammonium hydroxide to saturate. The coercivity is found to be increasing with cobalt content in the lattice. This shows that the anisotropic cation when introduced in the spinel lattice could enhance the coercivity which could be tuned by proper percentage of substitution. The saturation magnetisation is found to deviate from the expected stoichiometry and occupancy in tetrahedral or octahedral sites. The exact mechanism for the exhibited behaviour requires further studies such as low temperature Mossbauer measurements. The fluids

synthesized exhibited high shelf life and good stability against moderate applied magnetic field.

The cobalt substitution shifts the blocking temperature to higher value compared to the manganese zinc ferrite fluid particles and this could be efficient candidates for magneto caloric applications.

**References**

1. B. D Cullity and C. D. Graham, Introduction to magnetic materials, *Wiley publishing*, second edition
2. J. Smit and H.P.J. Wijn, Ferrites, *Phillips technical library, Eindhoven, The Netherlands* (1959)
3. S. Chikazumi, Physics of ferromagnetism, second edition, *Oxford Science publications* (1997)
4. JianLiang Xiea, Mangui Hana, Liang Chena, Renxiong Kuanga, and Longjiang Denga, *J. Magn. Magn. Mater.* **314** 37-42 (2007)
5. Chao Liu, Bingsuo Zou, Adam J. Rondinone, and Z. John Zhang , *J. Phys. Chem. B*, 104 (2000)
6. C. N. Chinnasamy A. Narayanasamy N. Ponpandian R. Justin Joseyphus B. Jeyadevan , K. Tohji and K. Chattopadhyay , *J. Magn. Magn. Mater.* **238**, 281-287 (2002)
7. Y. Yafet and C. Kittel, *Phys.Rev.* **87** 290- 294 (1952)
8. Feng Li, Junjie Liu, David G. Evans, and Xue Duan, *Chem. Mater.*, **16**, 1597-1602 (2004)
9. Camilla Nordhei, Astrid Lund Ramstad and David G. Nicholson , *Phys.Chem. Chem. Phys.* **10** 1053–1066 (2008)
10. Adriana M. Gama , Mirabel C. Rezende, and Christine C. Dantas *J.Magn.Magn. Mater.* **323**, 22 2782-85 (2011)
11. T. Upadhyay, R. V. Upadhyay, R. V. Mehta, V. K. Aswal and P. S. Goyal *Phys. Rev. B* **55** 5585-88 (1997)
12. Fujun Ma, Jian Lu , Zhiyong Wang, Jiayu Sun, Qiyong Gong, Bin Song, Hua Ai and Zhongwei Gu, *Int. J. Magnetic Resonance Imaging* **02**, 050-055 (2010)

13. J. Sakurai and T Shinjo , *J. Phys. Soc. Jpn* **23** 1426 (1967)
14. J. P. Chen, C. M. Sorensen, K. J. Klabunde, G. C. Hadjipanayis, E. Devlin and A. Kostikas , *Phys. Rev.B* **54** 9288-96(1996)
15. T. Upadhyay, R. V. Upadhyay, R. V. Mehta V. K. Aswal and P. S. Goyal *Phys.Rev. B* **55** 5585 -88 (1997)
16. R. Arulmurugan, G. Vaidyanathana, S. Sendhilnathan and B. Jeyadevan , *J.Magn.Magn. Mater.* **298** 83-94 (2006)
17. Chandana Rath, N. C. Mishra, S. Anand, R. P. Das, K. K. Sahu, Chandan Upadhyay and H. C. Verma, *Appl. Phys. Lett.* **76** 475-77 (2000)
18. E. Veena Gopalan, I.A. Al-Omari, K.A. Malini, P.A. Joy, D. Sakthi Kumar, Yasuhiko Yoshida and M.R. Anantharaman, *J. Magn. Magn. Mater* **321** 1092-1099 (2009)
19. B. Jeyadevan, C.N. Chinnasamy, K. Shinoda, K. Tohji, H. Oka, *J. Appl. Phys.* 93 (2003) 8450
20. E. Veena Gopalan, I. A. Al-Omari, D. Sakthi Kumar, Yasuhiko Yoshida, P. A. Joy and M R Anantharaman , *Applied Physics A: Materials Science & Processing* **99**, 497-503(2010)
21. P. Poddar, H. Srikanth, S.A. Morrison, E.E. Carpenter , *J. Magn. Magn. Mater* **288** 443–451(2005)
22. S. Calvin, E.E. Carpenter, B. Ravel, V.G. Harris, S.A. Morrison, *Phys. Rev. B* 66 (2002) 224405
23. S.A. Morrison, C.L. Cahill, E.E. Carpenter, S. Calvin, V.G. Harris, *J. Appl. Phys.* 93 (2003) 7489
24. D. J. Fatemi, V. G. Harris, V. M. Browning, and J. P. Kirkland, *J. Appl. Phys.* 83, 6867 (1998)

25. Y. Bao, A. B. Pakhomov, and Kannan M. Krishnan, *J. Appl.Phys.* **99**, 08H107 (2006)
26. G. F. Goya, T.S.Berquo, F.C.Fonseca, and M P Morales , *J. Appl. Phys.* **94**, 3520-27 (2003)
27. Jing Feng, Li-Qin Guo, Xiaodong Xu, Shu-Yan Qi and Mi-Lin Zhang , *Physica B: Condensed Matter* **394** 100-103 (2007)
28. Jose. M. Vargas et al, *Nanotechnology* **16** S285-90 (2005)
29. D.Tripathy and A. O. Adeyeya, C. B. Boothroyd, and S. N. Piramanayagam, *J. Appl.Phys.* **101**, 013904 (2007)
30. R. Bickford, J. M. Brownlow, and R. F. Penoyer , *Pro.IEE - Part B: Radio and Electronic Engineering* **104** 238 – 244 (1957)
31. Victoria L. Calero-DdelC, and Carlos Rinaldi, *J. Magn. Magn. Mater* **314** 60–67 (2007)

## *Chapter 5*

### **Superparamagnetic iron oxide nanoparticles based aqueous ferrofluids for biomedical applications**

Bio-compatible magnetic fluids having high saturation magnetization find immense applications in various biomedical fields. Aqueous ferrofluids of superparamagnetic iron oxide nanoparticles with narrow size distribution and high shelf life is realized by a controlled chemical co-precipitation process. Particle sizes are evaluated by employing transmission electron microscopy. Room temperature and low temperature magnetic measurements were carried out with a superconducting quantum interference device. The fluid exhibits good magnetic response even at very high dilution (6.28mg/cc). Based on the structural and magnetic measurements, the power loss for the magnetic nanoparticles under study is evaluated over a wide range of radio frequencies. The iron oxide nanoparticles were embedded in silica synthesized through Stober process, and suspended in polyethylene glycol. The nanoparticles exhibited non interacting nature and enhanced bio-compatibility.

### **5.1. Introduction**

Colloidal suspensions of ultrafine magnetic particles (ferrofluids) have widespread applications in fields such as biology and biomedicine [1-4]. Ferrofluids are synthesized by dispersing nanosized magnetic particles in carrier liquids with suitable surfactants and proper stabilization techniques. The biocompatibility and the ease with which it can be dispersed in water qualify iron oxide based ferrofluid a competent candidate for membrane separation, intraocular retinal repair, early diagnosing, imaging and magnetic hyperthermia for cancer therapy [5], enzyme immobilization of cell targeting, targeted drug delivery [6], in smart ferrogel preparation [7] for controlled delivery of drugs and as magnetic resonance imaging (MRI) contrast enhancing agents [8]. Magnetic nanoparticles–drug conjugate attached to an antibody or hormone can be magnetically guided to the infected tissue and could specifically bind to it while the external magnetic field is on. As the field is removed, the drug will disperse in the whole body, but the amount of drug is small, there will be very little side effects than when the drug is taken to the whole body initially. This provides a platform for optimum dosage of drug. Surface modified magnetic nanoparticles are applied in cell separation such as clean up of bone marrow [9]. This includes fixing of monoclonal antibodies (that has affinity towards the tumor cells), coated magnetic particles to the cells. The tumor cells specifically attach to the nanoparticles and are magnetically separated in a field gradient. The specificity of the nanoparticles could be provided by surface modification with suitable functional molecules.

MRI is one of the powerful techniques in medical imaging, which measures the spin lattice relaxation time ( $T_2$ ), the time that a proton in water takes to achieve thermodynamic equilibrium with the surroundings.  $T_2$  varies for different tissues and when a magnetic particle is loaded to a tissue, the magneto static field generated by

the magnetic nanoparticles can alter the relaxation of proton enhancing the contrast. Iron oxide nanoparticles coated with dextran are biocompatible and is used as contrast enhancing agents [10]. High magnetic moment is required for a contrast agent. The surface area, size and shape of the nanoparticles decide the physical and chemical properties of these particles to a great extent, which in turn decide the performance in various applications [11]. The Brownian relaxation depends on the hydrodynamic volume, which varies with the molecules attached [12] to the magnetic particle. This property can be used for biomolecular sensing. Any shift in relaxation time reflects the properties of the binding and the dynamics of binding [10]. The particle size, and its distribution along with the magnetic and flow properties of the fluid influence the application parameters in biomedicine. The spherical shape and mono dispersibility of SPIONs are often a prerequisite for applications in living tissues [13], since any small deviation in hydrodynamic volume can change the relaxation characteristics, thus leading to misinterpretations. Moreover the particle, the surface coating and the carrier need to be bio-compatible. Thus the optimization of the synthesis of nanoparticles and their conjugation with organic molecules onto the surface becomes very much essential. Aqueous based ferrofluids are the best candidates for practical approach in biomedicine.

Biosensing [14] is another area where the magnetic nanoparticles (MNPs) can be employed. The MNPs are applied in diagnostic techniques where the pathogens or cells in biological samples are sensitively measured. This includes early detection and diagnosis of tumors, monitoring malignancy and sensing the efficacy of treatment. Diagnostic magnetic resonance (DMR) is a technique in which the MNPs act as proximity sensors, which modulates the spin-spin relaxation of the water molecules surrounding the nanoparticles due to the strong field produced by them.

Hyperthermia refers to the degeneration of living tissues by heating the cells. This technique is applied to destroy the malignant cells in cancer treatment. Magnetic hyperthermia is superior to other techniques of hyperthermia for cancer treatment because of reduced side effects such as damage to healthy tissues [15]. Magnetic hyperthermia or magneto-thermo cytolysis refers to heating of cells attached to magnetic particle by an external AC magnetic field. The increase in temperature is caused due to hysteresis loss/ Neel relaxation. In the case of superparamagnetic particles, the loss is caused by the relaxation processes [16]. The heat dissipated when subjected to an alternating magnetic field depends on the fluid properties such as viscosity, the ratio of relaxation frequency to the applied frequency, distribution of the magnetic component, domain magnetization and density and the specific heat capacity of the magnetic constituent [17]. The heat produced in external magnetic field raises the temperature of the tissue and this causes the rupture of cells.

The stability of the fluid against sedimentation is decided collectively by competing interactions [1, 18-20] such as van der Waals interactions, dipolar interactions, viscous force of the carrier liquid, and the electrostatic and steric repulsion of the surfactant. Surfacted ferrofluid have a long chain of organic molecule such as oleic acid and oleilamine, around the surface and mainly, steric repulsion provides stabilization. In ionic fluids, the electrostatic repulsion provides stabilization. Hence the pH of such fluids may vary considerably (from 3 to 9) from acidic to basic depending on the surface treatment of the nanoparticles after precipitation. Biomedical applications require the fluid to be in neutral pH. Citric acid, a biocompatible surfactant presents both electrostatic and steric effects and could easily get conjugated to iron oxide particles. Iron oxide is most recommended because of its higher magnetization values, lesser toxicity [21] and the ease of metabolism by the liver.

The magnetic property of the nanoparticles is decided by the intrinsic magnetic parameters such as magnetization, coercivity and the inter-particle interaction. The interaction of particles modifies the relaxation mechanism [22] and coercivity and this affects the application in living cells. The surface modification of magnetic nanoparticles with inorganic materials like silica can reduce the inter-particle interaction. Moreover the silanol groups present on the surface of silica can bind to different functional groups easily and is highly recommended for bio-functionalisation. The functionality of these chemical species is such that they have affinity to cancerous cells than normal healthy ones. With the surface modification by silica the total size of the particles increases and the stability of suspension demand a different carrier liquid other than water, or a different pH. Polyethylene glycol (PEG) is biocompatible [23] with higher viscosity and can suspend silica modified SPIONs. The iron oxide particles larger than 50 nm are utilized in *in vitro* magnetic separation purposes due to their ferromagnetic behavior, while for *in vivo* biomedical applications iron oxide nanoparticles less than 50 nm are used. Hence, size control over the silica shell is important in the case of the SPION based silica composites for different biomedical applications [22]. The bare nanoparticles due to their smaller size may undergo phagocytosis by the nearby tissues [24]. The silica modification can prevent this as well. The biocompatibility, ease of functionalisation and stability makes the silica coated nanoparticles and their ferrofluids superior for biomedical applications. This core shell structures of iron oxide in silica assemblies are interesting in understanding the fundamental magnetic properties of nanomaterials.

This chapter deals with the synthesis of highly stable water based iron oxide fluid with narrow particle size distribution at neutral pH, and the evaluation of magnetic properties for hyperthermia application. The power loss spectrum of these nanoparticles in an external alternating magnetic field is simulated to investigate the

possibility of applying in AC magnetic heating. The nanoparticles are modified with silica coating that reduces the particle interaction. The cell viability test conducted with these fluids on He La cells was promising and it showed enhanced biocompatibility on silica modification.

## **5.2 Synthesis of iron oxide based and silica modified ferrofluids**

### **5.2.1 Synthesis of aqueous ferrofluids**

Monodispersed iron oxide particles of average size 9.5 nm were synthesized through controlled chemical co-precipitation method. For this, analytical grade anhydrous ferric chloride ( $\text{FeCl}_3$ ) and ferrous sulphate heptahydrate ( $\text{FeSO}_4 \cdot 7\text{H}_2\text{O}$  from Merk) in the molar ratio of 2:1, each in 500ml of distilled water were taken as the starting solution. 12% of aqueous ammonia was added to the solution while stirring at room temperature to supersaturate for the precipitation of the oxide. The rate of reaction was controlled by allowing one drop of ammonia per second to react with this solution until a pH of 10, to get a thick dark precipitate. 5 g of citric acid ( $\text{COOH-CH}_2\text{-C(COOH)(OH)-CH}_2\text{-COOH}$ ) crystals dissolved in 10 ml water was added to this wet precipitate and allowed for further reaction at an elevated temperature of  $80^\circ\text{C}$  while stirring for another 90 minutes. This sample was then washed with distilled water several times for the removal of water soluble byproducts. This is then suspended in distilled water by ultrasound treatment. The obtained fluid was kept for gravity settling of any bare nanoparticles and was then centrifuged at a rotation speed of 3500 rpm to remove any particles that may sediment. The supernatant fluid is extracted for further analysis. The concentration of the magnetic particles is estimated to be 6.28 mg/cc.

### 5.2.2 Synthesis of silica-coated PEG-based ferrofluid

A modified sol-gel synthesis that involves hydrolysis and condensation of TEOS was employed to obtain silica-coated iron oxide ferrofluids. In order to achieve this, 2 g of the above synthesized CA-coated iron oxide ferrofluid was diluted in 10 ml of distilled water. In addition, 5 ml of  $\text{NH}_4\text{OH}$  and 30 ml of ethyl alcohol were added to this solution. This dispersion was homogenized by ultrasonic vibration for 10 minutes. Under continuous and uniform stirring, 1 ml of TEOS was slowly added to this mixture and the temperature was maintained at  $80^\circ\text{C}$ . The resulting precipitate was magnetically decanted. A schematic of the synthesis is presented in (figure 5.1).

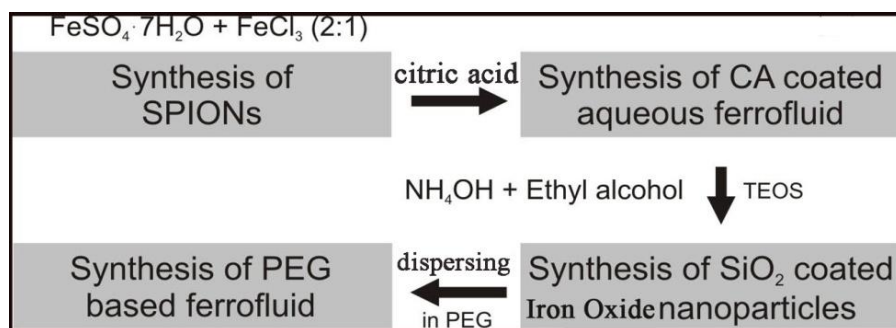


**Figure 5.1: Schematic of silica modified SPIONs suspension in PEG**

One part of the precipitate was dispersed in water followed by extensive ultrasonication while the other part was dispersed in viscous and biocompatible fluid, PEG (viscosity= $1.6 \times 10^{-2}$  Pa.s; density= $1.124\text{g/cc}$ . PEG employed for the present study is PEG 400 (Merck Chemicals, Analytical Grade) with the structure  $\text{HO-CH}_2\text{-(CH}_2\text{-O-CH}_2\text{)}_n\text{-CH}_2\text{-OH}$  and it has  $n=9$ . It was found that the water dispersed  $\text{SiO}_2$ -coated iron oxide nanoparticles (particle size is about 9 nm;  $\text{SiO}_2$  shell is about 280 nm) settle down quickly (figure 5.2a), while dispersed in PEG,  $\text{SiO}_2$ -coated iron

oxides were found to be stable even after 6 months of ageing or under a small external magnetic field (figure 5.2b).

One of the possible mechanisms for the formation of PEG-based stable ferrofluids is schematized in figure 5.2c. Silica shells were formed by the Stober's process [25] within the iron oxide ferrofluid followed by the addition of TEOS in the presence of ethanol and concentrated ammonium hydroxide. The hydrolysis, condensation and polymerization take place leading to the formation of silica nanospheres. During the process of silica nanospheres formation, SPIONs are entrapped within silica shell and this is equivalent to a core-shell structure with SPIONs as the core and silica as the shell. More than one iron oxide nanoparticle can be entrapped within a silica shell. PEG can easily bind with silica through the -OH groups giving rise to stable dispersions. Viscous PEG provides enhanced force of buoyancy for silica-coated magnetic particles than that in water (viscosity of water  $8.9 \times 10^{-4}$  NS/m<sup>2</sup>). The pH of the PEG based ferrofluid was found to be ~7.

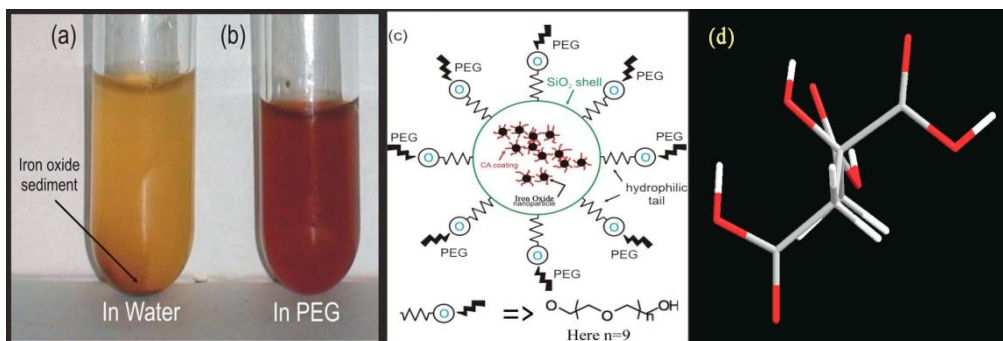


**Figure 5.2: Photograph of the silica modified nanoparticles suspended in (a) Water (b) PEG (c) schematic of silica encapsulated nanoparticles (d) Structure of citric acid**

The structural characterisation is carried out using X-ray diffraction (XRD) technique (Rigaku D Max) at Cu K $\alpha$ . The particles are analysed with transmission electron microscopy (TEM). The samples for the above mentioned experiments are prepared by evaporating the moisture content from the fluid. Room temperature and low temperature magnetic measurements are performed in a Superconducting Quantum Interference Device (SQUID) magnetometer (MPMS Quantum Design). The simulation of the power loss spectrum of the sample is performed for applied field strength of 500 Oe in the range 100 kHz to 1000 kHz. Scanning electron microscopy (SEM, JEOL, JSM-6390LV), energy dispersive spectroscopy (EDS) Fourier transform infrared spectroscopy (FT-IR, Thermo Nicolet Avatar 370 DTGS).

### **5.2.3 Cytotoxicity Assay**

Cytotoxicity of citric acid coated aqueous ferrofluid and silica-coated PEG-based ferrofluid are evaluated by 3-(4,5-dimethylthiazole-2-yl)-2,5-diphenyltetrazolium chloride (MTT) assay[39] Here,  $\sim 1 \times 10^6$  HeLa cells are inoculated into 96 well tissue culture plates containing DMEM supplemented with 10% FBS and incubated for 48h at 37<sup>o</sup>C. The cells are copiously washed with PBS, and the medium is exchanged with DMEM containing different concentrations of ferrofluids. The cells are incubated for 24 hr at 37<sup>o</sup>C and subjected for MTT assay following standard protocol. Briefly, ferrofluid treated cells are supplemented with 50  $\mu$ l of MTT solution (5 mg mL<sup>-1</sup>) prepared in PBS and kept for incubation under dark at 37 <sup>o</sup>C for 5hr. Subsequently, the viability of the cells is measured as a function of reduction of yellow MTT to insoluble purple formazan by mitochondrial dehydrogenase enzyme of healthy cells. Formazan crystals were dissolved in Dimethyl Sulphoxide (DMSO, HiMedia) and the absorbance was recorded at 570 nm

using a microplate reader (InfiniteM-200 Tecan, Austria). Each experiment is repeated six times, and mean and standard error were calculated.

### 5.3 Results and Discussion

The fluids exhibited good shelf life and stability against sedimentation under gravitational and magnetic fields. When an external magnetic field is applied normal to the free surface, fluid of citric acid coated SPIONs exhibited good spiking.

#### 5.3.1 Structural and morphological analysis

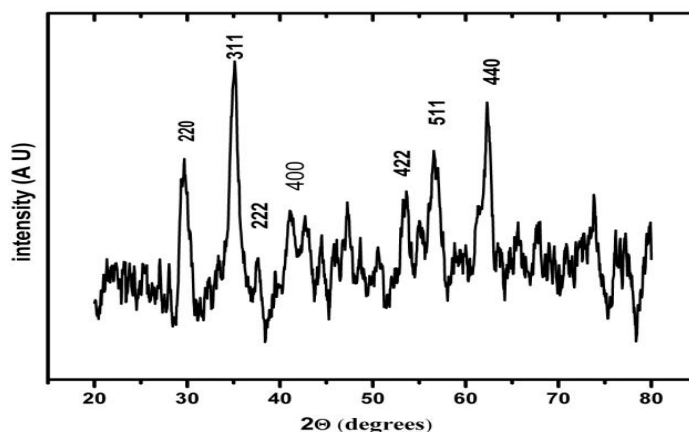


Figure 5.3: XRD pattern of the SPIONs.

The X-ray diffraction pattern (Figure 5.3) shows that the iron oxide particles have crystallized in the inverse spinel structure with a lattice constant of 8.41Å. All the major crystallographic planes corresponding to inverse spinel are identified [ICDD PDF No.750449]. It is hard to differentiate between maghemite ( $\gamma$  Fe<sub>2</sub>O<sub>3</sub>) and magnetite (Fe<sub>3</sub>O<sub>4</sub>) using X-ray diffraction analysis alone, since both represent an inverse spinel structure and the (hkl) planes are similar. However from XRD analysis it is seen that the compound contains no traces of nonmagnetic haematite ( $\alpha$ -Fe<sub>2</sub>O<sub>3</sub>).



The narrow size distribution is an advantage while considering the magnetic hyperthermia applications or for targeted drug delivery. The hydrodynamic length of a single citric acid molecule is calculated to be nearly 0.7 nm. This is the thickness of the surfactant monolayer. So there is a minimum spacing of 1.4 nm between the iron oxide nanoparticles. This could result in dipolar interactions among the particles.

The dipolar interactions can be brought down if a surface coating on the magnetic particles is possible. This is realized by silica modification of magnetic nanoparticles.

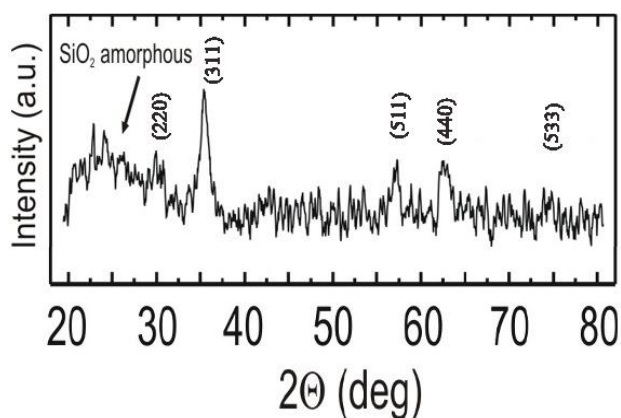


**Figure 5.5: X-ray diffraction pattern of silica coated iron oxide**

Figure 5.5 shows the XRD pattern of silica modified SPIONs. A broad peak is seen at around  $20^\circ$  corresponding to amorphous silica. Particle size of iron oxide calculated from the diffraction peak is about 9.3 nm, which shows that the particles have not grown while silica is coated.

The nature of bonding in the PEG-based ferrofluid was further investigated using FT-IR (figure 5.6). The spectrum of  $\text{SiO}_2$ -modified iron oxide nanoparticles dispersed in PEG has characteristic bands of both silica and iron oxide [26]. The

spectrum shows the characteristic peaks of Fe-O ( $673\text{ cm}^{-1}$ ), C-O (from PEG), Si-O-Si and Si-OR (a broad peak centered at  $1078\text{ cm}^{-1}$ ) bonds. The peaks at  $885\text{ cm}^{-1}$  and  $944\text{ cm}^{-1}$  can be assigned to symmetric and asymmetric stretching vibrations of the terminal groups of Si-OH and Si-O-R. The frequency mode which is at  $1078\text{ cm}^{-1}$  is associated with the back and forth motion of the oxygen atom along a line parallel to the Si-Si axis. This motion results in the opposite distortion of two neighboring Si-O bonds. A weak band is observed at  $830\text{ cm}^{-1}$  due to symmetric stretching of the oxygen atom along a line bisecting the Si-O-Si angle. The absence of a band at  $857\text{ cm}^{-1}$  in the spectrum suggests that there is no Si-O-Fe bond in the composite. The latter indicates that iron oxide is in an isolated state. Moreover, the presence of silanol bonds establishes the hydrophilic nature of silica shell and hence this also confirms the formation of the stable ferrofluid with PEG as carrier fluid. The PEG based ferrofluid remained stable even after an ageing for six months.

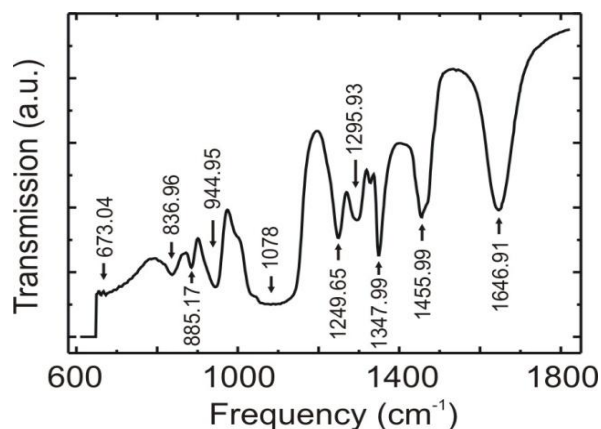


**Figure 5.6: FTIR spectrum on silica modified iron oxide**

The SEM and TEM images of the silica-coated iron oxide nanoparticles are shown in figure 7. The SEM image confirms the formation of white spherical

particles having an average size of 280 nm (figure 5.7a). The enhanced size is attributed to the silica coating.

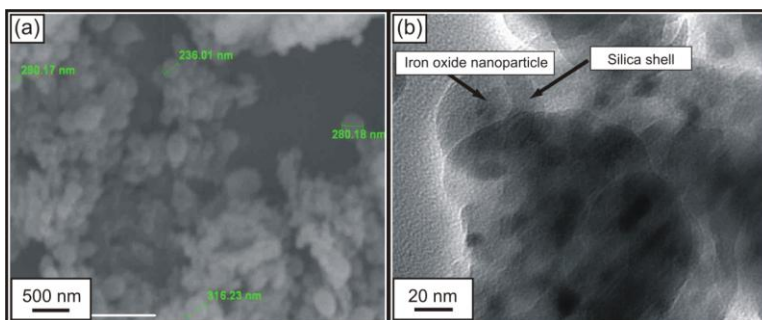


**Figure 5.7: (a) SEM image, (b) TEM image of the silica coated iron oxide**

Figure 5.7b depicts the bright field TEM image of silica-modified iron oxide nanoparticles. The contrast difference indicates that iron oxide and silica forms core-shell structures. Also it is to be noted that a single silica shell contains more than one iron oxide nanoparticle. The size of the iron oxide nanoparticles found in TEM is ~10 nm and correlates well with that calculated from XRD. The elemental analysis using EDS was carried out revealing the presence of Si, Fe and O. The molar mass ratio between iron oxide and Silica, calculated from the relative atomic percentage of Fe and Si from EDS, is found to be 1:17. Figure 5.8a shows the bright field TEM image of silica-modified iron oxide nanoparticles for which elemental mapping has been carried out and is shown in figure 5.8b-d.

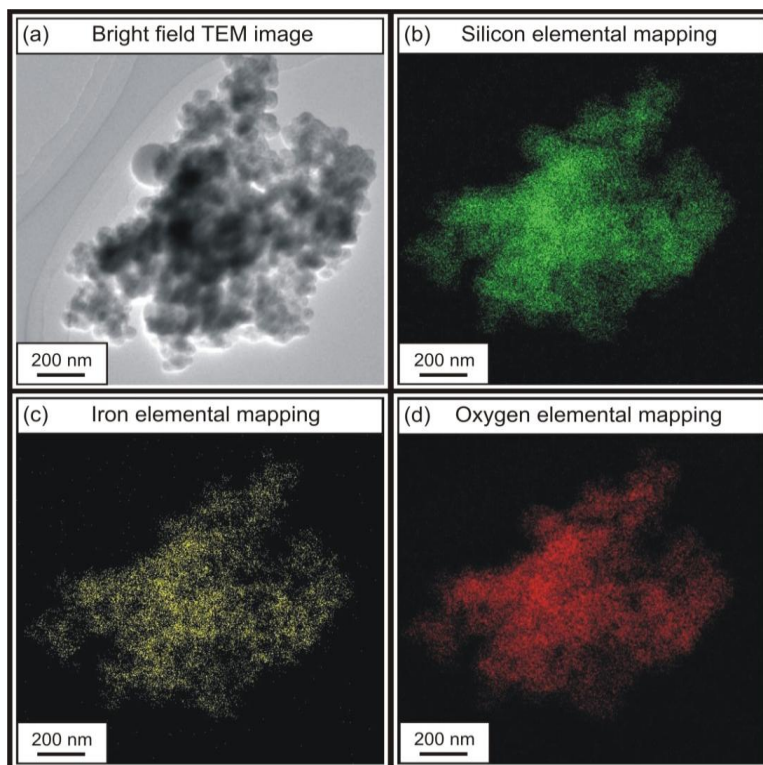


**Figure 5.8: SiO<sub>2</sub>-coated Iron Oxide nanoparticles (a) bright field TEM image (b-d) elemental mapping of Si, Fe and O, respectively**

It is to be noted that uniform colour distribution was obtained for Fe, Si and O indicating the uniform distribution of core-shell nanostructure.

### **5.3.2 Magnetic characterization**

For magnetization measurements, 3 micro litres of the fluid was dropped over to a quartz substrate and the base liquid was allowed to evaporate. Magnetic hysteresis loops of SPIONs were measured at room temperature and at a low temperature of 6 K and are depicted in figure 5.9. Field cooled (FC) and zero field

cooled (ZFC) magnetization measurements were carried out from 6 K to 300 K at an applied field of 30 mT.

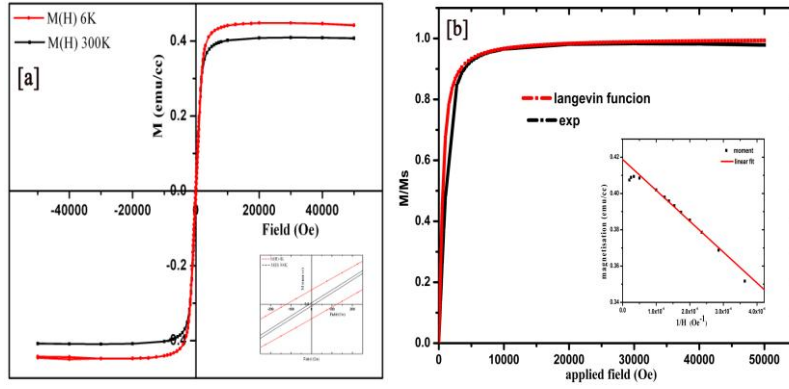


**Figure 5.9: (a) Hysteresis loops of FF CA particles; inset enlarged view at low applied fields (b) Theoretical fitting of normalized moment with Langevin function (Inset) Magnetization -  $H^{-1}$  plot for iron oxide nanoparticles**

The room temperature M-H loop exhibits negligible coercivity (9 Oe) and remanence, which signifies the superparamagnetic nature of particles. This is further verified by fitting experimental curve with the modified Langevin function [27] for the particles with normal size distribution (figure 5.9b).

$$M / M_s = L(a), \text{ where } a = mH / k_B T \quad (5.1)$$

$$\text{and } L(a) = \text{Coth}(a) - 1/a \quad (5.2)$$

with normal distribution of particles having a width “ $b$ ” the function get modified to

$$L(a) = (1/2ba) \ln \frac{(1-b) \sinh(a(1+b))}{(1+b) \sinh(a(1-b))} \quad (5.3)$$

where  $M$  is the magnetic moment for an applied field  $H$ ,  $M_s$  is the spontaneous magnetization,  $k_B$  is the Boltzmann constant and  $T$  the temperature.

At 6 K the coercivity is 125 Oe and the particles are in a thermodynamically blocked state. This is evident from ZFC measurement also. The saturation magnetization at room temperature, calculated by extrapolating the linear portion of magnetisation versus inverse of the applied field at higher field values is 0.418 emu/cc(Figure 9b (inset)). For a concentration of 6.288 mg/cc, the specific magnetization of the magnetic particles is 67emu/g. It is clearly seen that the magnetic moment is saturated at low applied fields and there is no further variation of moment even at high applied fields. If there are any traces of hematite, the moment even at high applied fields would not have been saturated. This is yet another evidence for the non occurrence of nonmagnetic iron oxide phase.

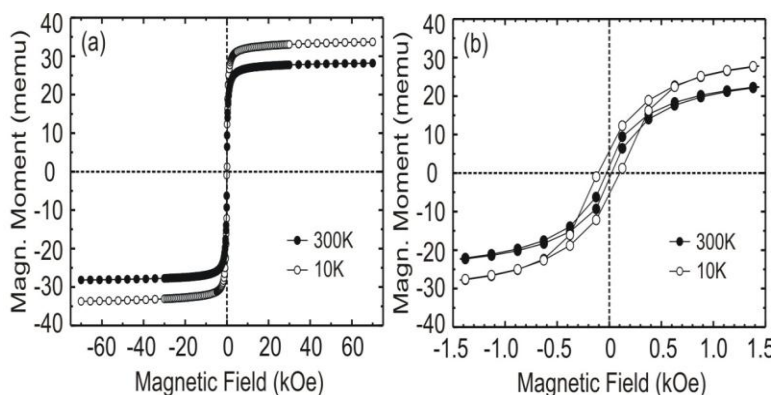


**Figure 5.10: Hysteresis curves of silica coated SPIONs**

The specific magnetization of 67 emu/g for SPIONs is reasonably a good value and is sufficient for biomedical applications. The  $M(H)$  hysteresis loops of  $\text{SiO}_2$ -coated iron oxide nanoparticles taken at 300 and 10 K are depicted in figure 5.10a. The silica-modified iron oxide nanoparticles exhibited negligibly small remanence as well

as coercive field ( $H_C = 14$  Oe) at room temperature (figure 5.10b). This shows that the particle growth has not occurred during the process of silica modification

The hysteresis loop opens at lower temperatures and coercivity increases to  $H_C = 122$  Oe at 10 K. The latter, accompanied with an increase of the saturation magnetization, which is expected for the nanoparticles [28] as the thermal randomization is decreased.

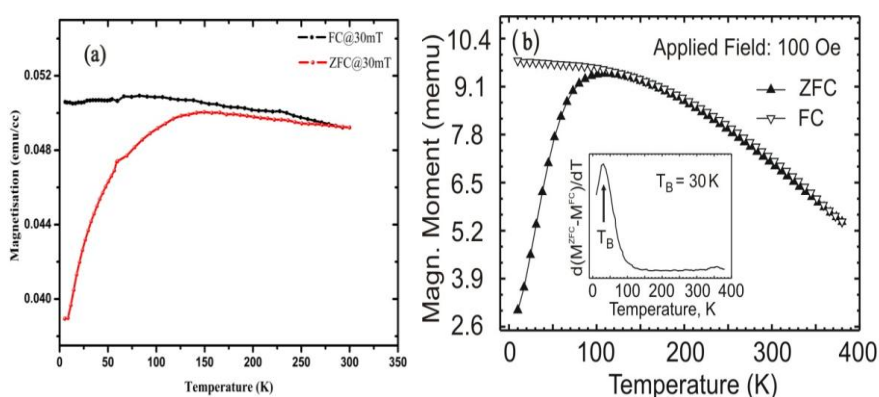


**Figure 5.11: (a) Zero Field Cooled (ZFC) and Field Cooled (FC) moment variation at 30mT. 10 (b) ZFC/FC on Silica-SPIONs at 10mT**

The effect of thermal activation and magnetic relaxation was studied by measuring zero-field and field cooling (ZFC/FC) curves. The ZFC and FC moments were measured at an applied field of 30mT (Figure 5.11a). The ZFC shows a broad blocking behaviour with a maximum moment at 140K, and above this temperature, it decreases gradually. This signifies the distribution of energy barriers present in the sample, and that they act as an ensemble of interacting fine particles. This may be collectively due to the randomly oriented surface spins, the size distribution [29, 30], and the inter-particle interactions. However, the presence of surfactant may eliminate the surface anisotropy as is reported by Roca et al [31]. The hydrodynamic length of citric acid is nearly 0.7nm that gives a physical separation of 1.4nm between

particles' surfaces, since the base liquid has been dried off before subjecting to magnetization measurements. Thus there could exist among particles strong dipolar interaction that cause an increase in the effective energy and enhanced magnetic volume. This explains the increased value for the blocking temperature from the expected one. It's also seen that both the FC and ZFC curves show almost little decrease with temperature which establishes the inter particle interaction that competes the thermal fluctuation [32].

The interacting nature and hence the enhanced magnetic volume will spoil the performance in biomedical applications. The ZFC/FC measurements were carried out on powder samples of silica modified SPIONs, before dispersing them in PEG. For the FC study, the temperature changes from 300 down to 5 K in the presence of a small magnetic field. Figure 5.11b depicts the ZFC/FC measurements carried out on the silica-modified iron oxide nanoparticles at 100 Oe. The behavior of ZFC/FC curves is typical for the system of non interacting superparamagnetic particles, which is an essential criterion for their applicability in medical therapy.

These properties are not seen in ferrofluids prepared from CA-coated iron oxide nanoparticles (figure 5.11a) indicating that the SiO<sub>2</sub> surface modification can successfully tune the magnetic properties as well as the inter-particle interactions. The ZFC/FC curves for SiO<sub>2</sub>-coated iron oxide nanoparticles bifurcate at a temperature of about 115 K, which is close to the  $T_{max}$  on the ZFC (100 K). The latter suggests a rather narrow distribution of blocking temperatures of individual nanoparticles in assembly indicating a narrow particle size distribution [33, 34]. The blocking temperature is related to the distribution of energy barriers [35, 36] and can be estimated from the first derivative on temperature of the difference between the ZFC and FC moments (inset in figure 5.11b). The maximum of the derivative corresponds

to the blocking temperature of  $T_B = 30$  K. This value is related to the nucleation volume,  $V$ , responsible for the magnetization reversal in magnetic nanoparticles. Assuming a thermally activated magnetization reversal with a switching rate following the Arrhenius law with a time constant  $\tau_m$  (related to the measurement time, typically 100 s), the nucleation volume can be estimated using the expression  $K \cdot V = k_B T_B \cdot \ln(\tau_m/\tau_0)$ , with  $K$  being the anisotropy constant of  $\text{Fe}_3\text{O}_4$  nanoparticles and  $\tau_0 \approx 10^{-10}$  s an attempt frequency. The magnetic anisotropy constant of about  $3 \times 10^5$  erg/cm<sup>3</sup> was measured for  $\text{Fe}_3\text{O}_4$  nanoparticles [37, 38]. Using the experimentally determined value for  $T_B$ , the nucleation volume of  $345$  nm<sup>3</sup> was found, which corresponds to the diameter of about  $8.7$  nm for a spherical nanoparticle. The latter is in a good agreement with the size of the iron oxide nanoparticles extracted from XRD and TEM data.

### 5.3.3 Theoretical analysis for magnetic heating

Since the hysteresis is almost negligible as is concluded from M-H loop, the power dissipation is due to the relaxation processes. The power loss produced in an applied AC magnetic field as a function of the relaxation time is given by [39, 40]

$$P = \frac{(mH\omega\tau)^2}{2\tau V k_B T (1 + \omega^2 \tau^2)} \quad (5.4)$$

where  $m$  is the magnetic moment of the particle,  $V$  the particle volume,  $\tau$  the relaxation time,  $H$  is the strength of the applied external magnetic field and  $\omega$  is the angular frequency of the applied AC magnetic field. The relaxation is assumed to be arising from both Brownian and Neel relaxation mechanism and the total relaxation time  $\tau$  is given by the equation

$$\frac{1}{\tau} = \frac{1}{\tau_N} + \frac{1}{\tau_B} \quad (5.5)$$

the Neel relaxation time  $\tau_N$  is [40]

$$\tau_N = \frac{\sqrt{\pi} \tau_o \exp(KV / k_B T)}{2 \sqrt{KV / k_B T}} \quad (5.6)$$

and the Brownian relaxation time  $\tau_B$  is

$$\tau_B = \frac{4\pi\eta r^3}{k_B T} \quad (5.7)$$

where  $\tau_o$  is the characteristic time constant  $\sim 10^{-9}$  s, K the anisotropy constant,  $\eta$  is the viscosity of the medium, and r the hydrodynamic radius of the particle. Since the viscosity of living tissue is very high, the Brownian relaxation time becomes very large. So Neel relaxation dominates when the particle is functionalized and introduced for hyperthermia application in the living cells. So the power loss and hence the heat generated becomes a function of domain magnetization, anisotropy and volume of the particle for an AC field of fixed strength and frequency.

The anisotropy constant K is calculated from the relation

$$KV = 25 k_B T_B \quad (5.8)$$

where  $T_B$  is the blocking temperature obtained from the ZFC measurements. The anisotropic constant calculated is of the same order as that of bulk iron oxide ( $1.1 \times 10^5$  erg/cc) [41] and is closer to the values reported in literature for iron oxide suspended in water [42, 43].

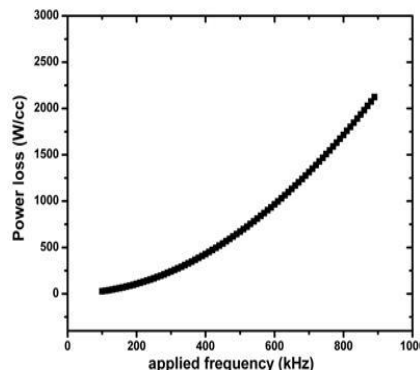


**Figure 5.12: Power loss spectrum as a function of AC frequency for the ferrofluid**

The power loss (also known as specific absorption rate SAR) of the prepared fluid particles, simulated as function of AC frequency in the range of 100 kHz to 900 kHz is plotted and is presented in figure 5.12. The results obtained are consistent with the earlier calculations carried out by Okawa *et. al.* [39], where the power loss for varied sizes is evaluated at a noninvasive frequency 120 kHz. Zhang *et.al* [44] has reported the SAR variation with particle size at still lower frequency of 55 kHz. The applied frequency for maximum power loss depends on the magnetic diameter where the Neel mechanism alone is considered. It is reported that the optimum size for non invasive frequencies lie around 12-14 nm [39]. Recent simulations [45] show that the power dissipation at an applied frequency of 800 kHz is 80 W/g and for 200 kHz, 10 W/g for an applied field strength of 200 Oe. In this study the corresponding values of power loss are 330 W/g and 20 W/g respectively. Li *et. al.* [42] studied the variation of SAR with the viscosity of the fluid in which an increase in SAR with viscosity was reported till twice the viscosity of water. However at 55 kHz and 200 Oe, for water suspended fluids, they obtained a power loss of 57 W/g. It is seen from figure 12 that the power loss increases with frequency. The optimum frequency for required heat generation could be selected on the basis of the actual experimental condition where magnetic hyperthermia needs to be performed.

### 5.3.4 Cytotoxicity of Ferrofluid Nanoparticles

Biocompatibility and non-toxicity are the prerequisites which determine the relevance of nanoparticles in *invitro* or *invivo* applications. Figure 13 shows the viability of HeLa cells in the presence of different concentrations of citric acid coated aqueous ferrofluid and silica-coated PEG-based ferrofluid nanoparticles. Here, we incubated HeLa cells with 0.1 - 1000  $\mu\text{g mL}^{-1}$  concentrations of ferrofluid nanoparticles for 24 hours and the viability was measured as a function of mitochondrial dehydrogenase enzyme production using MTT assay. It is observed that the silica-coated nanoparticles were not toxic to HeLa cells in culture up to a concentration of 100  $\mu\text{g mL}^{-1}$ .

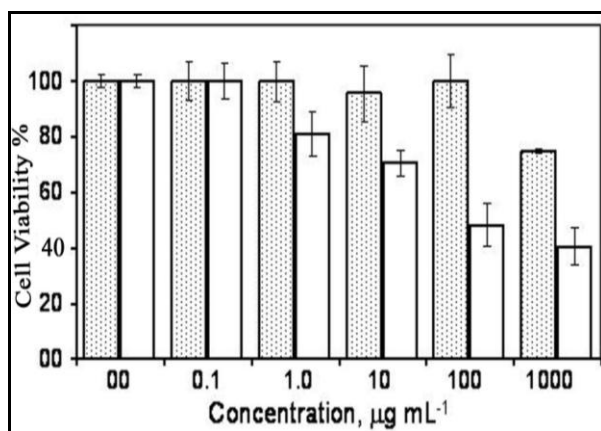


**Figure 5.13:** Histograms of MTT assays for HeLa cells incubated with different concentrations of citric acid coated aqueous ferrofluid (Bars with no pattern) and silica-coated PEG-based ferrofluid (Bars with dotted pattern). Values are given as percentage cell viability  $\pm$  standard Error

However, the viability was decreased by  $\sim 25\%$  when the concentration was further increased to 1000  $\mu\text{g mL}^{-1}$ . MTT assay results for citric acid coated aqueous ferrofluid nanoparticles show that the viability decreased progressively with

increasing concentration of nanoparticles and reached a minimum of ~40% viability with 1000  $\mu\text{g mL}^{-1}$ . MTT assay is standard for quantifying the redox activity of mitochondrial dehydrogenase enzyme in living cells, and any decrease in the reduction of MTT is an index of mitochondrial damage and cell death. The cell viability test shows that the silica encapsulation enhances the compatibility, and the temperature dependant magnetic moment variation shows the reduction in inter-particle interaction due to surface modification with silica.

### **5.3.5 Optical measurements**

The synthesis of  $\text{SiO}_2$ -coated iron oxide ferrofluids open possibilities for synthesizing multifunctional ferrofluids having both magnetic as well as optical properties, such as photoluminescence. A number of researchers have reported the photoluminescence properties of silica nanoparticles, nanoshells and nanospheres [46, 47]. Attempts to observe photoluminescence on  $\text{SiO}_2$ -modified iron oxide ferrofluids were in vain. Pure silica nanospheres and nanoshells are supposed to be exhibiting luminescence at about 450 nm with an excitation wavelength of 360 nm. The SPIONs have an optical band gap of  $\sim 2.65$  eV (465 nm) as obtained from optical measurements. The diffused reflectance spectroscopy was employed to calculate the band gap of the  $\text{Fe}_3\text{O}_4$  nanoparticles. The band gap was measured from tauc plots of  $(\alpha h\nu)^2$  versus  $h\nu$ . The analysis shows that the direct band absorption takes place at energy of 2.65 eV (465 nm) (figure 5.14), and is matching with the reported bandgap values of ultrafine  $\text{Fe}_3\text{O}_4$ [48]. The obtained value is close to the luminescence line (450 nm) of the silica nanoshells [49]. This may cause the effective quenching of the luminescence of silica by iron oxide nanoparticles. Hence, the incorporation of SPIONs in the silica matrix might have resulted in the quenching of the luminescence of silica by absorbing this radiation as it is already observed in various heterostructures [50-52]. Time resolved measurements are required to probe the

photoluminescence quenching properties of these core-shell heterostructured ferrofluids. The silica modification of the iron oxide nanoparticles opens the possibility for hybridizing their surface with various biocompatible dyes, and then these ferrofluids can exhibit multifunctional properties such as both magnetic and optical properties

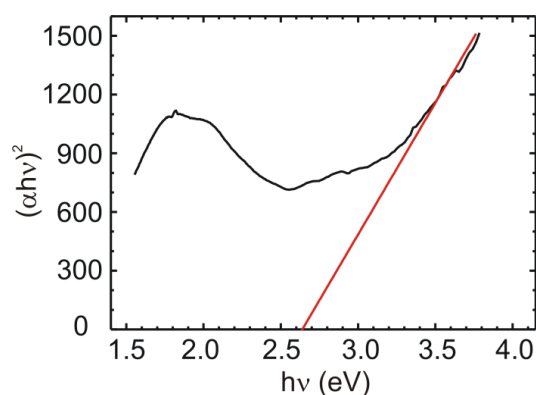


**Figure 5.14: Band gap calculation for  $\text{Fe}_3\text{O}_4$  nanoparticles using Tauc relation.**

#### **5.4 Conclusion**

Highly stable aqueous ferrofluid of SPIONs with citric acid as surfactant has been synthesized by controlled chemical co-precipitation method. The structural investigation by XRD and TEM show good tuning in respect of the particle size of 9.5 nm. The narrow size distribution obtained is highly desirable for biomedical applications, since the relaxation time varies with the size, and distribution in size will lead to distribution of relaxation time. The magnetic analysis shows that the nanoparticles are superparamagnetic in nature and hence the coercivity is negligible. The saturation magnetization value of 67 emu/g for the synthesized water based fluid is suitable for various biomedical applications especially for magneto hyperthermia. Based on the magnetic measurements, the power dissipation in an alternating

## *Chapter 5*

---

magnetic field of 500 gauss as a function of applied frequency is calculated. The results reveal the possibility of employing these nanoparticles in magnetic hyperthermia. In order to enhance the cell compatibility and to reduce the inter particle interaction, the SPIONs were surface modified with silica by Stober process. The analysis shows the particles are embedded in silica and are magnetically non interacting and hence good from a biomedical application point of view.

**References**

1. Catherine C. Berry, *J. Mater. Chem.* 15, 543–547 (2005)
2. D. K. Kim, M. Mikhaylova, F. H. Wang, J. Kehr, B. Bjelke, Y. Zhang, T. Tsakalakos, M. Muhammed, *Chem. Mater.* 15, 4343 (2003).
3. N. A. Brusnetsov, V. V. Gogosov, T. N. Brusnetsova, A. V. Sergeev, N. Y. Jurchenko, A. Kuznetsov, O. A. Kuznetsov, L. I. Shumakov, *J. Magn. Magn. Mater.* 225, 113 (2001)
4. D. L. Holligan, G. T. Gillies, J. P. Dailey, *Nanotechnology* 14, 661 (2003).
5. C. C. Berry, A. S. G. Curtis, *J. Phys. D: Appl. Phys.* 36, R198 (2003).
6. M. Babincova, V. Altanerova, C. Altaner, C. Bergeman, P. Babinec, *IEEE Trans. Nanobioscience*, 7, 15 (2008).
7. T. Y. Liu, S. H. Hu, T. Y. Liu, D. Liu, S. Y. Chen, *Langmuir* 22, 5974 (2006).
8. Lutz J F, Stiller S, Hoth A, Kaufner L, Pison U and Cartier R, *Biomacromolecules*, 7, 3132 (2006)
9. C. Scherer, Figo A. M. Neto, *Braz. J. Phys.* 35 3, 718 (2005).
10. Y. Bao, A. B. Pakhomov, and Kannan M. Krishnan, *J Appl.Phys.* 99 08H107(2006).
11. P. Tartaj, M. P. Morales, S. Veintemillas-Verdaguer, T. Gonzalez-Carreno, C. J. Serna *J. Phys. D: Appl. Phys.* 36 , R182 (2003).
12. S.-H. Chung, A. Hoffmann, K. Guslien, S. D. Bader, C. Li, B. Kay, L. Makowski, and L. Chen *J. Appl.Phys.* 97 10R101 (2005)
13. A. Petri-Fink, H. Hofmann, *IEEE Trans. Nanobioscience* 6 (4) , 289 (2007).
14. H. Shao, T-J Yoon, M. Liong, R. Weissleder and H. Lee, *Beilstein J. Nanotechno.* 1 142 (2010)

15. Q. A. Pankhurst, J. Connolly, S. K. Jones, J. Dobson, *J. Phys. D: Appl. Phys.* **36**, R167 (2003)
16. R. Hiergeist, W. Andrä, N. Buske, R. Hergt, I. Hilger, U. Richter, W. Kaiser, *J Magn.Magn.Mater.* **201**, 420 (1999).
17. J. Giri, P. Pradhan, T. Sriharsha, D. Bahadur, *J. Appl. Phys.* **97**, 10Q916 (2005)
18. R. E. Rosensweig, *Ferrohydrodynamics*, Cambridge University Press, New York, 1985
19. E. Dubois, V. Cabuil, F. Boue, R. Perzynski, *J. Chem. Phys.* **111** , 7147 (2001).
20. J. de Vincente, A. V. Delgado, R. C. Plaza, J. D. G. Duran, F. Gonzalez-Caballero, *Langmuir* **16**, 7954 (2000).
21. L. F. Pavon, O. K. Okamoto, *Einstein* **5**, 74 (2007).
22. D. K. Kim, M. Mikhaylova, Y. Zhang and M. Muhammed, *Chem. Mater.* **15**, 1617 (2003).
23. Ajay Kumar Gupta and, Mona Gupta, *Biomaterials* **26** (2005) 3995–4021
24. Zeljka Krpeti, Francesca Porta, Enrico Caneva, Vladimiro Dal Santo, and Giorgio Scari Phagocytosis of Biocompatible Gold Nanoparticles, *Langmuir*, **26**(18) 14799–14805 (2010)
25. Xiao-Dong Wanga, Zheng-Xiang Shena, Tian Sanga, Xin-Bin Chenga, Ming-Fang Lib, Ling-Yan Chena and Zhan-Shan Wanga, *Journal of Colloid and Interface Science* **341**, 23-29 (2010)
26. R. M. Silverstein and G. C. Bassler, *Spectrometric identification of organic compounds*, John Wiley and Sons, Inc., New York (1963).

27. T. N. Narayanan, A. P. Reena Mary, M. M. Shajumon, L. Ci, P. M. Ajayan, M. R. Anantharaman, *Nanotechnology* **20**, 055607 (2009).
28. B. D. Cullity, *Introduction to Magnetic materials*, Addison-Wesley Series Publishing Company, Inc. Philippines (1972).
29. S. J. Lee, J. R. Jeong, S. C. Shin, J. C. Kim, J. D. Kim, *J. Magn. Magn. Mater.* **282**, 147(2004).
30. X. Battle, A. Labarta, *J. Phys. D: Appl. Phys.* **35**, R15 (2002).
31. A. G. Roca, M. P. Morales, K. O'Grady, C. J. Serna, *Nanotechnology* **17**, 2783, (2006).
32. J. Dai, J. Q. Wang, C. Sangregorio, J. Fang, E. Carpenter, J. Tang, *J. Appl. Phys.* **87**, 7397, (2000).
33. P. A. Joy and S. K. Date, *J. Magn. Magn. Mater.* **222**, 33 (2000).
34. R. W. Chantrell, N. S. Walmsley, J. Gore and M. Maylin, *J. Appl. Phys.* **85**, 4340 (1999).
35. J. C. Denarding, A. L. Brandl, M. Knobel, P. Panissod, A. B. Pakhomov, H. Liu and X. X. Zhang, *Phys. Rev. B* **65**, 064422 (2002).
36. J. M. Vargas, J. Gómez, R. D. Zysler and A. Butera, *Nanotechnology* **18**, 115714 (2007).
37. J. M. Vargas, E. Lima Jr, R. D. Zysler, J. G. S. Duque, E. De Biasi and M. Knobel, *Eur. Phys. J. B* **64**, 211 (2008).
38. A. D. Arelaroa, E. Lima Jr, L. M. Rossi, P. K. Kiyohara and H. R. Rechenberg, *J. Magn. Magn. Mater.* **320**, 335 (2008).
39. K. Okawa, M. Sekine, M. Maeda, M. Tada, M. Abe, N. Matsushida, K. Nishio, H. Handa, *J. Appl. Phys.* **99**, 08H102 (2006)
40. R. E. Rosenswieg, *J. Magn. Magn. Mater.* **252**, 370, (2002).

41. B. D. Cullity, Introduction to Magnetic materials Philippines: Addison Wesley, London, 1972.
42. Y. Z. Li, -C. G Hong, M. W, Xu, *J. Magn. Magn. Mater.* **311**, 228–233, (2007).
43. M. Ma, Y. Wu, J. Zhou, Y. Sun, Y. Zhang and N. Gu, *J. Magn. Magn. Mater.* **268**,33(2004).
44. L. Y. Zhang, Y. H. Dou, L. Zhang and H. C. Gu, *Chin. Phys. Lett.* **24**, 483, (2007).
45. S. Purushotham and R.V. Ramanujan, *J. Appl. Phys.* **107**, 114701, (2010).
46. S. Thomas, D. Sakthi Kumar, Y. Yoshida and M . R. Anantharaman, *J. Nanoparticle Res.* **10**, 203 (2008).
47. T. N. Narayanan, D. Sakthi Kumar, Y. Yoshida, M. R. Anantharaman, *Bull. Mater. Sci.* **31**, 759 (2008).
48. S. S Nair, M. Mathews and M. R. Anantharaman, *Chem. Phys. Lett.*, **406**, 398 (2005).
49. Y. D. Glinka, S. H.Lin and Y. T. Chen, *Phys. Rev. B*, **66**, 035404 (2002).
50. X. Li, J. Qian, L. Jiang and S. He, *Appl. Phys. Lett.* **94**, 063111 (2009).
51. K. Mazunari, Y. Ito and Y. Kanemitsu, *Appl. Phys. Lett.* **92**, 211911 (2008).
52. H. Li and L. Rothberg, *PNAS* **101**, 14036 (2004).

## *Chapter 6*

### **On the magneto-optical, non-linear optical and microwave absorbing properties of ferrofluids based on Nickel and ferrites**

Ferrofluids, under an external applied magnetic field exhibit a variety of optical phenomena, and these magneto optical phenomena are interesting to find out the field induced aggregation effects and the inter-particle interaction and chain formation. The magneto optical dichroism measurements are carried out on various ferrofluids of hydrocarbon and aqueous base. The intensity variation with respect to applied field for parallel and perpendicularly polarized light is studied. The magneto-controllable optical limiting materials are searched for photonic devices and ferrofluids with suspended nanoparticles could be good candidates. The nonlinear optical properties of the diluted ferrofluids are studied by open aperture z scan method. The fluids exhibit limiting behavior and is explained as a multi photon process. The microwave absorbing properties of a poly vinyl alcohol- magnetite composite derived from ferrofluid is also presented. The absorption studies are carried out using a network analyzer employing cavity perturbation technique and the reflection loss for varied thickness of the flexible thick film is evaluated.

## **6.1 Magneto optics**

Magneto-optical effects are investigated to unravel the properties/electronic structure of atomic, molecular or solid systems. Magneto-optical properties stem from the interaction of magnetic moment vector with the light passing through a magnetically responsive medium. Faraday observed rotation of polarization of light when light travelled through glass placed in an external magnetic field [1]. This is known as Faraday rotation and the geometry is such that the light travels in the direction of the field (longitudinal mode). This is due to the interaction of electric field vector of the incident light with the magnetisation vector of the medium. The magneto optical phenomena are exploited in the reflection mode to study the domain dynamics and the possibility of magneto optical recording devices. In analogy to electro optical Kerr effect, the magneto optical phenomena (rotation of polarization) in the reflection mode is known as Magneto Optical Kerr effect (MOKE) [2-3]. Depending on the direction of path of the incident light and the applied magnetic field, the Kerr effect could be transverse, longitudinal or polar Kerr effects. The magneto-optical (MO) phenomena could be explained on the basis of effective dielectric tensor, which is skew-symmetric and all the terms are complex in nature; the off diagonal elements contribute to the MO effects. The explanations could be derived from the Maxwell equations [3]. Some of the important magneto-optic phenomena are described for the sake of continuity.

Magneto optical effects, in the transmission mode, where the light transmitted through the magnetized medium becomes a function of the strength and direction of the applied magnetic field or magnetisation ( $M$ ), are Faraday rotation, field induced dichroism, magnetic birefringence, and Cotton- Mouton rotation. The absorption, refraction or scattering as well as the rotation of plane of polarization of the light

transmitted through the material become a function of the applied magnetic field or magnetisation of the medium whichever is prominent.

(i) *Magnetic circular dichroism*

A plane polarized light can be considered consisting of a left circularly polarized and right circularly polarized components. In an applied magnetic field the spin splitting occurs in the material and the two components experience different absorption coefficient. This is known to be magnetic circular dichroism (MCD).

(ii) *Faraday rotation and ellipticity*

The polarization of a plane polarized light rotate after passing through a material under magnetic field is Faraday rotation as a result of differential absorption of right circularly and left circularly polarized component when the light incident in longitudinal symmetry. This is related to the spin-orbit interaction. When in magnetic field, the spins are polarized in the direction of applied field. The spin orbit interaction provides an energy to both the circularly polarized components but in opposite directions. This causes the two to have different refractive indices in the material and propagate with different velocity and they combine to have a rotated plane of polarization when emerging from the material.

When the attenuation of the two circularly polarized components is different the plane polarized light turn elliptical and the material is said to have ellipticity.

(iii) *Cotton- Mouton rotation*

This is a transverse M O effect where the light path is perpendicular to the direction of applied field. The plane polarized light turns elliptically polarized after

passing through a magnetized material. This is due to the field induced refractive index change.

(iv) *Magneto optical birefringence and linear dichroism*

Magneto optical effect when the magnetic field is perpendicular to the light incident direction. The refractive index change (real part of complex refractive index) with applied field is known to be magneto optical birefringence. Linear dichroism refers to the differential absorption of parallel and perpendicular polarized light with reference to the magnetic field.

### **6.1.1 Magneto optical effects in ferrofluids**

Ferrofluids are isotropic in nature due to the randomly oriented particles. The field induced structural anisotropy induces a dielectric and hence an optical anisotropy. In applied field the moments try to align in the field direction causing anisotropy. The dielectric characteristics of a ferrofluid subjected to magnetic field are studied on different assumptions. The particles could be shape anisotropic or the anisotropy is induced by interaction that results in chain formation.

In an applied magnetic field a chain like formation occurs in ferrofluid [4]. The chain grows with the strength of the applied field. In zero applied field the interactions result in irregular aggregates, and the fluid remains isotropic. For small fields, shorter chains are formed. As the field increases the chains combine and it saturates when the fluid reaches its saturation magnetization. This proposes a dynamically varying anisotropy of the fluid. The energy of the chain consists of field energy and dipole interaction energy. The length of the chains in the direction and in perpendicular direction to the field would be different owing to this energy criterion. Solving for the dielectric constant [5] can be obtained as

$$\varepsilon_{\text{pep}} = \varepsilon_c + \phi C \left[ 1 - \frac{L(a)}{a} \varepsilon_x + \frac{L(a)}{a} \varepsilon_z - \varepsilon_0 \right] \quad (6.1a)$$

$$\varepsilon_{\text{para}} = \varepsilon_c + \phi C \left[ 2 \frac{L(a)}{a} \varepsilon_x + \left( 1 - 2 \frac{L(a)}{a} \right) \varepsilon_z - \varepsilon_0 \right] \quad (6.1b)$$

Where  $L(a)$  is the Langevin function and  $a = (\mu H / k_B T)$ ,  $H$  the applied magnetic field. The complex refractive indices are related to dielectric constants by the relations,

$$\varepsilon_{\perp} = N_{\perp}^2 = (n_{\perp} + jk_{\perp})^2 \quad (6.2a)$$

$$\varepsilon_{\parallel} = N_{\parallel}^2 = (n_{\parallel} + jk_{\parallel})^2 \quad (6.2b)$$

where  $n$  and  $k$  represent the refractive indices and extinction coefficients in respective directions. This shows that the refractive index varies with field and with light polarization and this leads to birefringence. The absorption also varies with applied magnetic field and nature of polarization relative to the applied magnetic field. Anisotropy in real part of refractive index results in birefringence, exhibited as phase shift in polarization. Anisotropy in transmitted intensity leads to dichroism. This can arise from anisotropic absorption or scattering altering the transmitted intensity.

$$I_{\parallel} = I_0 \alpha_{\parallel} = I_0 \exp[(-4\pi)cLk_{\parallel}/\lambda] \quad (6.3a)$$

$$I_{\perp} = I_0 \alpha_{\perp} = I_0 \exp[(-4\pi)cLk_{\perp}/\lambda] \quad (6.3b)$$

where  $I_0$  is the incident intensity,  $c$  the concentration,  $L$  is the path length in the sample, and  $\lambda$  is the wavelength used. The absorbance varies for both the polarizations as field is applied. The change in absorbance from the zero field value is given by the expression [6]

$$\Delta A_{\parallel} = -\ln(I_{\parallel} / I_0) \quad (6.4a)$$

$$\Delta A_{\perp} = -\ln(I_{\perp} / I_0) \quad (6.4b)$$

The dichroism, which is the difference of the change in absorbance in either polarization which is again a function of applied field, can be written as

$$\Delta A = \Delta A_{\parallel} - \Delta A_{\perp} \quad (6.4c)$$

Dichroism reflects the degree of orientation of moments in fluid under an applied field. This reflects the microstructure formation and its relaxation in field. The dichroism measurements in static as well as dynamic modes [7] are interesting from a fundamental perspective in that it is possible to study the aggregation effects, chain formation and clustering in field, and for many applications such as optical modulators, viscometers, and relaxation time measurement for bio-molecular recognition. The exact mechanism leading to the MO effects in ferrofluids cannot be generalized. In the case of non-interacting particles, it is assumed to be the orientation of moments in the applied field with no agglomeration. The field induced clustering of pre-existing small aggregates or short chains are also studied. The chain formations that can lead to field controlled gratings [8] of desired width, Faraday modulators are some of the proposed [6] applications. The particle motion could be either translational owing to the diffusion of particles in a colloid or rotation in an external field. The Brownian relaxation depends on the viscosity of ferrofluid and hence information about the type of molecular binding can be retrieved from the relaxation studies of a ferrofluid in the case of a functionalised ferrofluid [9]. The relaxation measurements in a dynamic field can give knowledge about attached chemical

species. The diffraction effects in fluids are also explained as a result of thermal lens effects [10].

Here, the static magneto optical dichroism measurements carried out on water based ionic ferrofluids and kerosene based ferrofluids, the synthesis and magnetic properties of which are discussed in previous chapters, are presented. The measurements reveal the magnetic field dependent variation of absorbance of differently polarised light by ferrofluids.

## **6.2 Experiment**

The experimental arrangement is schematised in figure 6.1. A low power (3 mW) diode laser (670 nm) is used to incident on the ferrofluid fluid taken in a sample cell of dimension 1cm x 1cm, with the path of light normal to the direction of the applied magnetic field (figure 6.1). The linear transmittance in zero fields is fixed at 20%. Laser beam chopped by mechanical chopper (C), and polarized by polarizer (P) incident on sample kept in between the pole pieces of electromagnet. The transmitted light is converged by lens (L) to the diode detector. The chopper is synchronized with a lock-in-amplifier (LIA) in such a way that the output signal corresponding to the chopping frequency, from the detector. This reduces the stray signals from being detected.

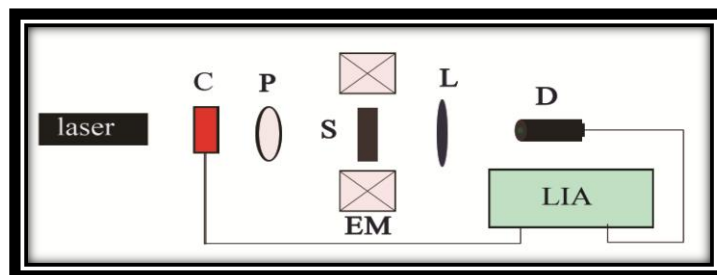


**Figure 6.1: Experimental arrangement for dichroism measurement**

The absorption variation, from the zero magnetic field value, as a function of applied field is measured in transverse mode with the polarisation of the incident light parallel and perpendicular to the applied magnetic field direction. The differential absorption for both parallel and perpendicular polarised light with respect to the field direction are plotted.

### 6.2.1 Linear dichroism on Nickel nanofluid(Ni F)

The dichroism measurements on Ni F (preparation and initial characterization detailed in chapter 3), consisting of nickel nanoparticles of average particle size 5 nm suspended in kerosene, is depicted in figure 6.2a. The absorbance variation as per equation 6.4 is plotted as a function of applied field. The perpendicular absorbance decreases whereas the parallel absorbance increases from the zero field value. At all applied field strengths, the delta absorbance follows the relation for intrinsic dichroism [11-12]

$$\left| \Delta A_{//} \right| = 2 \left| \Delta A_{\perp} \right| \quad (6.5)$$

The change in absorbance for parallel polarised light at a given field strength is double that for perpendicular polarisation, but happens in opposite sense. Figure 6.2b depicts the dichroism i.e the difference of change in absorbance as a function

of applied field. The variation follow langevin nature [4]. The experimental curve is compared with theoretical langevin function. This behaviour is for independant particle orientation forming a one dimensional chain with out any interaction of adjacent chains.

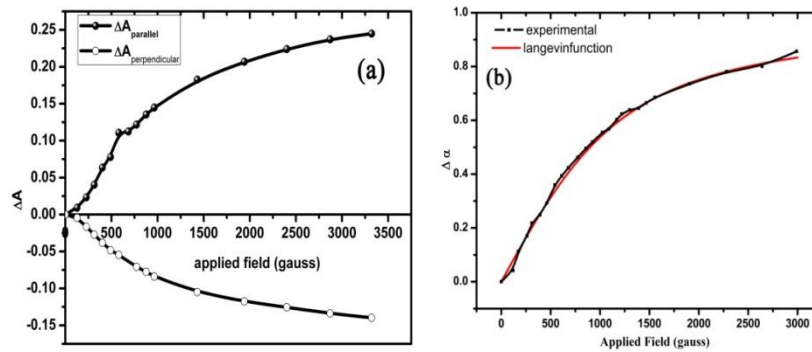


**Figure 6.2: Magneto optical dichroism in Ni F; (a) change in absorbance for parallel and perpendicular polarizations (b) difference of change in absorbance as function of applied field.**

It has been observed that the intensity get back to the zero field value as soon as the field is removed in either polarisation. This indicate the particles are superparamagnetic with least particle agglomeration. The rapid relaxation of the optical transmission points out that the field induced aggregates are short lived with smaller dimensions[13], which happens when the interaction of particle with the applied field has greater strength compared to the inter-particle interaction. The size of the suspended particles are 5nm; the dipolar interaction is very weak and this makes a dilute fluid to be non interacting. The individual particle moments align in the direction independantly and result in magnetisation similar to langevin function variation. This once again shows that the particles in fluid are non interacting in nature.

### 6.2.2 Dichroism studies in oxide fluids

Dichroism measurements are carried out in kerosene based and water based fluids with iron oxide, cobalt ferrite and manganese zinc ferrite nanoparticles suspended. The synthesis routes are explained in chapter 4. Figure 6.3 shows the measurements on  $\text{Fe}_3\text{O}_4$  fluids. It could be seen that the absorbance increases for both polarisation in the oleic acid coated kerosene fluids (figure 6.3a), where as the citric acid coated, water based fluids exhibits dichroic behaviour (figure 6.3b).

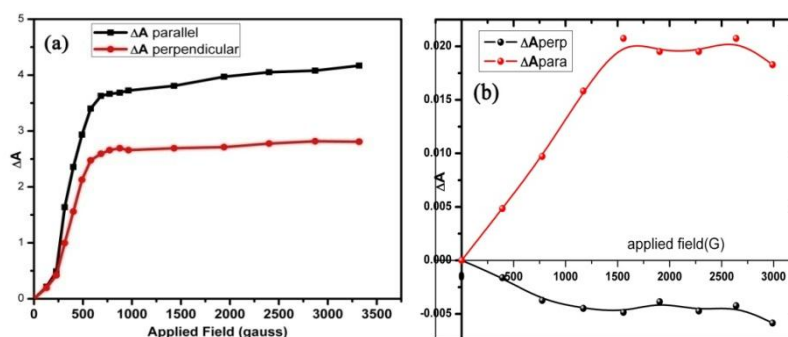


Figure 6.3: Magneto optical dichroism in  $\text{Fe}_3\text{O}_4$  (a): suspended in kerosene (b) in water

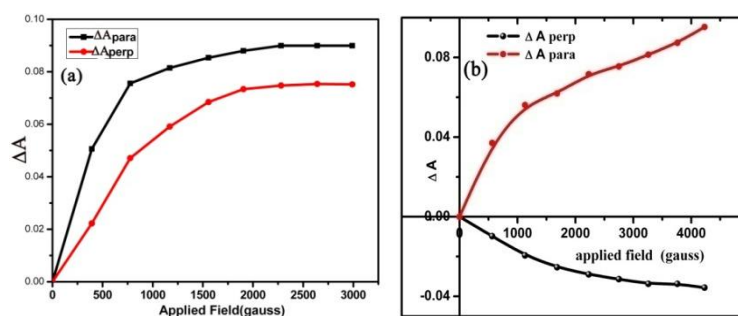
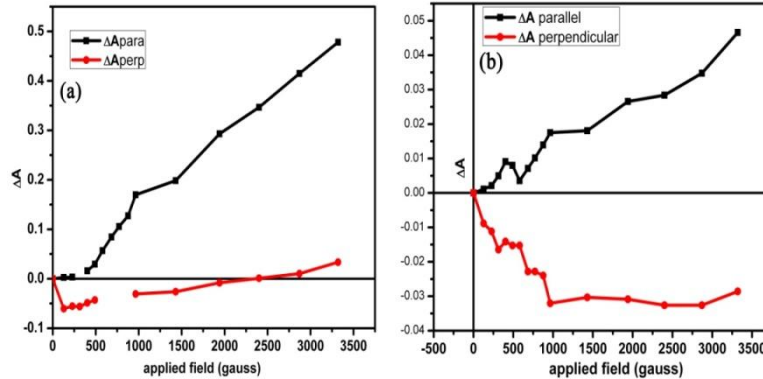


Figure 6.4: Magneto optical dichroism in  $\text{CoFe}_2\text{O}_4$  (a) suspended in kerosene (b) in water



**Figure 6.5: Magneto optical dichroism in  $Mn_{0.6}Zn_{0.4}Fe_2O_4$  (a) suspended in kerosene (b) in water**

The absorption measurements for cobalt ferrite suspensions also exhibited similar behaviour; where in kerosene fluid (figure 6.4a) has absorptions increasing in both polarization, and water fluid (figure 6.4b) shows dichroic nature. This shows that the kerosene based fluids the absorption occurs independent of polarization of the light, whereas the ionic fluids presents differential absorption with field. This can be explained as the citric acid surfacted fluids present electrostatic repulsion and hence in diluted fluids have little clustering effects. So individual moments align in the field direction and follow saturation independently. Whereas in oleic acid coated particles, the dipolar interaction cause local clustering leading to macro clusters. This kind of macro clustering due to the steric interaction turning attractive is reported for suspensions with technical grade oleic acid coated nanoparticles [14]. The scattering occurs from these macro clusters and this causes the decrease of light intensity. It could be noticed that in ionic fluids the light intensity changes faster and get back to zero field value immediately when the field is switched off. Whereas in surfacted fluids there occurs a hysteresis and delay in returning of the light intensity. This could be also be explained as result of strong inter-particle interaction and associated

clustering which increases with field intensity. The adjacent agglomerates combine to form macro clusters and cause scattering. This explains the decrease of transmitted light with field irrespective of the polarization of light in surfacted fluids.

Figure 6.5 depicts the dichroism measurements on manganese zinc ferrite suspensions. The ionic (water based) fluid (figure 6.5b) exhibited differential absorption where as the kerosene based fluid (figure 6.5a) exhibited dichroic nature at low fields and the absorbance variation in parallel and perpendicular polarization are differing in nature. As the field is increased, the variation in absorbance of perpendicular polarized light turned similar to absorbance of parallel polarized light. The clustering can be assumed to be little in zero field condition. As the field strength increased, the interaction between particles also increases and with considerable strength of applied field, clustering leads to scattering and this causes the intensity to vary similar in both cases [13]. The change in absorbance for perpendicular polarized light crosses the x-axis at a field near 2500 gauss to the positive direction indicating the variation to be similar to parallel polarization.

Transmission measurements conducted on iron oxide suspended in poly vinyl alcohol (PVA) stabilized with citric acid (figure 6.6) also exhibited dichroic nature. This establishes that in electrostatically stabilized fluids, the particle moments independently rotate in external magnetic field, and the repulsion between particles prevent them from aggregation. The interaction with field is stronger than the inter particle interaction. The moments get immediately dispersed when the field is removed making them isotropic in nature again.

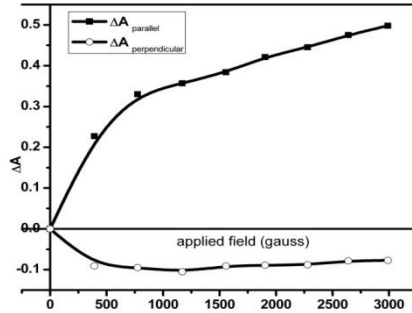


Figure 6.6: Magneto optical dichroism in  $\text{Fe}_3\text{O}_4$  suspended in PVA

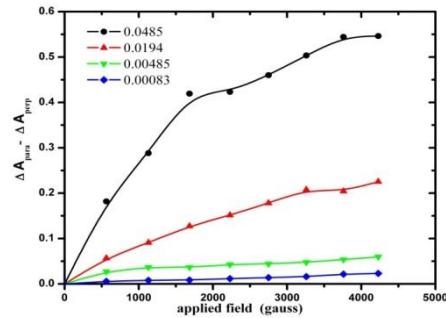


Figure 6.7: Magneto optical dichroism in  $\text{CoFe}_2\text{O}_4$  in water at different magnetic particle content

The polarization dependent light transmission studies are conducted on water based cobalt ferrite fluids at different magnetic particle concentrations. At all concentrations studied, they exhibited dichroic characteristics. The anisotropic constant (difference in absorbance variation with field) is plotted for different concentrations in figure 6.7. It is clearly evident that the dichroism increases with concentration which is expected.

### 6.3 Nonlinear optics

Laser has become an essential part of everyday life in research, industry, medicine, communication, entertainment, military and markets. The accidental exposure to high intensity lasers may damage the human eyes and highly sensitive equipments. They need to be protected from being exposed at high intensity light. Optical limiters that allow light up to certain threshold intensity and block above the damage level are good candidates for laser protection. For an intensity dependant transmission, optical properties like refractive index and absorption coefficient need to change with light intensity. The nonlinear optics branched into another area of material research when second harmonic generation [15] is experimented successfully. The nonlinearity lay hidden in materials; requires high intensities to exhibit the effect. This requires the knowledge of light matter interaction at optical frequencies.

Light can be considered as an electromagnetic wave that span a definite frequency range. When an alternating weak electric field fall on an atom, it undergo harmonic oscillations with the applied field, with a polarization induced which is linear with strength of electric field  $E$ , as  $P = \chi E$ , where  $\chi$  is the susceptibility, a second rank tensor related to the refractive index( $n_0$ ) and absorption coefficient( $\alpha_0$ ) of the material of the medium. The dielectric constant  $\epsilon$  is related to these properties as  $\epsilon = n^2 = (1 + \chi)$ . When the intensity of the incident radiation increases, the dipole oscillations are no longer simple harmonic in nature and the polarization deviates from linearity. Magnitude of the nonlinearity will depend on the applied light field intensity and the nonlinear susceptibility coefficient,  $\chi$ .

$$P = \chi^1 E + \chi^2 E E + \chi^3 E E E + \dots \quad (6.6)$$

where  $\chi^1$  is the linear susceptibility (second rank tensor (matrix)), but  $\chi^2$  and  $\chi^3$  are second order (third rank tensor) and third order (fourth rank tensor) nonlinear susceptibilities respectively. However higher order nonlinearities die out at low intensities as the nonlinear susceptibilities are weaker compared to the linear susceptibility. The third order nonlinearity in polarization leads to nonlinear optical characteristics in refractive index and absorption leading to phenomena like self-focusing and optical limiting. Symmetry considerations show that system possesses inversion symmetry (isotropic media like solutions) lacks nonlinearities of even order; while those lacking inversion symmetry such as anisotropic crystals can exhibit both even and odd nonlinearities. Depending on the inherent order of nonlinearity of the material and the experimental conditions various nonlinear processes can be demonstrated.

#### **6.4 Third order nonlinearity**

The third order nonlinear susceptibility is related to the nonlinear refraction and absorption by

$$\text{Re } \chi^3 = 10^{-6} c n_0^2 n_2 / 480\pi^2 \quad (6.7a)$$

$$\text{Im } \chi^3 = 10^{-7} c^2 n_0^2 \beta / 96\pi^2 \omega \quad (6.7b)$$

Where  $c$  is the velocity of light (in  $\text{cm s}^{-1}$ ),  $n_0$  is the linear refractive index,  $\omega$  is the laser radiation frequency in Hz,  $\beta$  is the nonlinear absorption coefficient (in  $\text{cm W}^{-1}$ ), and  $n_2$  is the nonlinear refractive index (in  $\text{cm}^2 \text{W}^{-1}$ ). The refractive index ( $n$ ) and absorption coefficient ( $\alpha$ ) of the medium are given by

$$n = n_0 + n_2 I \quad (6.8a)$$

$$\alpha = \alpha_0 + \beta I \quad (6.8b)$$

where  $n_0$  is the linear refractive index,  $n_2$  is the nonlinear refractive index,  $\alpha_0$  is the linear absorption coefficient,  $\beta$  is the nonlinear absorption coefficient and  $I$  is the laser intensity. The propagation equation for light travelling in the  $z$  direction through a third order nonlinear medium can be written as,

$$\frac{dI}{dz} = -(\alpha_0 + \beta I)I \quad (6.9)$$

Depending on the sign of  $n_2$  and  $\beta$ , the refractive index get modified and will give rise to self-focussing or defocusing effects and modification in the absorption coefficient will lead to induced transmission or absorption.

### **6.5. Nonlinear Mechanisms**

Study of nonlinear properties of a material is of genuine interest from a fundamental point of view. The various nonlinear responses of materials depends on different parameters, including wavelength, pulse duration, and repetition rate of the incident laser beam used for the measurement [16] Different mechanisms such as nonlinear scattering, multi-photon absorption, and reverse saturable absorption including free carrier and excited state absorption are thought to be responsible for optical limiting and are associated with the effects of the material and laser parameters. Generally, more than one nonlinear mechanism coexists with relative dominancy in a material. Some major mechanisms responsible for the optical limiting property in nanomaterials are discussed in the following section.

### **6.5.1. Nonlinear scattering**

Nonlinear scattering (NLS) is an intensity dependent scattering, refers to dispersing of a highly intense beam into a larger area causing a reduction in the intensity of the emerging beam. Mie scattering theory does not allow nanoparticles to scatter a light beam effectively. The effective scattering arises from the formation of scattering centers, initiated at the nanoparticles.

The incident photon energy absorbed by the nanoparticles could subsequently be transferred as thermal energy to the surrounding solvent. This causes the evaporation of solvent and formation of bubbles. Due to the refractive index discontinuity at the vapour-solvent interface, the vapour bubbles can scatter energy effectively. This is prominent in nanosecond laser excitation, because evaporation time is also of the order of nanosecond.

The origin of the scattering centers can be from the evaporation of nanoparticles itself. In the case of metal nanoparticles, if the wavelength of the incident beam is in the surface plasmon absorption band of metal particles, strong photon absorption will take place. This process can form microplasma states in the solution, and hence serve as scattering centers. In some nanomaterials systems the two mechanisms may coexist, giving a strong optical limiting.

Another type of scattering centre formation can take place due to the variation of the refractive index of the surrounding solvents or the interface between the particles and the surrounding liquid. Such a dielectric with a refractive index discontinuity or mismatch, in the nanosecond regime can act as scattering centres.

### 6.5.2. Reverse saturable absorption

Reverse saturable absorption (RSA) is a prominent nonlinear absorption mechanism that leads to optical limiting. The processes leading to RSA can be multi-photon absorption, excited state absorption or free carrier absorption. RSA occurs when the excited state absorption cross section is greater than that of the ground state, and atoms at the ground and excited state can absorb photons of same frequency resulting in an increased absorption at high fluence. For inorganic materials, the term RSA is accepted to describe the situation where the excited state absorption (ESA) becomes greater than the ground state absorption, leading to a decrease in the transmission with increase in incident intensity.

### 6.5.3. Multi-photon absorption

A multi-photon absorption is a process in which simultaneous absorption of two or more photons occur via virtual intermediate state. The two-photon absorption (TPA) can be described by a propagation equation 6.11. Provided that the linear absorption is very small at lower intensity, the solution for transmission intensity is given by  $I(L) = \frac{I_0}{(1 + I_0 \beta L)}$ . This solution indicates that the transmission intensity decreases as the incident intensity increases, resulting into an optical limiting phenomenon. The ability of TPA induced optical limiting strongly depends upon the TPA coefficient, incident intensity and propagation length. The optical limiting characteristics of TPA materials are more effective for shorter pulses (femtosecond). The three-photon process also exhibits very similar characteristics. Linear absorption and TPA cross section are to be determined to find out the contribution of multiphoton absorption from the z-scan measurements.

#### **6.5.4. Free-carrier absorption/ Excited state absorption**

Free carrier absorption (FCA) is analogous to ESA. In semiconductors free charge carriers (electrons/holes) are generated by photon absorption process. The excited electron/hole in the conduction/valence band can absorb another photon and move higher/lower in conduction/ valence band, when the intensity of the incident radiation is high. This absorption by free carriers is known as free carrier absorption. The pulse duration should be faster than the carrier diffusion and recombination time. Since the two photon absorption can generate free charge carriers, ESA and TPA may coexist in some materials.

#### **6.6. Measuring nonlinear properties**

Measurement of optical nonlinearities requires high precision characterization techniques. The measurements are normally carried out with reference to a standard material which simplifies the whole procedure. Ammonium dihydrogen phosphate (ADP) and potassium dihydrogen phosphate (KDP) are employed as reference materials in second order nonlinearity measurements. Nonlinear interferometry, ellipse rotation, degenerate four wave mixing, nearly degenerate three wave mixing and beam distortion measurements are some techniques which require complex experimental arrangement. DFWM is used to measure third order nonlinearity and employs carbon disulphide ( $\text{CS}_2$ ) as the reference material. Z scan method [17] is a simple and direct method to measure nonlinear refraction and absorption using a single beam.

In the Z-scan experiment, a single Gaussian beam of laser is tightly focused by a convex lens and the transmittance of the sample is measured in the far field as a function of sample position with respect to the focal plane. The focal point is taken as the origin, ie  $z=0$ . The input intensity will be the maximum at this point and will

decrease symmetrically towards either side. A graph plotted with the  $z$  value on the  $x$ -axis and normalized transmitted energy on the  $y$ -axis is known as the  $z$  scan curve. The sample is kept in a translational stage along ( $z$  axis) the beam propagation direction and moved through the focal plane. At each position, the beam waist is different and hence the sample experience different intensity. The transmittance is measured as function of the position of sample. Information of the nonlinear absorption and refraction can be obtained from the  $z$  scan measurements. Depending on the experimental arrangement, there are two types: open aperture  $z$  scan and closed aperture  $z$  scan. In open aperture measurements, the transmittance is directly measured from the sample to the detector. This gives information about nonlinear absorption. While in closed aperture scan, a narrow aperture is placed in between sample and the detector. This scan results give details of nonlinear refraction. The nonlinear materials exhibit varied transmittance as a function of intensity which is exhibited as a function of  $z$  position in  $z$  scan method.

### **6.7 Ferrofluids as nonlinear optical materials**

The optical properties are related to the inherent properties as well as the size, shape, aggregation of particles and the suspended medium (matrix in composites), and the wavelength of the incident radiation. The near molecular properties exhibited by nanoparticles make them optically nonlinear. The finite size effects such as surface plasmon resonances in metals, excitonic confinements in semiconductors and concomitant blue shift of band edge could strongly result in modification of nonlinear optical properties of the material. This is how nanotechnology presents huge potential for nonlinear optics. Optical nonlinearities are reported in a number of materials such as organo-metallics, dyes, single crystals, polymers and hybrid structures. Good optical limiting devices for photonic application require better nonlinear materials with fast response, good stability in the required intensity range and wavelength.

The nonlinear properties controlled via an external stimulus present tremendous applications. The theoretical evaluation of such an externally controllable nonlinear optical material showed that nonlinear character could be tuned by an external magnetic field [18]. Ferrofluids of iron oxide nanoparticles are known for their optical limiting property and are studied by several researchers [19-20]. Besides being magnetic in nature, these nanoparticles form complex microstructures under an applied external magnetic field and this could as well tune their optical properties. The linear optical absorption and refraction properties are observed to vary with magnetic field (discussed in the beginning of this chapter) and are explained as a result of magnetic moment interacting with the electric field of radiation. In fluids, the inter-particle interactions depend on the magnetic property of the constituent particles and their surface chemistry can lead to the formation of mesoscopic chain like structures. A material whose nonlinear response could be tailored by application of an external magnetic field is of great interest to the technological world. Such a system requires an interaction between the magnetic susceptibility and nonlinear absorption of the material. Heterostructures or composites with a magnetic particle and nonlinear optical materials [21-22] have been investigated with a view towards realizing magneto controlled nonlinear optical materials for photonic devices. It is all the more convenient and simpler if a magnetic material itself is nonlinear in nature. Ferrofluids with suspended nanoparticles having appropriate dimension are good candidates for such applications. Ferrofluids based on iron oxide and its derivatives [18] and one dimensional metallic systems of cobalt [19, 23] are reported to exhibit optical limiting behavior.

### 6.8 Experimental

In the z-scan technique, the laser beam is focused using a lens, and the sample is moved along the beam axis (z-axis) through the focal point plane (which is taken as  $z = 0$ ). In this scheme each z position corresponds to an input fluence of  $4\sqrt{\ln 2}E_{in} / \pi^{3/2}\omega_{(z)}^2$ , where  $E_{in}$  is the input laser pulse energy,  $\omega_{(z)}$  is the beam radius given by  $\omega_0\sqrt{1+(z/z_0)^2}$  where  $\omega_0$  is the beam radius at the focus, and  $z_0 = \pi\omega_0^2/\lambda$  is the Rayleigh range (diffraction length). The second harmonic output (532nm) from a Q-switched Nd:YAG laser (Minilite, Continuum Inc.) is used for the measurements. Figure 6.8 is schematic of the z scan set up.

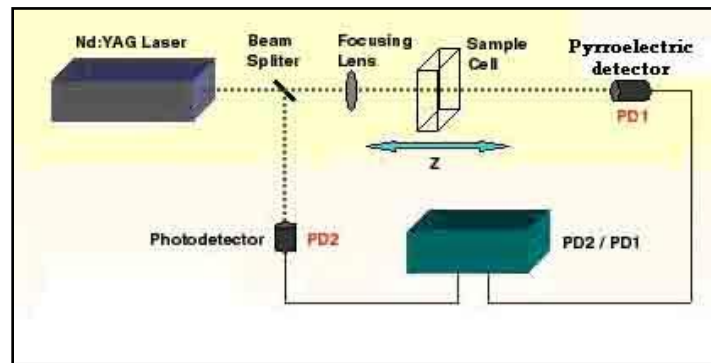


Figure 6.8: Schematic of open aperture z-scan technique.

The laser is focused using a plano-convex lens of 20 cm focal length, and the focal spot radius ( $\omega_0$ ) is 18 microns. The peak optical intensity seen by the sample at the beam focus is of the order of  $10^{12} \text{ Wm}^{-2}$ . Fluids for measurements are then taken in a 1 mm glass cuvette which is mounted on a stepper motor controlled linear

translation stage. All samples are prepared at low concentrations such that their linear transmission ranged from 50-70% at 532 nm, when taken in the 1 mm wide sample cell. The sample thickness is lesser than the Rayleigh range (1.9 mm). The sample is translated in the z direction in small steps, and the transmitted energy is measured for each position z using a pyroelectric laser energy detector (Rjp735Laser Probe Inc NY.). Two pyroelectric energy probes are used for measuring the laser energy; one energy probe monitored the input laser energy, while as the other monitored the transmitted laser energy through the sample. The experiment is automated such that laser pulses could be generated on demand. The interval between two successive laser pulses is always kept sufficiently large (typically more than 1 s), so that complete thermal relaxation of the sample occurs prior to the arrival of the subsequent pulses.

#### **6.8.1. Z scan measurements on Nickel nanofluid (Ni F)**

Z scan measurements on Ni F are carried out by adjusting the linear transmission of the fluid at the excitation wavelength to 60%. The measurements are carried out at two laser pulse energies, namely 50  $\mu\text{J}$  and 200  $\mu\text{J}$ . Figure 6.9 depicts the open aperture z scan curves of Ni F. The z scan curves indicate the presence of two competing mechanisms in Ni F sample at two different laser fluences. The results show saturable absorption behavior at moderate laser energies and an optical limiting behaviour at higher energies. The curves are redrawn with laser fluence on the x axis. The saturation trend is clearly visible in the z-scan curve corresponding to 50  $\mu\text{J}$  and optical limiting is clearly evident in the z-scan curve corresponding to 200  $\mu\text{J}$  (figure 6.9). This implies that there are two predominant causes for the nonlinearity: one is a saturation of the ground state absorption, and the other is an absorption by the excited state.

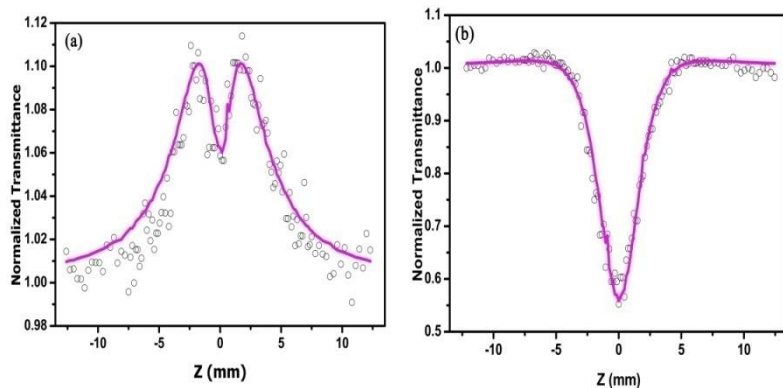


**Figure 6.9: Z scan curves on Ni F (a): at 50μJ (b): 200 μJ**

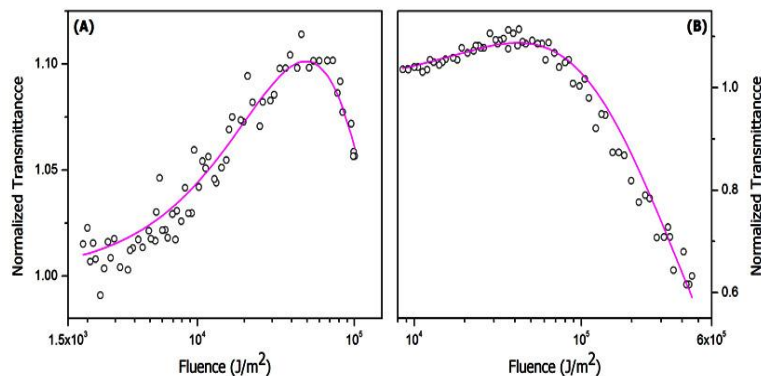


**Figure 6.10: Fluence curves derived from the z-scan measurements for input laser energies of (A) 50μJ and (B) 200 μJ. Circles are data points and solid curves are numerical fits to the data using equations 6.10.**

In order to reach a meaningful conclusion with the nonlinear optical properties, linear absorption studies are performed. A UV Vis NIR spectrophotometer ((Jasco-470) is used to measure the optical absorption in the visible and ultraviolet wavelengths. The linear optical absorption measurements (figure 6.11) on the fluid show metallic nature with absorption increasing with photon energy.

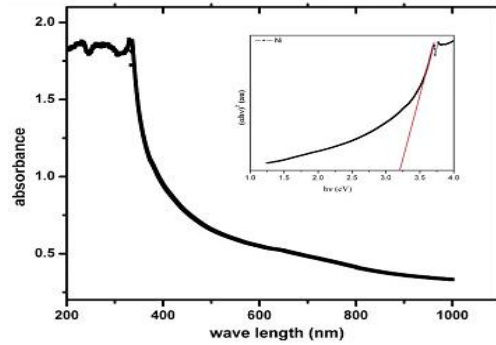


**Figure 6.11: Optical absorption spectrum of the Ni fluid. Inset shows the tauc plot for band gap calculation.**

The linear absorption data can be correlated with the nonlinear properties. At the excitation wavelength of 532 nm the sample has certain absorption (as it is evident from figure 6.11), whereas at the corresponding two photon wavelength of 266 nm, the sample shows relatively greater absorption. This indicates the existence of excited states suitable for two-step as well as genuine two-photon absorption processes. Therefore, an effective nonlinear absorption coefficient  $\alpha(I)$ , given by

$$\alpha(I) = \frac{\alpha_0}{1 + \left(\frac{I}{I_s}\right)} + \beta I \quad (6.10a)$$

can be considered for modeling the z-scan results. Here  $\alpha_0$  is the unsaturated linear absorption coefficient at the excitation wavelength,  $I$  is the input laser intensity, and  $I_s$  is the saturation intensity.  $\beta I = \sigma N(I)$  is the excited state absorption (ESA) coefficient,

where  $\sigma$  is the ESA cross section and  $N(I)$  is the intensity-dependent excited state population density. The effect of genuine two-photon absorption can be neglected because it will be much weaker compared to that of ESA. For calculating the transmitted intensity for a given input intensity, the propagation equation,

$$\frac{dI}{dz'} = - \left[ \left( \alpha_0 / \left( 1 + \frac{I}{I_s} \right) \right) + \beta I \right] I \quad (6.10 \text{ b})$$

is numerically solved. Here  $z'$  indicates the propagation distance within the sample. By determining the best-fit curves (figure 6.10) for the experimental data, the nonlinear parameters are calculated.  $I_s$  is found to be in the order of  $10^{13}$  W/m<sup>2</sup> and  $\beta$  is in the order of  $10^{-11}$  m/W. For comparison, this  $\beta$  value is in the same range as those of copper nanocomposite glasses [24], Bismuth nanorods [25] and conjugate polymer molecules [26], measured under similar experimental conditions.

### 6.8.2 Z scan measurements on oxide fluids

Laser pulse energy of 40 microjoules is used for the experiments on cobalt substituted iron oxide fluids. The fluence graphs obtained from the z-scan measurements are given in figure 6.12 a-d. These curves fit well to a three-photon absorption process, for which the transmission is given by the equation [27]

$$T = \frac{(1-R)^2 \exp(-\alpha L)}{\sqrt{\pi} p_0} \int_{-\infty}^{+\infty} \ln \left[ \sqrt{1 + p_0^2 \exp(-2t^2)} + p_0 \exp(-t^2) \right] dt \quad (6.11)$$

where  $p_0 = [2\gamma(1-R)^2 I_0^2 L_{\text{eff}}]^{1/2}$ . Here  $R$  is the Fresnel reflection coefficient at the sample-air interface,  $\alpha$  is the absorption coefficient,  $L$  is the sample length, and  $I_0$  is the incident intensity.  $L_{\text{eff}}$  is given by  $[1 - \exp(-2\alpha L)]/2\alpha$ .

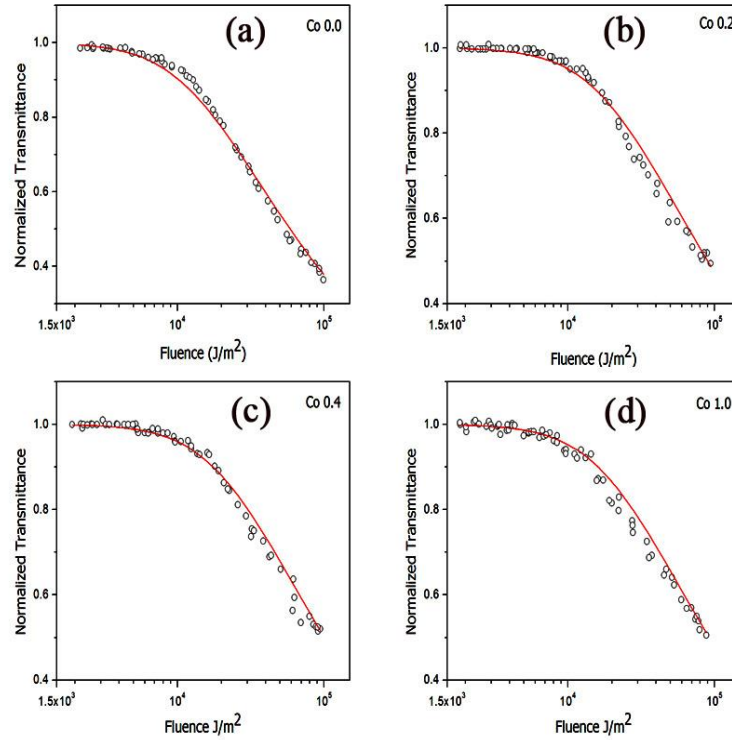


**Figure 6.12: Fluence curves derived from the z-scan measurements for input laser energies. Circles are data points and solid curves are numerical fits to the data using equation 6.11. (a): iron oxide  $\text{Fe}_3\text{O}_4$ , (b):  $\text{Co}_{0.2}\text{Fe}_{2.8}\text{O}_4$  (c):  $\text{Co}_{0.4}\text{Fe}_{2.6}\text{O}_4$  and (d):  $\text{CoFe}_2\text{O}_4$  nanoparticles suspended in kerosene**

The three-photon absorption coefficients  $\gamma$  obtained are in the order of  $10^{-22} \text{ m}^3/\text{W}^2$ . This nonlinearity possibly arises from sequential absorption of photons followed by excited state absorption or free carrier absorption. This kind of a nonlinear absorption is often termed as an “effective” three-photon absorption process. For instance, such an effective  $\chi^{(5)}$  nonlinearity of the  $\chi^{(3)}:\chi^{(1)}$  type has been observed in semiconductors [28] and metal nanoparticles [29-30] where the excited state absorption is brought about by free charge carriers.

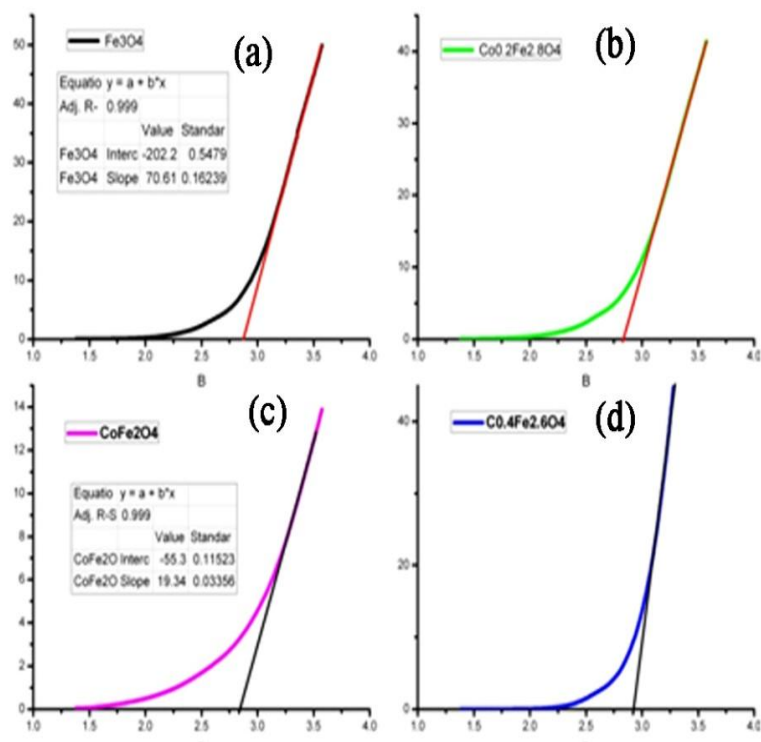


**Figure 6.13: Optical absorption measurements on oxide fluids showing the tauc plots for band gap calculation (a):Fe<sub>3</sub>O<sub>4</sub>, (b): Co<sub>0.2</sub>Fe<sub>2.8</sub>O<sub>4</sub> (c): CoFe<sub>2</sub>O<sub>4</sub> and (d): Co<sub>0.4</sub>Fe<sub>2.6</sub>O<sub>4</sub> nanoparticles suspended in kerosene**

Room temperature linear Optical absorption measurements are carried out on thin fluid films in a UV-Vis –NIR spectrophotometer (Jasco 470). Assuming direct allowed transition, the energy gap ( $E_g$ ) for all the four fluids are calculated from the relation,  $\alpha = A (h\nu - E_g)^{1/2}/h\nu$ . The linear portion of  $(\alpha h\nu)^2$  Vs  $h\nu$  (figure 6.13) on extrapolation to photon energy axis meets the photon energy corresponding to  $E_g$ .

The results from the optical measurements, both nonlinear z scan and wavelength dependant absorption, are consolidated in table 6.1( $\alpha$  is the Linear absorption coefficient,  $\gamma$  the Three photon absorption coefficient at the excitation wavelength).

**Table 6.1: absorption coefficients and band gap obtained from transmission measurements**

Sample	$\alpha$ ( $\text{m}^{-1}$ )	Band gap energy	$\gamma$ ( $\times 10^{-22} \text{ m}^3/\text{W}^2$ )
$\text{Fe}_3\text{O}_4$	693.15	2.87	6.5
$\text{Co}_{0.2}\text{Fe}_{2.8}\text{O}_4$	693.15	2.82	4.0
$\text{Co}_{0.4}\text{Fe}_{2.6}\text{O}_4$	713.35	2.84	3.2
$\text{CoFeO}_4$	713.35	2.84	2.9

It is seen that with increase in the concentration of cobalt, the degree of nonlinearity reduces. This is probably due to the presence of cobalt ions which modifies the semiconducting nature. However the band gap is not found to be modulated much with the substitution of cobalt. The linear absorption changes slightly.

Figure 6.14(a-c) depicts the z scan measurements and wavelength dependent absorption measurements (figure 6.14d) on kerosene fluid of cobalt ferrite synthesized by supersaturating with sodium hydroxide. The particles are size selected by dispersing in acetone prior to suspending in kerosene. This helps to remove larger particles from the suspension. Z scan curves are measured for 52% linear transmission at 100  $\mu\text{J}$  and 200  $\mu\text{J}$ , and at a higher transmission of 70% at 100  $\mu\text{J}$ . All the curves well fit with three photon absorption process.

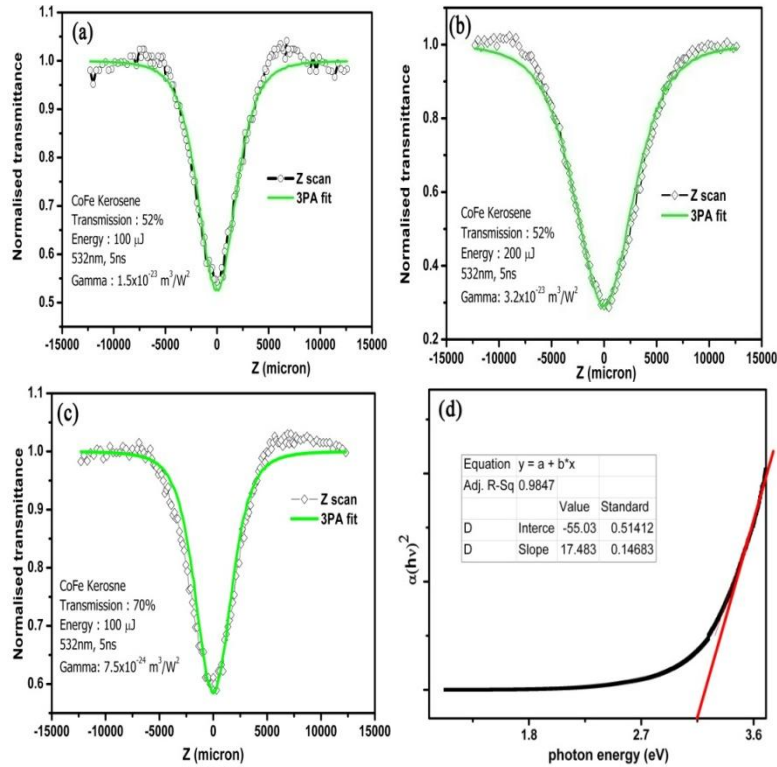


**Figure 6.14: Z scan measurements on cobalt ferrite fluid at (a) 100µJ (b) 200µJ (c) 100 µJ (d): wavelength dependant linear absorption**

The limiting is found to enhance with fluence which suggest that the material is promising for limiting devices. Almost 70% absorption is exhibited. The band gap is calculated using the tauc plot analysis. The oxide particle suspensions represent a non-linear limiting owing to three photon absorption. These oxide nanoparticles suspended nanofluids are behaving similar to semiconductors with a band gap of 2-3 eV. Nickel fluid presents a saturating nature in low fluence and limiting due to excited state absorption at moderate fluence. The fluids show good stability even after

prolonged exposure to laser. The fluids being suspensions of ultra fine particles can absorb light and relax by phonon assisted processes.

The contribution from phonons can be estimated by conducting measurements with femto second pulses so that the exact origin of nonlinearity can be extracted. The nano fluids are reported to exhibit ballistic phonon transfer that enhance thermal conductivity of the fluid in nanosecond time scales, where the nanoparticles form a local clustering with separation between particles and thus enhancing the effective volume. The energy absorbed by the nanoparticles from the incident laser pulse can be dissipated by this kind of ballistic phonons.

### **6.9 Microwave absorption properties on Iron Oxide-PVA composite films**

Ferrites are found to be good microwave absorbers and find applications in electromagnetic interference (EMI) shields. These are superior due to the minimum eddy current generation compared to ferromagnetic metals. The various interactive processes such as magnetisation and polarization in the material cause many losses in them and this makes them ideal for electromagnetic absorbers. The electromagnetic loss in soft ferrites arises from polarization effects, grain boundary effects and from the high permeability at radio frequencies.

The S (2-4 GHz) band of the microwave region of electromagnetic spectrum is especially significant in weather ranging, communication satellites, direct broadcast satellites, mobile satellite services, Wi-MAX technology and for communicating with space shuttles.

#### **6.9.1 Synthesis of composite films**

Aqueous fluid of iron oxide is prepared by the method explained in section 5.2. These fluids are carefully blended with 5% polyvinyl alcohol solution in water, by ultrasound agitation for 30 minutes. The well dispersed fluid is made to form free

standing thick films by dip coating and drying the moisture content at 60<sup>0</sup>C. The films are found to be flexible and less than 1mm thick. Films with uniform dispersion of nanoparticles could be fabricated by this method from fluids.

### 6.9.2 Experiment

The microwave characterizations are carried out in the S band by a vector network analyzer (figure 6.15a) (Rohde & Schwaz ZVB4), employing cavity perturbation technique. Cavity (figure 6.15b) is a part of rectangular waveguide of non magnetic metal with appropriate dimensions such that electromagnetic resonances are created in the chosen frequency band. The dimensions are chosen to sustain the required TE modes in the cavity. The cavity perturbation technique is based on the change in the resonant frequency and quality factor of the cavity due to the insertion of a sample in to it at the position of maximum electric field or magnetic field, depending upon the nature of the parameter to be studied. The films of composites are cut into thin rectangular sections with 2 mm X 3 cm, and inserted in to a rectangular cavity (waveguide-WR284) through a narrow line slot having dimension 3 mm x180 mm. Inserting sample into the cavity perturbs the resonance and modifies the resonance frequency and quality factor. The shift is measured at different modes and the permittivity is calculated.

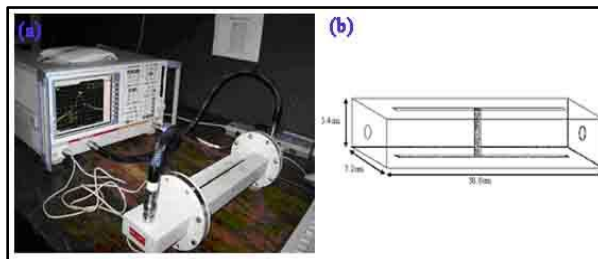


**Figure 6.15: (a) Rohde & Schwaz ZVB4 network analyser, (b) schematic of WR284 waveguide.**

The dielectric permittivity and dielectric loss of the material are evaluated by the

$$\text{formulae [31] } \varepsilon_1 = \frac{V_c(f_c - f_s)}{2V_s f_s} + 1 \quad (6.12a)$$

$$\varepsilon_2 = \frac{V_c}{4V_s} \left( \frac{1}{Q_s} - \frac{1}{Q_c} \right) \quad (6.12b)$$

where  $V_s$  and  $V_c$  are the volume of the material and cavity respectively,  $f_s$  and  $f_c$  are the resonance frequencies with and without the sample while  $Q_s$  and  $Q_c$  are the corresponding quality factors of the sample and cavity, given by

$$Q_s = \frac{f_s}{f_c - f_s}, \text{ and } Q_c = \frac{f_c}{f_c - f_s} \quad (6.13)$$

The complex permeability of magnetic materials can be evaluated by introducing the sample at the position of minimum electric field (maximum magnetic field density) in the rectangular cavity (TE<sub>10n</sub> mode), the real ( $\mu_1$ ) and the imaginary ( $\mu_2$ ) parts of the permeability are given by [32]

$$\mu_1 = 1 + K \frac{(f_c - f_s)}{f_s} \frac{V_c}{V_s} \quad (6.14a)$$

$$\mu_2 = \frac{K}{2} \left( \frac{1}{Q_s} - \frac{1}{Q_c} \right) \frac{V_c}{V_s} \quad (6.14b)$$

Where  $K$ , the geometrical factor dependent on the guided wave length ( $\lambda_g$ ) and width of the cavity (a) by the relation,

$$K = \frac{(\lambda_g^2 + 4a^2)}{8a^2} \quad (6.15)$$

For the TE<sub>10n</sub> mode,  $\lambda_g = 2L/n$ , where L is the length of the cavity and n=1,2,3,4.

### 6.9.3 Result and discussion

The dielectric permittivity and magnetic permeability of the PVA films and iron oxide–PVA composite are depicted in figure 6.16. The permittivity is enhanced for the composites due to the magnetic nanoparticles in it. These composites could be good flexible EMI shields.

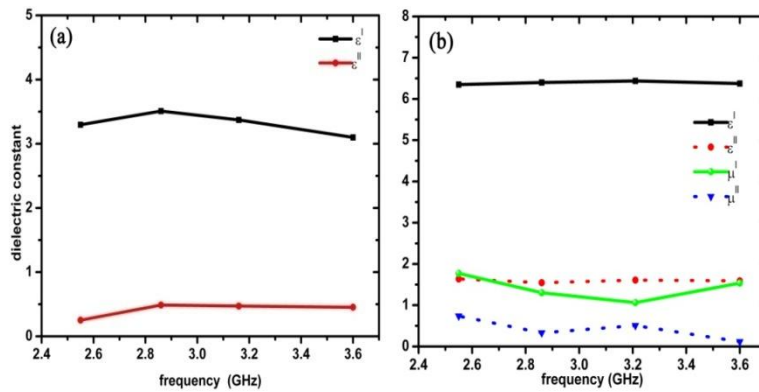


**Figure 6.16(a): permittivity of PVA films and (b): permittivity and magnetic permeability of PVA ferrite composite.**

The reflection loss has been evaluated from the values of obtained parameters for different thickness of the films and is presented in figure 6.16. The absorption or reflection at the interface depends on the permeability and permittivity of the material. The absorption of microwave at the material reduces the amount of reflected

power (reflection loss) and this is functional in stealth technology. The reflection loss is related to the normalized input impedance by the relation [33]

$$Z_{in} = \frac{Z_i}{Z_0} = \left(\frac{\mu^*}{\epsilon^*}\right)^{1/2} \tanh\left(j \frac{2\pi}{c} (\mu^* \epsilon^*)^{1/2} f d\right) \quad (6.16)$$

where f is the frequency in free space and d the thickness of the absorbing medium. The reflection loss in decibels (dB) is given by

$$\Gamma = -20 \log \left( \frac{|Z_{in}| - 1}{|Z_{in}| + 1} \right) \quad (6.17)$$

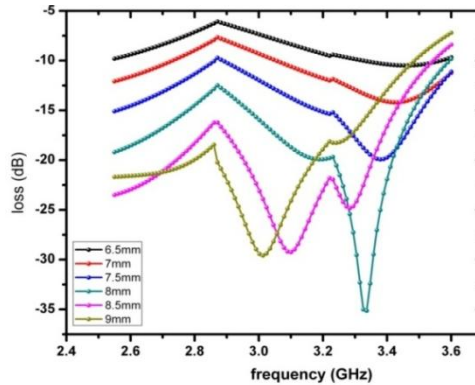


Figure 6.16: Reflection loss of composite at different thickness

Figure 6.16 depicts the reflection loss simulated from the relative permittivity and relative permeability measured by cavity perturbation method. It is obtained that the composite films are absorbing and the loss go beyond the commercially required -20dB limit for a thickness of 7.5 mm of the sample. The composites can be mould into any desired shape and size since developed by a solution drying process.

### **6.10 Conclusion**

Ferrofluids or magnetic nanofluids are good candidates for photonic devices owing to the diversity in the optical phenomena exhibited by them. The magnetic fluids of metal nanoparticles and oxide nanoparticles in different carrier liquids are studied for their optical properties. The optical transmission of the fluids could be externally controlled by an applied magnetic field as could be seen from dichroism measurements. The nature of surfactant and the surface chemistry of suspended particles decide the inter-particle interaction and the interaction of individual moments with external field. The relative strength of the two decides the cluster formation or dynamics of field induced chain formation. The magneto optical measurements shed light on the nature of interaction among the particles.

The fluids are found to exhibit good nonlinear optical properties. The fluence dependent transmission studies are conducted by an open aperture z scan method. The experimental curves are theoretically fit to explain the mechanism happening for the exhibited properties. The metallic fluids exhibited two competing characteristics: at low fluence they are found to be saturating with intensity whereas at moderate fluence, exhibited limiting nature. All the oxide fluids, iron oxide, cobalt substituted iron oxide and cobalt ferrites prepared by two different methods exhibit optical limiting showing a three photon absorption mechanism. The nanosecond excitation regime, this can originate from a two photon process followed by free carrier absorption. The phonon assisted energy transfer cannot be ruled out. Studies can be elaborated for shorter time window to eliminate thermal assisted energy transfer and find the contribution solely of electronic origin. The fluids could be magnetically controlled microscopically could also be searched for field controlled optical limiters.

Good thermal stability long shelf life and stability against aggregation make these fluids for photonic applications.

Suspensions in flexible polymers such as PVA could be mould into flexible microwave absorbers. The PVA composites with co-precipitated iron oxide nanoparticles are studied for microwave absorbing capability. These are found possess commercial significance at and above a thickness of 7.5 mm.

**References**

1. Michael Faraday, Faraday's Dairy of experimental Investigation 1820-1862, Edited by *Thomas Martin*, (2008)
2. J. L. Erskine and E. A. Stern, *Phys. Rev. Lett.* **30**, 1329–1332 (1973)
3. P.S.Pershan, *J.Appl.Phys.* **38** 1482-90 (1967)
4. Junaid M. Laskar, John Philip, and Baldev Raj, *Phys. Rev. E* **78**, 031404 (2008)
5. Q Zhang, J.Wang, and H Zhu, *J. Appl. Phys.* **78** 3999-4002(1995)
6. N. A. Yusuf, A. Ramadan and H. Abu-Safia, *J. Magn. Magn. Mater.* **184** 375-386(1998)
7. D. Jamon, F. Donatini, A Sibli, F.Royer, R.Perzinski, V.Cabuil and S. Neveu, *J. Magn. Magn. Mater.* **321** 1148-54 (2009)
8. H-E Horng, S. Y. Yang, S.L.Lee, C-Y Hong and H-C Yang, *Appl.Phys. Lett* **79** 350-52 (2001)
9. C. Groß, E. Romanus, G. Glöckl, P. Weber, and W. Weitschies, **3**. 22-23 (2002 )
10. T.Du, S.Yuan and W. Luo, *Appl.Phys.Lett.* **65** 1844-46 (1994)
11. Helen W Davies and J Patrick Llewellyn 1980, *J. Phys. D: Appl. Phys* **13** 2327.
12. B. R. Jennings, M. Xu, and P. J. Ridler Source 2000, *Proceedings: Mathematical, Physical and Engineering Sciences* **456**, 891-907
13. V. Socoliuc, M. Ras, V. Sofonea, D. Bica, L. Osvath and D. Luca 1999, *J. Magn. Magn. Mater.* **191** 241-248
14. V. Socoliuc, M. Ras, V. Sofonea, D. Bica, L. Osvath, D. Luca, *J. Magn. Magn. Mater.* **191** 241-248 (1999)

15. Richard L Sutherland , *Handbook of nonlinear optics, second edition*
16. Wang, J. Blau, W. J. *J. Opt. A: Pure Appl. Opt.* (2009) 11 024001.
17. M.Sheik-Bahae, A.A.said, T-H wei, D.H.hagan, E.W. Van Stryland, *IEEE J. Quant. Ele.* **26** 760-69 (1990)
18. J.P. Huang and K. W. Yu. 2005 , *Appl. Phys. Lett.* **86** 041905
19. S. S. Nair, J. Thomas, C.S. Suchand Sandeep, M. R. Anantharaman and R. Phillip. 2008 , *Appl. Phys. Lett.* **92** 171908(1-3).
20. J. Chen, X. Chen, S. Pu, Z. Di and Y. Xia 2007 , *Opt. Comm.* **276** 268.
21. G. Xing, J. Jiang, J. Y. Ying, and W. Ji, 2010 , *OPTICS EXPRESS* 18 (6) 6183-90.
22. E. Cattaruzza, F. Gonella, G. Mattei, P. Mazzoldi, D. Gatteschi, C. Sangregorio, M. Falconieri, G. Salvetti, and G. Battaglin 1998 , *Appl. Phys.lett.* **73** 1176.
23. T.N Narayanan, C S Suchand Sandeep, M M Shaijumon, P M Ajayan, Reji Philip and M R Anantharaman 2009 , *Nanotechnology* **20** 285702(1-7).
24. B. Karthikeyan, M. Anija, C.S. Suchand Sandeep, T.M. Muhammad Nadeer, R. Philip 2008, *Opt. Commun.* **281** 2933-2937.
25. S. Sivaramakrishnan, V.S. Muthukumar, S. Sivasankara Sai, K. Venkataramaniah, J. Reppert, A.M. Rao, M. Anija, R. Philip, N. Kuthirummal 2007, *Appl. Phys. Lett.* **91** 093104.
26. P.K.Hegde, A.V.Adhikari, M.G. Manjunatha, C.S. Suchand sandeep, R.Philip, *Synthetic Metals* (in press).
27. *Handbook of Nonlinear Optics*, R.L.Sutherland, Marcel Dekker, NY (1996)
28. A. A. Said, C. Wamsley, D. J. Hagan, E. W. Van Stryland, B. A. Reinhardt, P. Roderer and A. G. Dillard, *Chem. Phys. Lett.* **228**, 646 (1994).

29. P. V. Kamat, M. Flumiani and G. V. Hartland, *J.Phys.Chem.B.* **102**, 3123 (1998).
30. J. Thomas, M. Anija, J. Cyriac, T. Pradeep and R. Philip, *Chem. Phys. Lett.* **403**, 308 (2005)
31. Dube, D. C.; Lanagan, M. T.; Kim, J. H.; Jang, S. J. *J. Appl. Phys*, 63, 2466. (1988)
32. Sklyuyev, A.; Ciureanu, M.; Akyel, C.; Ciureanu, P.; Menard, D.; Yelon, A. *IEEE CCECE* 1486. (2006)
33. David P Cheng, *Field and wave Electromagnetics.*

## *Chapter 7*

### **A preliminary investigation on the transport properties of nanofluids based on iron oxide**

Ferrofluids are good heat transfer agents and hence thermal conductivity of these fluids decides their application potential. Since the major component of these fluids is ferri/ferromagnetic material, magnetic field dependent thermal properties are also of significance. The transport properties of these fluids are of preliminary in nature and the initial results are presented in this chapter.

## **7.1 Introduction**

Nanofluids are dilute suspensions of nanoparticles specifically designed for heat transfer applications by increasing the thermal conductivity. With the demand of efficient heat exchangers in electronic and automobile industry, this typical class of fluids assumes significance and has grown into a branch of heat engineering. The efficiency of heat transfer improves the productivity, performance and life time of the machines, electronic devices and equipments. Heat transfer properties are decided by the thermal conductivity as well as the heat transfer mechanism. The conventional fluids used in coolant technology are water, ethylene glycol and transformer oil all with low thermal conductivity. Nanofluids with good heat transfer property reduce the size of the cooling system and improve the efficiency. The widespread use of cell phones and portable devices necessitated smart nanofluids that can effectively handle energy and reduce the wastage of energy.

The thermal conductivity was proposed to increase by adding solid particles with high thermal conductivity and the effective thermal conductivity was proposed by Maxwell theory [1]. These micron sized particle suspension often resulted in clogging in channels of flow. Choi [2] *et. al* proposed the superior nanofluids for intensified heat transfer due to many reasons. Nanoparticles possess high surface area and hence more heat transfer surface between particles and surrounding fluid. The suspensions are highly stable with Brownian motion and clogging can be avoided. The enhancement in thermal conductivity depends on the parameters such as size and shape of the particles, the pH and viscosity of the liquid, additives present and volume fraction of the nanoparticles. The heat transfer properties need to be analyzed in both static and dynamic flow conditions at varied temperature and pressure.

From the conception of nanofluids in cooling systems, extensive studies are made with a lot of liquids such as water, ethylene glycol(EG) and oils suspended with nanoparticles of oxides[3-5] (alumina, titania, copper oxide) and metals(Cu, Ag) [6-8] and carbon nanotubes[9-10] and recently graphene and decorated grapheme[11-12]. The convective heat transfer together with the effective thermal conductivity of the solid particles enhances the thermal conductivity. The variation in conductivity at different pressures and temperatures and flow rate are to be studied for end application as a coolant fluid.

The exact mechanism of the improved thermal conductivity and heat exchanging property is rather contradicting [13]. The classical effective medium theory Hamilton crosser models cannot explain effectively the varied responses reported by various researchers mentioned above. The underlying mechanism still is to be critically investigated. Magnetic nanofluids, the suspensions of superparamagnetic particles are made a model nanofluids system to study the mechanism [14-15]. The studies on the ferrofluids show that, in addition to the micro convection aided by Brownian motion, aggregation effects plays a key role in deciding the thermal conductivity (k) enhancement. The heat transport through the percolating path made by nanoparticles explains the enhancement in k value. The enhancement of 300% is exhibited with an external magnetic field in ferrofluids. This makes ferrofluids smart heat transfer fluids which could be controlled by an external means.

The magneto optical studies on the fluids show a kind of clustering and chain formation effects under an applied field. This system could be searched for magnetic field dependent heat conducting properties. This chapter contains an initial

investigation on the magnetic field dependent heat transfer properties of ferrofluids of magnetite suspended in kerosene.

## 7.2 Theoretical concepts

The models of thermal conductivity enhancement in nanofluids could not satisfactorily explain the various features presented by them. There are many semi empirical correlations that explain conductivity of mixtures.

Classical models consider only the thermal conductivities of the solid particles, their size, shape and volume fraction and thermal conductivity of the suspended media. The Maxwell-garnet model for a two component system [1] correlates the effective thermal conductivity ( $k_{eff}$ ) with that of solid ( $k_p$ ) and of liquid ( $k_f$ ) and the solid concentration ( $\phi_p$ ) as

$$k_{eff} = \frac{k_p + 2k_f + 2(k_p - k_f)\phi_p}{k_p + 2k_f - (k_p - k_f)\phi_p} k_f \quad (7.1)$$

This model could successfully explain the mixture of solid-solid and micron sized solids in liquid. This model considers the interfacial resistance and hence fails to explain when the particle concentration is above a threshold.

The nanofluids with large surface area could not fit well with the classical model owing to the large interfacial effects. Bruggeman model analyses the interaction among the particles and for spherical particles the conductivity takes the form

$$k_{eff} = (3\phi - 1)k_p - (3\phi - 2)k_f + \sqrt{\Delta} \quad (7.2)$$

where  $\Delta = (3\phi - 1)^2 k_p^2 + (3\phi - 2)^2 k_f^2 + 2[2 + 9\phi(1 - \phi)] k_p k_f$ . This model well works with even high concentrations. For non spherical particle mixtures

Hamilton Crosser (HC) model best explains which include a shape factor  $n$ . According to this model for a solid liquid mixture with relative conductivity of conductivity of 100 can be written as

$$k_{eff} = \frac{k_p + (n-1)k_f - (n-1)(k_f - k_p)\varphi}{k_p + (n-1)k_f + (k_f - k_p)\varphi} k_f \quad (7.3)$$

Where  $n = 3/\psi$  where  $\psi$  defines the sphericity of particles, the ratio of surface area of the sphere with volume equal to that of the particle to the surface area of the particle.

A comprehensive model by Keblinsky [16] explains the various factors that contribute to the thermal conductivity in nanofluids. The Brownian motion of nanoparticles, collision between the solid particles, molecular layering of the liquid around the nanoparticles [17], and clustering of nanoparticles contribute to the mechanism of heat transfer. The Brownian motion [18] and the collision have its characteristic time and this could not account for the fast response of thermal conductivity shown in many nanofluids systems. The layering of liquid molecules over the solid particles accounts for a large thermal conductivity. [19]. The clustering of nanoparticles into chain like ordered structures are another possibility as seen in ferrofluids with large increase of thermal conductivity.

The heat transport in nanofluids is best believed to be ballistic in nature rather than diffusive or convective. The thermal conductivity is modeled to increase when the clusters are loosely packed with layering of liquid molecules separating them. The nano clusters formed could form thermally less resistant path and increased effective volume from the actual physical volume. The liquid layer mediated nano clusters could transfer heat faster. The ballistic phonons initiated in one nano particle of the cluster could persist in the surrounding liquid layer of 1 -2 nm thick and could reach

upto the nearest particle. The mean free path of phonon in liquid is very small and hence this happen only for a particle - particle separation around 1- 2 nm.

The ferrofluids are suspensions of nanoparticles with an average size ~ 10 nm suspended in a base liquid and could easily be controlled by an external magnetic field. The field induced microstructure formation has resulted in various optical properties as discussed in chapter 6. This chain formation or nano clustering could enhance the heat transfer properties.

### 7.3 Thermal conductivity on Iron oxide suspended in kerosene

The thermal conductivity measurements of the base liquid and the fluid is measured in different magnetic field using a transient hot wire set up in (KD2 Pro). This measures the heat dissipation from a line source. The accuracy is within 5%. The thermal conductivity of the fluid (k) relative to the thermal conductivity of the base liquid ( $k_f$ ) as function of applied magnetic field is plotted in figure 7.1.

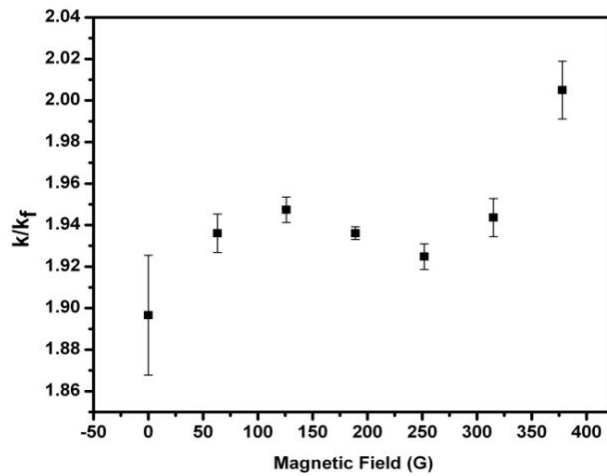


Figure 7.1: Variation of thermal conductivity as a function of applied field

The thermal conductivity of the fluid has enhanced compared to the base liquid by 90% where as the enhancement with field is less prominent from 90 to 100% at an applied field strength of 400 G. The initial result on the ferrofluid is encouraging and the measurement need to be carried out with different concentrations and fluids based on other nanoparticles. The enhancement in thermal conductivity can be attributed to the clustering caused by dipolar exchange interaction of magnetic nanoparticles which possess large magnetic moment. The effects of clustering on kerosene based iron oxide ferrofluids has been discussed based on the magneto-optical transmission measurements (chapter 6). The clustering gets enhanced with applied field and this might have caused enhancement in conductivity.

**References**

1. J. C. Maxwell, A Treatise on Electricity and Magnetism, 2nd ed. Clarendon, Oxford, 1881.
2. Lee S, Choi SUS, Li S, Eastman JA. *ASME J Heat Transfer* **121** 280–9 (1999)
3. Lee S, Choi SUS, Li S, and Eastman JA: *J. Heat Transfer*, **121** 280 (1999).
4. N. Jha and S. Ramaprabhu, *J. Appl. Phys.* **106**, 084317 (2009)
5. Kang HU, Kim SH, Oh JM: *Exp Heat Transfer* **19** 181 (2006)
6. J. A. Eastman, S. U. S. Choi, S. Li, W. Yu, L. J. Thompson, *Appl. Phys. Lett.* **78** 718-20 (2001)
7. E. Pradeep J. Sudhan and K. S. Meenakshi , *Indian J. Sci. Tech.* **4** 417-21 (2011)
8. P. Warriar and A. Teja , *Nanoscale Res. Lett.*, **6** 247 (2011)
9. SUS Choi, ZG Zhang, W Yu, F Lockwood, Grulke EA: *Appl Phys Lett*, **79** 2252 (2001)
10. Ding Y, Alias H, Wen D, and R A Williams: *Int J Heat Mass Transfer*, **49** 240 (2006)
11. Tessy Theres Baby and S. Ramaprabhu , *J. Mater. Chem.* **21** 9702 (2011)
12. Tessy Theres Baby and Sundara Ramaprabhu, *Nanoscale Res. Lett.* **6** 289 (2011)
13. D.Wen, G.Lin, S.Vafaei, and K.Zhang, *Particulology*, **7** 141-150 (2009)
14. J.Philip, P.D.Shima and B. Raj, *Appl. Phys. Lett.* **92**, 043108 (2008)
15. J.Philip, P.D.Shima and B. Raj, *Appl. Phys. Lett.* 91, 203108-10 (2007).

16. P. Keblinski, S. R. Phillpot, S. U.-S. Choi, and J. A. Eastman, *Int. J. Heat & Mass Transfer* **45** 855-863 (2002).
17. Le-Ping Zhou, Bu-Xuan Wang, Xiao-Feng Peng, Xiao-Ze Du, and Yong-Ping Yang, *Advances in Mechanical Engineering* 172085 (2010)
18. Manju Prakash · E. P. Giannelis, *J Computer-Aided Mater Des* **14**:109–117 (2007)
19. W. Yu and S.U.S. Choi, *J. Nanoparticle Res.* **5** 167–171 (2003)

## *Chapter 8*

### **Conclusion**

A thorough investigation on a focal theme is what a Ph. D thesis demands and here too an earnest attempt has been made on two aspects: a) fundamental and b) applied. The realm of ferrofluids is very vast and is a virgin area where a lot of innovations are in the offing and even though the focused area of research is in “nanosized” dimensions, a complete study is next to impossible. So there are lacunae and gaps in the present study which can be addressed further by other researchers. However, this investigation has also produced some salient results which are noteworthy and need mention. This chapter encompasses the salient results obtained out of this investigation. This chapter also inspects the drawbacks and will also talk about the future prospects.

The progress of mankind has been synonymous with the development of novel materials. The quest for making life more humane, the necessity for removing obsolescence, making new devices and understanding new phenomenon for applications has been the hallmark of material research. If material scientists played with composition and incorporated impurities for tailoring properties, now it is the turn of the scientists working in the area of nanoscience to tune the properties by hobnobbing with the dimensionalities, size and shape. Nanoscience employs size and shape for arriving at superlative properties and thus the job of the material scientists has been lessened. The days are not far off where the nation's progress is gauged by the progress in nanoscience. So nanoscience and nanotechnology is going to have a strong bearing on the economy of the country. The work which has been presented in this thesis is also to be seen as a small attempt in order to add drop wise to the mighty ocean of advances in nanotechnology.

The material science research necessitates the synthesis of materials by inexpensive, economically viable techniques that can be carried out at ordinary conditions. The history of sample preparation is needed for better understanding of the properties and to design the preparation conditions for better results. The synthesis of nano materials needs special attention, since a slight deviation can alter the properties to a great extent. The synthesis parameters for desired output are to be optimized by trial and error. The broad theme of this particular study is ferrofluids. As has already been stated, the basic ingredient of a ferrofluid is surfactant coated magnetic nanoparticles having less than 10 nm size. Ferrofluids can be categorized into two, namely the hydrocarbon based and the aqueous based. Ferrofluid based on hydrocarbons are increasingly being used in engineering applications as rheological fluids in automobiles, as earthquake arrestors, perfect sealants, in clutches and in a horde of other devices. Water based ferrofluids have become very important and

aqueous ferrofluids based on superparamagnetic iron oxide nanoparticles (SPIONs) have become the cynosure of biotechnologists because SPIONs are bio compatible, they can perform site specific drug delivery, cell separation, detect diseases and can also cure deadly diseases like cancer. So any study on ferrofluids assumes significance not only from a fundamental perspective but also from an applied point of view. From a fundamental perspective, the realm of magnetic nanoparticles is always enriching and a hot area of research pursued aggressively by physicists, chemists and engineers alike. Phenomena like the existence of surface spins, spin glass, superparamagnetism and frustrated spin systems are all very attractive and demand thorough investigations. Though much attention has been paid in recent years on the study of ferrofluid based on  $\text{Fe}_3\text{O}_4$ , not much attention is devoted to the study of fluid based on metals, especially fluids based on Ni, Co etc. This is primarily because of the difficulty in synthesizing pure; nano sized Ni particles and the dearth of dispersing them in carriers like kerosene. This thesis also has paid considerable attention in synthesizing good quality ferrofluid based on nickel. A detailed investigation on the synthesis and characterization of Ni ferrofluid is carried out. During the course of investigation of nickel nanofluids, considerable insight has been derived on the low temperature ordering of small particles in different regimes *vis-a-vis* the interacting as well as non-interacting nature.

The Ni nanoparticles being highly prone to oxidation need careful control since oxidation may alter the magnetic properties to a complex behaviour. Sol-gel auto combustion technique was optimized to obtain pure crystalline nanoparticles of fcc Ni in large amounts. This novel technique seems to be superior over the known methods. However the particles were distributed in size and deviated from exact spherical shape. The actual mechanism or kinetics involved could not be resolved out

since the reaction occurs instantaneously. Careful analysis is required to elucidate the mechanism and thus control over the size distribution and shape can be achieved.

Stable fluids require the particles to be of certain size decided by the density, type of stabilization applied and the viscosity of the carrier liquid. The Nickel nanoparticles subjected to high energy ball milling in the presence of oleic acid result in particle size reduction and the surface energy created a platform for the adsorption of oleic acid onto particle surfaces. These surfacted particles were size selected in kerosene and metallic nanofluids are realized which are of great technological interest in heat engineering, magneto-optics and photonics.

The structural and magnetic measurements and analysis reveal the purity of the Ni nanoparticles. The nanoparticles of size  $\sim 5$  nm exhibited a magnetic ordering that enormously increased the moment especially at low temperature. The ordering was pronounced for the smaller particles at low temperature need deeper and closer look at them at various magnetic fields. The fluids exhibited stability with aging and applied magnetic field. They are found to possess good magneto-optical responses. The optical nonlinearity studied at nanosecond excitations exhibited saturation at low fluences and limiting nature at high fluences. The mechanism is identified to be excited state absorption. Nevertheless the thermal contribution cannot be ruled out. The measurements at femto second pulses can shed a light into this. This is to be carried out later and is a futuristic proposition.

Ferrofluids based on ferrites are also important from a technological point of view. This is because the properties of the constituent nanoparticles can be tailored by appropriate choice of the cations residing the octahedral and tetrahedral sites. Thermally sensitive ferrofluids based on Manganese Zinc ferrite and the more important Cobalt ferrites based fluids were also subject of this study. The fluid

synthesis needs better understanding of colloidal chemistry and co-precipitation followed by *in situ* surface treatment and dispersing in liquid sounds better and simple. The proper choice of a combination of metal salts and rate of addition of reactants, the temperature and pH of super saturation etc are optimized for each system of ferrites and ferrofluids with hydrocarbon and aqueous base are synthesized. All the fluids exhibit good shelf life. The fluids of manganese zinc ferrite, with different surfactants are compared on the basis of inter-particle interactions. The magnetic properties related to the chemical environment need special attention when proposed for various field dependent applications. The fluids of cobalt substituted magnetite were found to exhibit enhanced coercivity due to the introduction of anisotropic cobalt ion in the lattice. The relaxation behaviour is complex with contribution arising from Neel and Brownian type, and the blocking is shifted to near room temperature. This can be tuned to room temperature and above by manipulation of particle size. Room temperature blocking is of particular interest in magnetic refrigeration and high density data storage. This is relevant and assumes significance because scientists are searching for eco-friendly techniques like magnetic refrigeration for production of low temperatures. Though Gadolinium alloys are a prospective material for magneto caloric applications, the search for cheaper alternatives based on ferrites is on. The size effects on the blocking temperatures of these ferrites are particularly of interest to mechanical engineers because  $T_B$  decides the operating temperature. The nanoparticles of ferrites exhibit cation redistribution and mixed valency and alter the properties from their bulk counterparts. This requires analysis by sophisticated measurement techniques such as X-ray photoelectron spectroscopy and Mossbauer studies. This could not be carried out. Aqueous ferrofluids based on SPIONs are important for biomedical applications. For biomedical applications, these particles have to be functionalized wherein a drug

molecule can be attached, dragged by an external magnetic field and delivered to the site also by the application of an external magnetic field. So SPIONs are to be coated with Silica resembling a core shell structure. This has been attempted and was successful in synthesizing, and characterizing these fluids. SPIONs based on aqueous ferrofluid are useful for cancer treatment. The application of an AC magnetic field generates heat on to the tissue or cell where the nanoparticles are attached. This requires appropriate modeling and simulation. The power loss at various frequencies has been estimated and this is one of the important outcomes of this present investigation.

The bio compatibility and non-interacting nature is improved by surface modification with silica. A silica particle contained more than a magnetic particle; single particle modification is possible with the addition of right amount of silane. The specific absorption rate has to be measured *in vivo* for real ground applications.

Ferrofluids display interesting micro/nanostructures under an external applied magnetic field. The interaction among particles also results in varied pattern formation. This result in modified optical properties with the field induced anisotropy in them. The ferrofluids are proposed to be magneto-controlled optical switches, gratings and polarizer. Dichroism measurements carried out in various ferrofluids explicate the interaction effects depending on the colloidal environment and the suspended medium together with particle loading. The measurement can be extended to dynamic regime where a time varying magnetic field can be applied to study relaxation mechanism especially suitable to find the chemical species attached to the magnetic particle.

The nanofluids of ferrites are found to be good optical limiters with a theoretical agreement with predominant three photon absorption process. The particles being covered with layer of liquid molecules, one can also think of a phonon

assisted energy distribution aiding the nonlinear process. The measurement was carried out in nanosecond window which can access thermal relaxation as well. This effect can be eliminated and the contribution of pure electronic origin can be identified with femto second pulses. The magnetic field induced micro-structural formation and the resulting optical transmission and the nonlinear measurements with fast energy transfer intuit one to think of applying the ferrofluids into heat transfer applications. An appropriately magnetic field controlled optical limiter could be a possibility.

The nanofluids are employed in heat engineering and as heat transfer fluids for coolant technology. The field dependent clustering can be exploited to improve the thermal conductivity of the ferrofluids since they can form highly conducting channels by chain formation in the direction of the applied magnetic field. The liquid layering with ballistic phonon transfer among nanoparticles could be a reasonable explanation for increased conductivity of nanofluids. The measurement conducted in kerosene based iron oxide ferrofluids using a transient hot wire set up with applied magnetic field show a 100% increase of thermal conductivity. The thermal conductivity studies can be extended to other fluids and metal based fluids which is an important future perspective of the present investigation.

With the advent of fast and wide communication technology, the s band of microwave spectrum has been exploited thoroughly. The microwave absorbing studies conducted in PVA- iron oxide composite is hopeful for flexible EMI shields. The composites are finely dispersed since the starting material is also a fluid. The composites with manganese zinc ferrites which have high permeability could be investigated in the future and may yield good results.

Ferrofluids exhibit various instabilities in an external applied field. Rosensweig instability is observed at magnetic fluid and nonmagnetic interface under

a perpendicular magnetic field. The instability depends upon the strength of magnetic field energy, the viscosity and surface tension and the gravitational field energies. The surface deformation in an applied magnetic field normal to the surface taken is presented in figure 8.1.

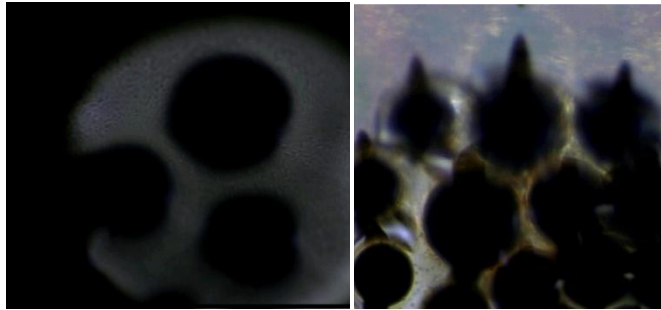


**Figure 8.1: Rosensweig instability at ferrofluid air interface (left) low applied field (right) high field**

The careful analysis of these instabilities can give a light on the symmetry breaking in physical systems and is important to study the physics of *Ferrohydrodynamics* deeply. The pattern acquires different orders of instability at critical field strengths as observed at two different applied fields and qualitative and quantitative measurements and analysis is another future prospective which can be carried out in near future. The thesis is also incomplete and much needs to be carried out. The present investigation carried out which has resulted in this thesis may be set as a precursor to further studies on this interesting entity called nanofluids

## List of publications

### Journal papers

1. T. N. Narayanan, **A. P. Reena Mary**, M. M. Shaijumon, L. Ci, P. M. Ajayan, and M. R. Anantharaman, "Carbon nanotube-iron oxide composite produced by filling multiwall carbon nanotubes with aqueous ferrofluid" *Nanotechnology* 20, 055607 (2009)
2. **A. P. Reena Mary**, T. N. Narayanan, Vijutha Sunny, D. Sakthikumar, Yasuhiko Yoshida, P. A. Joy and M. R. Anantharaman. Synthesis of Bio-Compatible SPION-based Aqueous Ferrofluids and Evaluation of Radio Frequency Power Loss for Magnetic Hyperthermia *Nanoscale Res Lett* (2010) **5**:1706–1711
3. T. N. Narayanan, **A. P. Reena Mary**, P. K. Anas Swalih, D. Sakthu Kumar, D. Makarov, M. Albrecht, Jayesh Puthumana, Abdulaziz Anas, and M. R. Anantharaman: Enhanced Bio-Compatibility of Ferrofluids of Self-Assembled Superparamagnetic Iron Oxide-Silica Core-Shell Nanoparticles *Journal of Nanoscience and Nanotechnology*, (2011) **11** 1958-1967.
4. **A.P. Reena Mary**, C. S. Suchand Sandeep, T.N. Narayanan, P. M. Ajayan, Reji Philip, and M. R. Anantharaman, Non-linear and Magneto optical transmission studies on self-assembled magnetic nanofluids of oxide free metallic nickel *Nanotechnology* (2011) 22(**37**):375702
5. R.K. Srivastava, T.N.Narayanan, **A.P.Reena Mary**, M.R Anantharaman, A.Srivastava, P.M.Ajayan and Robert Vajtai, Ni filled multiwalled Carbon nanotube polystyrene composite films as efficient microwave absorbers. *Appl. Phys. Lett.*, 99, 113116 (2011).

6. Evidence for low temperature magnetic ordering in metallic nickel nanoparticles of nanofluids synthesized via a two step synthetic route.(ready for communication)
7. Surfactant mediated interactions and clustering effects in water and hydrocarbon based ferrofluids of  $Mn_{0.6}Zn_{0.4}Fe_2O_4$  (ready for communication)
8. Field induced scattering mediated by chain formation and clustering in surfacted and ionic stabilized ferrofluids; a study based on magneto optical measurements.(manuscript ready)

#### **Conference papers**

1. Aqueous Ferrofluid of Iron Oxide Nanoparticles Synthesized In Starch-Oleic Acid Complex. *Reena Mary A P*, Arun Aravind, P A Joy and M R Anantharaman-ICNA 2007,NIT Trichy
2. Room Temperature Ferromagnetism in  $Zn_{0.95}Co_{0.05}O$  Diluted Magnetic Semiconductors *Reena Mary A P*, Manfred Albrecht, Guenter Schatz, , M R Anantharaman-NCSE2007 CMET Thrissur.
3. Cobalt Doped Zinc Oxide Systems: Structural and Optical Properties *Reena Mary A P* and M R Anantharaman- Mat Con 2007, CUSAT
4. Model Dielectric Function Analysis for Band gap Calculations on bulk ZnO particles & Spin coated ZnO films. Narayanan T N, *Reena Mary A P* and M R Anantharaman.-CTMS 2007 Christian college Chengannur
5. 6th International Symposium on Bioscience & Nanotechnology, November 2008, Toyo University, Japan On the preparation and properties of CNT-SPIRON nanocomposites. T N Narayanan, *A P Reena Mary*, M M Shaijumon, P M Ajayan, and M R Anantharaman

6. Second International Conference on Frontiers in Nanoscience and Technology, Cochin Nano-2009, Field Induced transmission studies on kerosene based ferrofluids A P Reena Mary, Vijutha Sunny and M R Anantharaman
7. A P Reena Mary, T N Narayanan, Vijutha Sunny, Sakthi Kumar, M R Anantharaman .Studies on properties of aqueous ferrofluids for magnetic hyperthermia, Kerala Science congress KFRI Peechi-2010. (**best poster** )
8. A P Reena Mary, and M R Anantharaman, international conference on magnetism and magnetic materials MMM 2008, NPL New Delhi